NOTICE

AVIS

The quality of this microform is heavily dependent upon the quality of the original thesis submitted for microfilming. Every effort has been made to ensure the highest quality of reproduction possible.

If pages are missing, contact the university which granted the degree.

Some pages may have indistinct print especially if the original pages were typed with a poor typewriter ribbon or if the university sent us an inferior photocopy.

Reproduction in full or in part of this microform is governed by the Canadian Copyright Act, R.S.C. 1970, c. C-30, and subsequent amendments.

La qualité de cette microforme dépend grandement de la qualité de la thèse soumise au microfilmage. Nous avons tout fait pour assurer une qualité supérieure de reproduction.

S'il manque des pages, veuillez communiquer avec l'université qui a conféré le grade.

La qualité d'impression de certaines pages peut laisser à désirer, surtout si les pages originales ont été dactylographiées à l'aide d'un ruban usé ou si l'université nous a fait parvenir une photocopie de qualité inférieure.

La reproduction, même partielle, de cette microforme est soumise à la Loi canadienne sur le droit d'auteur, SRC 1970, c. C-30, et ses amendements subséquents.

Canada

UNIVERSITY OF ALBERTA

CONVECTIVE STORMS AND MOISTURE FIELDS
IN LIMEX85:
A CASE STUDY

by

M.P. Brennand

A THESIS

SUBMITTED TO THE FACULTY OF GRADUATE STUDIES AND RESEARCH OF
THE UNIVERSITY OF ALBERTA IN PARTIAL FULFILLMENT OF THE
REQUIREMENTS FOR THE DEGREE

MASTER OF SCIENCE

in

METEOROLOGY

DEPARTMENT OF GEOGRAPHY

Edmonton, Alberta

Fall 1992

Canada

UNIVERSITY OF ALBERTA

RELEASE FORM

NAME OF AUTHOR: Michael P. Brennand

TITLE OF THESIS: Convective Storms and Moisture Fields in LIMEX85:
A Case Study

DEGREE: Master of Science

YEAR THIS DEGREE GRANTED: 1992

Michael P. Brennand

c/o   Concord Environmental
#1190, 555 - 4th Avenue S.W.
Calgary, Alberta
Canada   T2P 3E7

DATE 92 05 20

UNIVERSITY OF ALBERTA

FACULTY OF GRADUATE STUDIES AND RESEARCH

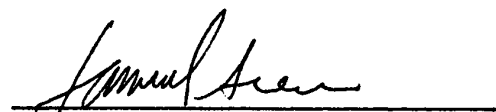The undersigned certify that they have read, and recommend to the Faculty of Graduate Studies and Research for acceptance, a thesis entitled Convective Storms and Moisture Fields in LIMEX85: A Case Study submitted by Michael Brennand in partial fulfillment of the requirements for the degree of MASTER OF SCIENCE in METEOROLOGY.

Dr. E. Lozowski

Dr. G. Reuter

Dr. S.S. Shen

DATE   May 11, 1992

ABSTRACT

The goal of this research is to delineate the evolution of various moisture measures in the vicinity of convective storms, and to look for evidence that the observed storms were influenced by the moisture fields. The moisture measures investigated include mixing ratio, equivalent potential temperature, moisture convergence and integrated moisture convergence. A case study approach is employed using the LIMEX85 mesoscale data set collected by the Alberta Research Council Hail Project in July 1985. Two regions of analysis are defined which provide a spatial reference. Irregularly spaced data are gridded and contoured to delineate changes in the moisture fields for two analysis regions located in Alberta. Contoured fields of the moisture parameters are provided for six time periods and five pressure levels. Additional contoured depictions in semi diurnal, and cross-sectional forms further describe the evolution of the moisture fields over the case study areas. Synoptic charts, radar imagery, and tephigrams furnish further tools to typify the convective conditions over the analysis regions.

The analysis relates the observed convective activity from the radar imagery and the changing moisture fields to delineate the conditions of convective storms development. Significant moisture sources at the surface are observed which fuel the storm growth. Mid-level moisture is sufficient to mitigate cloud erosion by the entrainment of the ambient wind field. Moisture convergence is calculated and observed to be a storm precursor by 2 to 4 hours. The vertical stratification of equivalent potential temperature indicates the presence of conditional convective instability. Regions of storm formation are characterised by high surface values of equivalent potential temperature. Moistening of the boundary layer is observed at storm maturation and decay. The mesoscale analysis based on twenty to one hundred kilometre grid intervals reveal moisture sources and transport, which support a link between the observed developing convective activity and the surrounding environment moisture fields. The mesoscale analysis reveals evidence of surface moisture convergence and large negative equivalent potential temperature gradients in the regions which fostered convective storm growth. Supporting error analysis and gridding sensitivity tests have also been undertaken.

ACKNOWLEDGEMENTS

CONVECTIVE STORMS AND MOISTURE FIELDS IN LIMEX85: A CASE STUDY

Table of Contents

LIST OF TABLES

LIST OF FIGURES

LIST OF ABBREVIATIONS AND SYMBOLS

AES	Atmospheric Environment Service
ARC	Alberta Research Council
ASL	Above Sea-level
°C	degrees Celsius
CCOPE	Co-operative Convective Precipitation Experiment
IMC	integrated moisture convergence
LCL	lifting condensation level
LIMEX85	Limestone Mountain Experiment 1985
K	degrees Kelvin
MC	moisture convergence
MDT	Mountain Daylight time
NCAR	National Centre for Atmospheric Research
NHRE	National Hail Research Equipment
NOAA	National Oceanic and Atmospheric Administration
NSSL	National Severe Storms Laboratory
RH	relative humidity
SESAME	Severe Environmental Storms And Mesoscale Experiment
T_c	isentropic condensation temperature
T_d	dew point temperature
T_e	adiabatic equivalent temperature
UTC	Co-ordinated Universal Time (formerly GMT)
Vn	Horizontal wind velocity vector
cm	Centimeter
dBZ	radar reflectively factor in decibels
e_w	saturation vapour pressure
g/kg	grams per kilogram
mb	millibar
mb g/kg hr	millibar grams/kilogram hour
p	pressure
r	mixing ratio
u	meridional wind component
v	zonal wind component
θe	equivalent potential temperature
γ	dry adiabatic lapse rate
λ	longitude
θ	latitude
θn	wind direction
∇	Vector Differential Operator
Δ	Delta (a spatial interval)
Σ	Summation sign
$\dfrac{\partial u}{\partial x}$	The partial derivative of the zonal wind velocity component with respect to x (distance in the east-west direction)
$\dfrac{\partial v}{\partial y}$	The partial derivative of the meridional wind velocity component with respect to y (distance in the north-south direction)

CHAPTER 1.

INTRODUCTION

Many researchers have emphasized that a knowledge of the evolution and transport of atmospheric moisture fields is paramount for thunderstorm insight and prediction (Mahrt, 1977; Modahl, 1979 and Park and Sikdar, 1977). While investigating statistical discriminators between storms which yielded hail and those which did not, Mahrt (1977) states that a modest decrease of moisture with height causes a gradient of energy which offers a distinct advantage to organized moist convention. Modahl (1979) states that a greater knowledge of the low-level winds and their resulting influence on the moisture content are systematically different for hail and no-hail convective events. The primary objective of the Park and Sikdar (1971) research was to describe the time evolution of the wind, temperature and moisture fields from the pre-convective state to the storm period with an emphasis on the low-level variations in cloud regions and adjacent cloud free regions. The moisture field plays an important role in initiating convection, determining the intensity and duration of storms and in determining the amount of resulting rainfall. Moisture sources at the surface provide humid air which is less dense than dry air at the same temperature and pressure. This moist air tends to rise and thereby can act as a trigger to initiate convection. Once condensation occurs, diabatic heat is released and the upward motion of the air parcel is stimulated, further assisting the initiation of convection processes.

The intensity of a storm is generally quantified by the magnitudes of the precipitation rate and or the updraft wind speeds. For steady state conditions the rainfall rate is directly proportional to the updraft wind speed. The amount of available moisture in

the lower boundary layer regulates the amount of condensation which results in the amount of upward buoyancy and thus the storm updraft.

The amount of moisture in the mid-layers affects the duration of the storm. For dry conditions, mixing between cloudy and environmental air can dry out the convective storm. For moist conditions, however, cloud entrainment is less constructive in terms of potential storm development.

Horizontal gradients in the boundary layer moisture content are associated with horizontal gradients in effective air density because moist air is lighter than dry air at the same temperature and pressure. This difference in effective air density tends to form a circulation with rising air in the moist flank and descending air in the dry flank. This may form a weak "seabreeze" type circulation driven by horizontal moisture differences and assist the triggering of convection processes.

Synoptic scale upper air data (with a typical station spacing of 500 km) collected twice daily around the globe cannot adequately resolve moisture fields linked to thunderstorm formation. A finer resolution in time and space is required to resolve the changes in the moisture fields associated with thunderstorm development. Smaller scale networks can provide the research data required to study sub-synoptic scale (mesoscale) phenomena such as thunderstorms. A mesoscale experiment (LIMEX85) carried out by the Alberta Research Council Hail Project in the summer of 1985 sought to collect mesoscale data appropriate for thunderstorm research. This experiment was conducted over a region of roughly 200 by 200 km^2 in the foothills and mountains of southwestern Alberta.

1.1   OBJECTIVES AND OUTLINE OF THESIS

The primary scientific objectives of this research are to:

2

(1) Analyze surface observations and radiosonde data to obtain a three-dimensional field of atmospheric moisture at two-hour time intervals before and during the evolution of a severe convective storm.

(2) Relate the evolution of the observed moisture fields spatially with the storm development at the same time as depicted by radar.

(3) Investigate the usefulness of computing moisture convergence on a 20 km spatial grid in predicting thunderstorm formation.

(4) Look for evidence of moistening of the outflow boundary regions during the storm's maturing and decaying phases.

This research was undertaken using a case study approach based on data collected by the Alberta Research Council (ARC) during the LIMEX85 mesoscale upper air experiment (Strong, 1989). The case study described here focuses on data collected on July 11, 1985. In order to characterize the moisture fields, contoured depictions of mixing ratio, equivalent potential temperature, moisture convergence and integrated moisture convergence have been prepared. AES synoptic charts and ARC radar imagery are included to further delineate the larger scale meteorological conditions and the observed thunderstorm features.

The depictions of the aforementioned variables take one the following forms:

- Tephigrams

- Radar images

- Synoptic weather maps

- Contoured moisture fields in a horizontal plane for a specific time and pressure level

- Contoured moisture fields in a vertical plane for a specific time

- Contoured moisture fields in the vertical plane for a specific place in time

- Moisture flux calculations

Since the moisture for thunderstorm growth is often concentrated in the first few hundred metres of the surface layer, the well-mixed moist layer typical of

3

thunderstorms must arise from moisture transfer upward from the surface layer. The supply of surface moisture is often localized in a region of maximum surface moisture convergence, providing an adequate source of moisture for storm development. By analyzing the developing features of the atmospheric moisture fields and the associated wind and temperature fields in time, a "snapshot" by "snapshot" illustration of the moisture field evolution is obtained.

1.2   MOISTURE IN THE ATMOSPHERE AND THUNDERSTORMS

The earth's atmosphere contains an average storage of water equivalent to a 2.5 cm layer for the entire surface area (Barry and Chorley, 1974). This water comprises approximately 3% of the atmosphere by weight and 4% by volume. This atmospheric moisture is in a constant state of change as the processes of evaporation, condensation and precipitation take it though the hydrologic cycle. Cloud and subsequent thunderstorms are made up of one or more cells of convective circulation, with updraft areas and regions of compensating downward air transport (Rogers, 1979).

The life cycle of a thunderstorm cell is described by Rogers (1979) as a three stage process, with the stages delineated by the predominant direction and magnitude of the vertical wind fields. The three stages are referred to as the cumulus, mature, and dissipating stages. The cumulus stage has updrafts throughout most of the cell. At the mature stage, the presence of both updrafts and downdrafts is evident. During the dissipating stage, the cell is dominated by weak downdrafts. The initial updraft phase causes the storm cell to grow as air is entrained in the region of the updraft. Large amounts of water are condensed and begin to fall as precipitation. The falling drops initiate evaporative cooling and viscous drag on the surrounding air creating a downdraft. The downdraft reaches the ground as a cold core and spreads over the surface interfering with the updraft region as the mature stage is reached. A depleted updraft stops the supply of moisture and the subsequent rainfall. This weakens the downdraft as the cycle finally dies out. Rogers (1979) states that the most destructive thunderstorms are those in which the updraft and downdraft regions do not interfere

4

with each other, but become more organized thereby sustaining large, long-lasting convective circulations.

Cotton (1990) presents a very complete discussion concerning the atmospheric conditions associated with convective storm development. This discussion includes a conceptual model and the delineation of the necessary atmospheric conditions for severe storm convection and subsequent storm development. The first of these necessary conditions is a source of boundary layer moisture. Without an adequate boundary layer moisture source a prospective storm will have insufficient moisture to develop at all. The next necessary condition is the existence of triggering mechanisms to initiate convective storm development. Physically these are mechanisms which bring about the onset of updrafts to carry the boundary layer moisture into cloud formations. These mechanisms include such effects as differential surface heating, topographic feature wind field modification, and zones of convergence along a cold front. Another condition required for storm development is the absence of a dry environment at or near the cloud base. This precludes the developing cloud from being eroded due to environmental air entrainment about its base and edges. The atmospheric vertical profile of temperature and moisture must indicate convective instability, conditional instability and convective available potential energy in order for the storm to develop. Shear in the ambient wind field in the storm environment tends to organize the relative positions of regions of updraft and downdrafts in a constructive manner. Unidirectional shear results in a successive generation of new convective cells downwind of the existing ones and thereby produces a so-called multicell storm. If the wind direction changes with height (veering and backing) the updraft and downdraft structure becomes separated and spirals essentially with altitude. For strong convective instability and strong veering of the ambient wind field a long-lasting isolated updraft is present forming a super-cell storm which often produces large hailstones. The final condition is the existence of a capping-lid just below convective instability level to allow for a build up of convective instability.

In terms of the frequently depicted atmospheric vertical profile parameters temperature, moisture and wind, the following conditions required for storm formation

5

are related. The temperature profile determines convective instability and the existence and location of the capping lid. The moisture profile (dew point temperature) determines the amount of boundary layer moisture available for precipitation formation, the amount of convective instability and the absence of upper dry levels which suppress cloud development through the entrainment of dry air. The wind profile gives the amount of wind shear which determines the separation of updrafts and downdrafts and thereby the duration of the storm. If the regions of updraft and downdrafts coincide spatially, convection stops. Veering of the wind combined with shear provides favourable conditions for super-cell storm formation.

1.3   MESCOSCALE FIELD EXPERIMENTS

Several mesoscale upper air experiments have been carried out in the United States. These experiments, their locations and the principal investigative groups are listed in Table 1.1.

The NSSL and SESAME mesoscale networks were designed to study meteorological aspects of the severe storm environment (Strong, 1986). Mesoscale research using these data sets has provided a wealth of information on the severe storm environment. This information assisted in the development of theoretical storm models, computer model simulation, and severe storm forecasting. In order to verify some of the results of these studies for the Alberta scenario, and to test some new concepts, Strong (1989) carried out a number of small mesoscale experiments between 1980 and 1985, collectively called the Limestone Mountain Experiments, culminating in LIMEX85. One case study from LIMEX85 is the focus of this thesis.

The investigative efforts of a few of the principal thunderstorm researchers and the data sets involved are summarized in the following paragraphs.

TABLE 1.1   Previous mesoscale upper air experiments with locations and research groups.

Experiment	Location	Research Group
SESAME[a]-AVE[b]-IV	Central U.S.	NASA[e] and NSSL[f]
SESAME-AVE-V	Central U.S.	NASA and NSSL
CCOPE[c]	Miles City, Montana	NCAR[g]
NHRE[d]	Colorado	NCAR

[a]   Severe Environmental Storms and Mesoscale Experiment

[b]   Area Variability Experiment

[c]   Cooperative Convective Precipitation Experiment

[d]   National Hail Research Experiment of NCAR

[e]   National Aeronautical and Space Administration

[f]   National Severe Storms Laboratory

[g]   National Center for Atmospheric Research

Braham (1952) sought to determine the water and energy budgets of thunderstorms. Using the University of Chicago and U.S. Weather Bureau co-funded thunderstorm research project data, he looked at the nature and intensity of the moisture sources and sinks, and the moisture flux and redistribution of moisture as a result of the thunderstorm process. In general, the source of moisture was identified as the water-vapor content of the air flowing into the storm. This water-vapor is converted in part to liquid and frozen water due to the expansional cooling of the air mass, as it is carried vertically by the updraft. Some condensed water falls out as rain while the remaining portion is evaporated from the sides of the cloud, or in the downdraft.

In 1977, Mahrt (1977) analysed the data collected by the National Hail Research Experiment (NHRE) at Sterling, Colorado. He sought to statistically characterize and compare early afternoon environmental conditions prior to hail-producing

7

thunderstorms, and those of less severe moist convection. This analysis showed that hail-producing thunderstorms were formed from particularly thin mixed layers as contrasted to non-hail producing storms. The energy required to initiate convection was greater than normal for hail-producing thunderstorms. Mahrt (1977) also found the inversion capping lid prior to storm formation was stronger on hail days.

Modahl (1979) used the same NHRE data set from Colorado and tried to characterize the evolution of the mean low-level wind and moisture content fields. Days in which hail was experienced showed shallow easterly and southerly winds. Non-hail days showed westerly winds. Moisture content increases were linked to the easterly and southerly wind components.

Data from the NSSL mesoscale network in Oklahoma during May 1976 was the focus of the research by Park and Sikdar (1982). Their main objective was to depict the kinematic and thermodynamic structure of the observed storm. They noted the existence of a pre-storm shallow mixed layer capped by a strong inversion layer. When the inversion layer was eliminated by the growth of the mixed layer, a storm violently developed. Warm moist air from the southeast converged and the development of intense localized convection ensued. The convective updraft conditions observed in the southeast were contrasted by a sinking motion to the northwest. This was defined as a feedback mechanism between the storm and its environment.

Research by Carlson (1979), and Carlson et al. (1983) using 1979 SESAME field program data focused on the development of a conceptual model for the evolution of thunderstorms. A combination of air flow and topography can produce a restraining inversion or capping lid which focuses the location of severe storms. This vertical stratification suppresses convection and allows for an increase of latent instability in the boundary layer. The removal of the lid due to surface heating and large scale vertical motion results in strong convection.

Maddox (1983) completed an objective analysis of ten convective complexes using data collected by NOAA in Colorado from 1975 to 1977. This research indicated that

8

the thunderstorms develop within a region of mesoscale surface moisture convergence, and upwind vertical motion over the plains. The vertical motions are primarily due to strong low-level warm advection. The thunderstorms interact with their environments by moistening a deep tropospheric layer. The demise of such convective storms is usually typified by the development of a more stable, less convectively favourable environment.

Fuelberg and Printy (1983) used rawinsonde data from the 1979 AVE-SESAME experiment to diagnose atmospheric variability in the environment of convective storms. They observed temperature increases in the upper troposphere and cooling in the lower stratosphere and near the surface. The wind field was observed to strengthen north of the convective area and a decrease of jet-level winds was noted southeast of the storms. Strong upper level divergence, low-level convergence and upward air motions developed after storm initiation. They concluded that many of the observed atmospheric variations were produced by the convective storms.

Kuo and Anthes (1984) analyzed the effect of mid-latitude organized convection on its environment by diagnosing the associated mesoscale heat and moisture budgets over the region using 1979 AVE-SESAME data. They found a close correspondence between vertically integrated diagnostic heat sources and moisture sinks with observed rainfall rates especially when the averages were computed using a larger spatial scale than the average station spacing. The moisture budget showed a moistening of the environment before a squall line developed and a drying as the squall line moved out of the region. They also found a high correlation between rainfall rate and large scale moisture convergence.

Fuelberg, Lin and Chang (1986) calculated moisture budgets using AVE-SESAME V data prior to, during, and after the convective outbreak. Their investigative domain included convective and non-convective regions to facilitate a comparison. The storm environment was characterized by strong low-level horizontal moisture convergence and upward transport. Temporal variability was consistent with previously investigated environmental variations near convective regions. This supports the existence of

feedback processes occurring between the storms and the surrounding environment. Moisture budget calculations had their greatest magnitude near the storms.

Heimbach and Engel (1987) used CCOPE data to examine alternatives to large meso-networks with station spacings on the order of 10 to 20 km. They found that periods lacking convective activity showed limited or no convergence and vorticity trends. Convective periods showed sinusoidal time plots of the derived parameters with periods of 1 - 2 hours. Variance increased just prior to and after convection.

McCorcle (1988) investigated the effect of soil moisture and evaporation on a diurnal temporal scale on the Great Plains nocturnal jet. This was accomplished by embedding a soil hydrology module into a boundary-layer numerical model. Spring time data were used to initialize to forecast mode. This addition yielded forecasts of the vertical and horizontal wind fields which were well correlated with the timing and location of the observed wind field features within the regions of observed convection. The response of the model demonstrated the importance of including spatial distributions of soil moisture in such forecast models.

1.3.1 Severe Summertime Convection over the LIMEX85 Region

In his investigation of scale interactions and the convective process, Strong (1986) suggests that a typical storm producing situation over Alberta has the following components:

- A southwest flow aloft preceding a shortwave trough.

- A surface low in southern Alberta.

- An easterly component of upslope flow in the boundary layer resulting in localized moisture convergence over the foothills.

- An unstable air mass.

- The prestorm existence of a capping inversion or lid.

10

In a separate investigation into the LIMEX85 data set, Honch (1989) found the presence of strong positive vertical motion five hours prior to the storm events. The cellular structure of the vertical velocity fields displayed good spatial continuity, but poor temporal continuity. A strong surface convergence was aligned along the Foothills of Alberta.

Smith and Yau (1991) also used the LIMEX85 data set to investigate convective activity over Alberta. They concluded that under generally clear skies, cumulus convection begins over the Alberta Foothills when strong surface heating removes the capping lid. Convective outbreaks occur with cooling aloft and when an approaching synoptic scale upper-level trough is in phase with strong surface heating in the Alberta Foothills. East and northeast surface winds transport moist air from the plains to the Foothills. These processes yield localized deep destabilization and strong upslope moisture transport.

Rogers and Sakellarion (1986) used the radar reflectivity patterns of three large Alberta hail storms to determine precipitation content and moisture outflow content as functions of time. They found that the maximum hourly precipitation generation rate and the total outflow exhibited two periods of maximum separated by 30 - 45 minutes. Their three storm sample was deemed too small to determine if storm differences were due to measurable environmental factors such as wind shear and stability or whether the differences are insignificant compared to the natural variability found within the storm environments which develop under the same conditions.

Smith and Yau (1987) investigated the role of topography in the genesis of hail storms in Alberta using two-dimensional mixed-layer model of the planetary boundary layer. High resolution topography was input into the model along with varying geostrophic winds. They found that south and southeast winds favour the outbreak of widespread severe convection. They concluded that topographic forcing is a major factor in determining the location of hail storm genesis in southern Alberta. A comparison of the model generated results and a real time data set showed a close

correspondence between the locations of model generated zones of positive vertical motion and those of the early radar echoes.

Honch and Strong (1990) used the LIMEX85 data set to test the validity of some dynamical aspects of a multi-scale conceptual model of thunderstorm gene...is applied to the Alberta region. Vertical velocity fields and surface divergence fields are calculated and discussed in relation to radar and satellite data sets. Their findings show the presence of strong positive vertical motions in the lower to mid troposphere 5 - 6 hours prior to storm formation. Strong surface convergence in the lee of the Rocky Mountains supports the premise that links surface convergence with thunderstorm initiation.

In summary, the authors which have worked on the LIMEX85 data set have identified three primary conditions appear to be required for the formation of thunderstorms. The first is a source of available moisture in the lower troposphere and a convergence or focusing of this moisture source. This convergence and focusing of the surface moisture is facilitated by transport due to the surface wind field and the trapping action of the pre-convective capping inversion or lid.

The second condition is a state of instability in the lower and mid troposphere producing rising thermals. The kinetic energy associated with these rising thermals must be sufficient for the moisture to attain a level where condensation can take place. The instability resulting in the rise of the air parcels is due to the temperature difference between the air parcels and in the neighbouring air mass. As a moist air parcel rises, the pressure is reduced, thereby expanding and adiabatically cooling the parcel. If enough cooling is generated, the air mass becomes saturated, resulting in condensation and cloud formation. Sufficient vertical displacement will cause the parcel to freely convect upwards.

The third and final requirement is a source of ascent to assist in the lifting of the air parcels. These vertical velocities may arise from a combination of thermodynamical

and dynamical processes, such as low-level convergence, differential surface heating, orographic lift, and ascent along frontal air mass discontinuities.

Of the conditions required for the development of thunderstorms, it is evident that the transport of moisture from the boundary layer to the mid troposphere is a key component in the process. This research will focus on characterizing the atmospheric moisture content and its horizontal convergence, using a case study approach.

1.4 MOISTURE MEASURES

A variety of moisture measures exist to quantify the moisture content of the atmosphere. These include vapor pressure, vapor density, mixing ratio, specific humidity, relative humidity, and virtual temperature as outlined in Rogers (1979). The vapor pressure is the partial pressure due to the molecules of a given vapor. Vapor density is the ratio of the mass of water vapor present to the total volume of the air/water vapor mixture. Mixing ratio is the dimensionless ratio of the mass of the water vapor to the mass of the dry air. Specific humidity is the dimensionless ratio of the water vapor to the total mass. Relative humidity is the dimensionless ratio of the vapor pressure to the saturation vapor pressure. The virtual temperature is the temperature of a dry air mass which has the same density and pressure as the moist air. The moisture measures used in this analysis are described further as follows.

1.4.1 Mixing Ratio

The mass of water vapor in grams per kilogram of air is called the mixing ratio. It usually is denoted by the symbol r [g of H_2O/kg of dry air]. Given the dew point temperature (t_d) and pressure (p), the mixing ratio can be calculated as follows (Iribarne and Godson, 1981):

13

$$r \, [\text{g/kg}] = \frac{1000 \, \varepsilon \, e_w}{(p - e_w)} \tag{1.1}$$

where $\varepsilon = R_d/R_v = 287.05 \, [\text{J/kg K}]/461.51 \, [\text{J/kg K}] = 0.62198$

   e_w = saturation vapor pressure at t_d

   p = atmospheric pressure

For the purposes of this research, the vapor pressures have been computed using an empirical polynomial formulation suggested by Lowe (1976). The polynomial relationship is valid over the temperature range of -50 to +50 °C and is accurate to within 1%.

$$e_w = a_0 + t_d \, (a_1 + t_d \, (a_2 + t_d \, (a_3 + t_d \, (a_4 + t_d \, (a_5 + t_d \, (a_6)))))) \tag{1.2}$$

where t_d is dew point temperature in °C [-50, 50] and:

$$a_0 = 6.107799961$$
$$a_1 = 4.436518521 \times 10^{-1}$$
$$a_2 = 1.428945805 \times 10^{-2}$$
$$a_3 = 2.650648471 \times 10^{-4}$$
$$a_4 = 3.031240396 \times 10^{-6}$$
$$a_5 = 2.034080948 \times 10^{-8}$$
$$a_6 = 6.136820929 \times 10^{-11}$$

The nested terms in brackets allow for a more efficient computation than the expansion terms.

1.4.2 Moisture Convergence

There are two basic methods for the determination of moisture convergence. Moisture convergence can be computed using the flux form by:

$$MC = \frac{\partial}{\partial x}(ur) + \frac{\partial}{\partial y}(vr)$$

or alternatively in the advective form by:

$$MC = u\frac{\partial r}{\partial x} + r\frac{\partial u}{\partial x} + v\frac{\partial r}{\partial y} + r\frac{\partial v}{\partial y}$$
$$\text{advection} \quad \text{convergence} \quad \text{advection} \quad \text{convergence}$$

where r is the mixing ratio, u and v the zonal and meridional wind components and x and y denote the easterly and northerly coordinates.

In this analysis I choose to use a finite-difference approximation of the advective form of calculating moisture convergence as outlined in Moore (1980). The choice of this particular approximation was based on the ease of its application computationally and because its form allows for a comparison of the relative magnitudes of moisture advection terms with the convergence terms. In the analysis, however, only the total moisture convergence is examined. It should be pointed out that the finite-difference approximation of the flux form can be less sensitive to computational inaccuracies because the flux form conserves the total moisture (see Holton (1979) p. 189). One other option is possible in applying the finite-difference forms of these moisture convergence equations. This is the use of a staggered grid. U and V values are displaced by $\frac{\Delta}{2}$ in order to more fully resolve the wind fields. Although this choice was not invoked in the analysis, it may have provided a attractive alternative to the scheme which was chosen.

In order to quantify the convergence of moisture with reference to a specific point in space, the quantity moisture convergence can be used. Moisture convergence values were computed using a finite-difference scheme referenced in Moore (1980):

$$= -\frac{(m^2_{i,j})}{2\Delta} \left[r_{i,j} \left(\frac{u}{m}_{\,i+1,j} - \frac{u}{m}_{\,i-1,j} + \frac{v}{m}_{\,i,j+1} - \frac{v}{m}_{\,i,j-1} \right) \right.$$

$$\left. + \frac{u}{m}_{\,i,j} \left(r_{i+1,j} - r_{i-1,j} \right) + \frac{v}{m}_{\,i,j} \left(r_{i,j+1} - r_{i,j-1} \right) \right] \qquad (1.3)$$

where: r is mixing ratio; u and v are the zonal and meridional wind components, respectively. Δ is the grid interval; and m is the image map scale factor. The unit for moisture convergence is [g/kg h]. The basis for the moisture convergence formula is as follows:

Given a grid of nine equally spaced points in the (x, y) system with centre point given the indices (i, j), as shown in Figure 1.1.
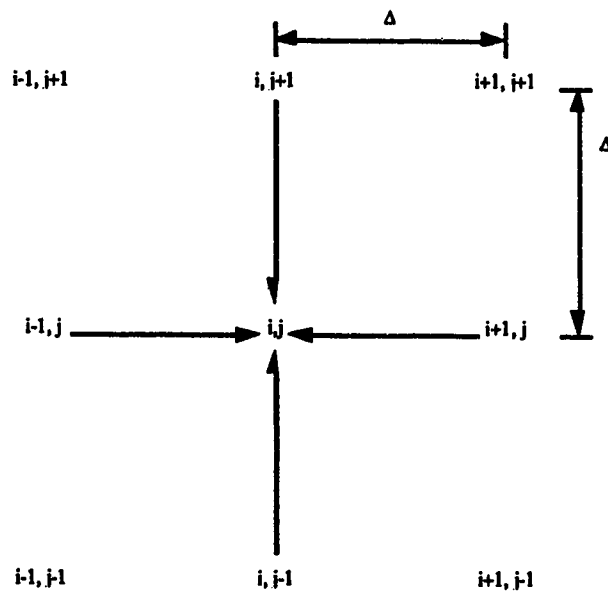
FIGURE 1.1 Nine grid point moisture convergence.

The divergence and convergence of the velocity field in the x-y plane are defined as:

- divergence $= \nabla \cdot Vh = \dfrac{\partial u}{\partial x} + \dfrac{\partial v}{\partial y}$ (1.4)

- convergence $= -\nabla \cdot Vh = -\dfrac{\partial u}{\partial x} - \dfrac{\partial v}{\partial y}$ (1.5)

$$\dfrac{\partial u}{\partial x} \simeq \dfrac{(u_{i+1,j} - u_{i-1,j})}{2\Delta}$$

(1.6)

$$\dfrac{\partial v}{\partial y} \simeq \dfrac{(v_{i,j+1} - v_{i,j-1})}{2\Delta}$$

The moisture convergence about the (i, j) grid point has the following terms:

$$\dfrac{(-r_{ij}\ u_{i+1,j})}{2\Delta}$$

$$\dfrac{(+r_{ij}\ u_{i-1,j})}{2\Delta}$$

$$\dfrac{(-r_{ij}\ v_{i,j+1})}{2\Delta}$$

$$\dfrac{(+r_{ij}\ v_{i,j-1})}{2\Delta}$$

$$\dfrac{(-r_{i+1,j}\ u_{ij})}{2\Delta}$$

$$\dfrac{(+r_{i-1,j}\ u_{ij})}{2\Delta}$$

$$\dfrac{(-r_{i,j+1}\ v_{ij})}{2\Delta}$$

$$\dfrac{(+r_{i,j-1}\ v_{ij})}{2\Delta}$$

For purposes of this thesis, all depictions of moisture convergence use an image map scale factor of 1. Therefore, summing and rearranging gives:

$$MC = -\dfrac{1}{2\Delta} [r_{ij}\ (u_{i+1,j} - u_{i-1,j} + v_{i,j+1} - v_{i,j-1}) + u_{ij}\ (r_{i+1,j} - r_{i-1,j}) + v_{ij}\ (r_{i,j+1} - r_{i,j-1})]$$ (1.7)

17

1.4.3 Integrated Moisture Convergence

The third moisture index used to characterize the moisture fields is integrated moisture convergence. The integration takes place in the vertical with respect to pressure (Moore, 1980).

$$IMC = \int_{P_B}^{P_T} MC \, dP \qquad (1.8)$$

where:
- IMC – Integrated moisture convergence
- MC – Moisture convergence.

The units of IMC are [g mb/h kg]. The integral was approximated as a sum of four trapezoidal approximations. The average MC value in the four layers (surface to 850 mb, 850 mb to 700 mb, 700 mb to 600 mb and 600 mb to 500 mb) was multiplied by the layer pressure difference and then these were summed to give the IMC value. If the surface pressure for a particular point was less than 850 mb, the surface to 850 mb layer yielded a zero IMC contribution to the sum and the upper pressure level of the second layer was changed to reflect the new surface pressure level. IMC reflects the net moisture convergence in a vertical column between the pressure levels p_T and p_B. For the purposes of these calculations, p_B was defined as the surface pressure and p_T the 500 mb level. The 850, 700 and 600 mb pressure levels were also used in the computations to yield a sum of four integrated moisture convergence values in the vertical. The 500 mb level was used as the top level due to a high proportion of missing data above this level, and large proportions of the total column moisture lying below the 500 mb level. This is justified by the fact that more than 90% of the water vapor in a vertically oriented column lies below the 500 mb level.

For a sample of LIMEX85 upper air stations at 1400 UTC on July 11, 1985, the percentage of column moisture below 500 mb is given in Table 1.2.

18

TABLE 1.2   Percentage of total column moisture lying below the 500 mb level for July
11, 1985, 1400 UTC.

Station Identifier	% of Total Column Moisture
ACR	94.2
AEL	95.2
AML	90.3
AQF	94.7
ARM	93.1
AYC	94.0
LMW	89.8
Average	93.0

1.4.4 Equivalent Potential Temperature

The fourth indirect measurement of atmospheric moisture used in this analysis is equivalent potential temperature (θe). It is defined as the temperature a parcel of air would have if taken from its adiabatic equivalent temperature to a pressure of 1000 mb in a dry adiabatic process (Rogers, 1979). The adiabatic equivalent temperature (T_{ae}) is defined as the temperature an air parcel would have if it underwent dry-adiabatic expansion until saturated, followed by pseudo-adiabatic expansion until all the moisture condensed out, and finally, dry-adiabatic compression to the initial pressure of (Huschke, 1970). The parameter θe is conserved for both dry and saturated adiabatic processes. To compute the equivalent potential temperature, the following equations were used (Rogers, 1979; Iribarne and Godson, 1981):

$$\theta e = T_{ae} \left(\frac{1000}{p} \right)^{\kappa}$$ (1.9)

where: $\kappa = \dfrac{1005 \ [J/kg \ K] - 718 \ [J/kg \ K]}{1005 \ [J/kg \ K]} = 0.2856$

19

$$T_{ae} = T \cdot e^{\left(\frac{L_v r}{C_p T_c}\right)}$$

(1.10)

where:
- L_v is the latent heat of vaporization = 2.501×10^6 [J/kg]
- r is the mixing ratio [g of H_2O/kg of air]
- T_c is the isentropic condensation temperature = $T - \gamma H_{LCL}$
- γ is the dry adiabatic lapse rate = 9.76 [K/gpkm] and
- H_{LCL} is the level of the lifting condensation level = 0.12 ($T - T_d$)
- T is the ambient temperature and T_d is the dew point temperature.

Equivalent potential temperature values reflect the combined influence of temperature and moisture. Therefore it is only a pure indicator of the spatial variation in moisture effects if the temperature field is uniform.

CHAPTER 2.

DATA SOURCES

2.0 INTRODUCTION

In order to characterize the evolution of the moisture fields for the case study day July 11, 1985, the incorporation of several different types of data was used. These include data collected by the Alberta Research Council LIMEX85 experiment, synoptic scale data collected by the Atmospheric Environment Service, and Alberta Forestry data.

LIMEX85 data were the key source of information for this study due to the temporal and spatial scales of two hours and 50 km, respectively. This data set also has the advantage of having the vertical component available which facilitates an upper air analysis. The LIMEX85 data set is also augmented with S-band radar images which were processed at the ARC facility in Edmonton, Alberta. The radar images make it possible to locate thunderstorms near their inception and to follow their tracks and evolution. By showing the location and timing of storm events based on radar images, an analysis focusing on the relationships between storms and their surrounding moisture fields can be initiated. Synoptic scale and Alberta forestry data are generally limited to the surface based measurements and hence were used to enhance the surface data analysis.

2.1 LIMEX85 DATA

The Alberta Research Council Hail Project undertook the Limestone Mountain Experiment (LIMEX85) over a region of southwestern Alberta during July 1985. This mesoscale upper air experiment collected data appropriate to mesoscale convective

21

process research (Strong, 1989). The archived data sets were described by Strong (1989).

The LIMEX85 upper air data were the main source of mesoscale upper air moisture data. Nine upper air stations in the LIMEX85 field study area collected upper air data at two-hour intervals commencing at 1400 UTC (0800 MDT). The locations and elevations of these stations, along with the upper air station at Stony Plain, Alberta operated by AES, are given in Table 2.1. A map of the LIMEX85 experiment area, including topographic contours, can be found in Figure 2.1 (from Brennand and Mason, 1986). The upper air data were pre-processed by the ARC UPPERAIR software in which linear interpolation was used to output the data fields at 10 mb increments up to 700 mb and 50 mb levels above 700 mb.

The LIMEX85 special surface weather sites are listed in Table 2.2. The LIMEX85 experiment also measured surface and radar data during the course of its execution. Table 2.3 provides a list of the variables collected, frequency of collection and data type. No pre-processing of the LIMEX85 surface data was performed.

TABLE 2.1   LIMEX85 upper air stations and Stony Plain upper air station.

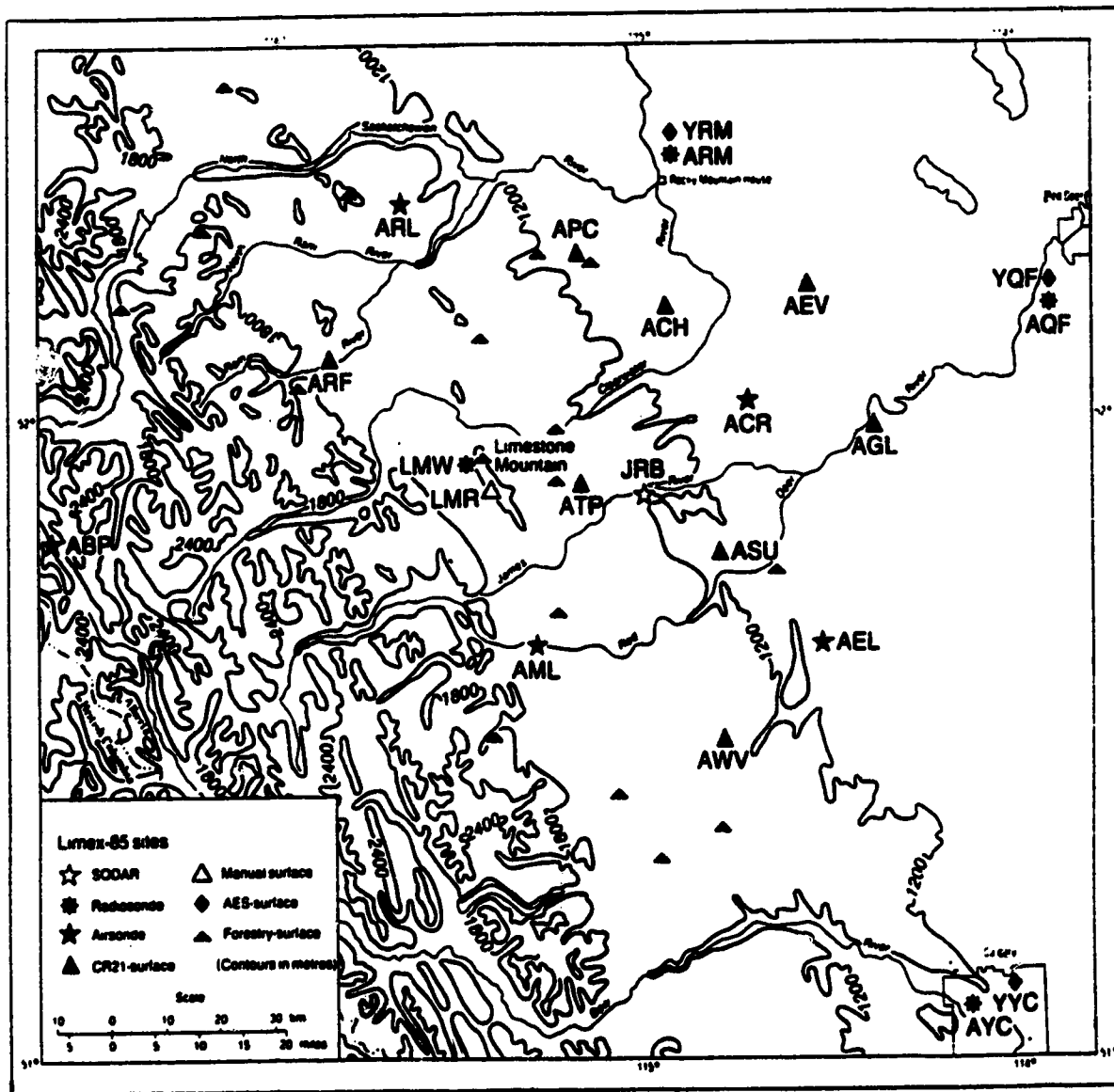| Station ID	Latitude (degrees N)	Longitude (degrees W)	Elevation (m ASL)	Name
CAQF	52.18	113.90	900	Red Deer
CARM	52.43	114.92	988	Rocky Mountain House
CAYC	51.08	114.13	1114	Calgary
CLMW	51.95	115.48	1506	Limestone Mountain
CABP	51.81	116.58	1710	Bow Pass
CACR	52.03	114.42	1068	Caroline
CAEL	51.66	114.51	1130	Elkton
CAML	51.66	115.29	1442	Mountainaire Lodge
CARL	52.34	115.65	1294	Ram Lookout
CWEG	53.55	114.10	766	Stony Plain

Figure 2.1   LIMEX85 sites with contours of topographic elevations in meters.

TABLE 2.2   Special LIMEX85 surface weather sites.

Station ID	Latitude (degrees N)	Longitude (degrees W)	Elevation (m ASL)	Name
AEV	52.22	114.55	1009	Evergreen
AGL	51.99	114.38	1012	Glennifer Lake
APC	52.18	115.36	1406	Prairie Creek
ARF	52.09	115.85	1618	Ram Falls Ranger Station
ASU	51.79	114.79	1167	Sundre West
ATP	51.90	115.16	1380	Tee-Pee Pole Creek
AWV	51.50	114.64	1313	Water Valley
ACH	52.18	114.91	1088	Cheddarville West
LMR	51.90	114.40	2121	Limestone Mountain Ridge (field base)

TABLE 2.3   LIMEX85 data collected and data collection frequency.

Data Type	Meteorological Variables	Frequency
LIMEX85 Automatic Surface Stations	t, t_d, u, v, θ_n	5 minutes
LIMEX85 Upper Air Data	p, t, t_d, u, v, θ_n, θ_e, r, RH	1-3 hours
LIMEX85 Radar Data	Radar Reflectivity Factor (dBZ) Minimum Angle and Maximum Angle in a Plan Position Indicator Form	$\approx$ 30 minutes
Synoptic Surface Sites	p, t, t_d, wd, ws	1 hour

24

2.2   FORESTRY DATA

Alberta Forestry Lookout sites take weather observations at 1300 and 1900 UTC each day during the summer. The variables measured include p, t, t_d, u, v, and θ_n. A list of these sites is presented in Table 2.4. In order to include these data in the analysis, the values of each parameter were linearly interpolated and extrapolated to the 1200, 1400, 1800 and 2000 UTC analysis times. This method was suggested by Dr. G. Strong of the National Hydrology Research Center.

2.3   AES SYNOPTIC DATA

The main source of surface data other than LIMEX85 site was AES Synoptic Surface data. Sites from British Columbia, Alberta and Saskatchewan are outlined in Tables 2.5, 2.6 and 2.7, respectively. Data collected include date, time, p, t, t_d, u, v, and θ_e every hour.

Synoptic chart analysis from the AES microfilm archives at the University of Alberta were also included in the analysis in order to define the synoptic conditions during the case study.

TABLE 2.4 Alberta Forestry sites in the vicinity of the LIMEX85 study region.

Station ID	Latitude	Longitude	Elevation (m ASL)	Name
FCW	51.99	115.24	1279	Clearwater
F40	51.88	115.74	1615	40-Mile Flats
FAF	52.80	114.82	1029	Alder Flats
FAU	52.65	115.72	1341	Aurora
FBY	52.53	116.13	2090	Baldy
FBL	52.13	116.43	1893	Baseline
FBT	52.77	116.33	1516	Blackstone
FBZ	53.04	115.44	1085	Brazeau
FND	52.48	116.08	1326	Nordegg
FBH	51.70	115.20	1985	Blue Hill
FBK	51.96	114.78	1227	Burnstick
FMH	51.42	115.07	1902	Mockingbird Hill
FGH	51.32	114.94	1433	Ghost

TABLE 2.5   Alberta synoptic surface sites.

Station ID	Latitude	Longitude	Elevation (m ASL)	Name
CYQF	52.18	113.90	905	Red Deer
CYRM	52.43	114.92	988	Rocky Mountain House
CWBA	51.11	115.34	1397	Banff
CWBP	50.35	111.54	755	Brooks
CWCT	52.04	111.27	793	Coronation (auto)
CWJA	52.53	118.04	1061	Jasper
CWLB	54.46	112.01	568	Lac la Biche (auto)
CWMP	49.30	113.57	1190	Pincher Creek (auto)
CWRM	52.26	114.55	988	Rocky Mountain House (auto)
CWSE	53.33	114.06	766	Stony Plain u/a
CWZG	51.11	115.34	1397	Banff (auto)
CYBW	51.06	114.22	1106	Springbank
CYCT	52.04	111.27	791	Coronation
CYED	53.40	113.28	688	Edmonton (Namao)
CYEG	53.19	113.35	723	Edmonton International
CYET	53.35	116.27	925	Edson
CYLL	53.19	110.04	669	Lloydminster (A)
CYMM	56.39	111.13	369	Fort McMurray
CYOD	54.25	110.17	541	Cold Lake
CYOJ	58.37	117.10	338	High Level
CYPE	56.14	117.26	571	Peace River
CYPY	58.46	111.07	232	Fort Chipewyan
CYQL	49.38	112.48	929	Lethbridge
CYQU	55.11	118.53	669	Grande Prairie
CYXD	53.34	113.31	671	Edmonton Municipal
CYXH	50.01	110.43	717	Medicine Hat
CYYC	51.07	114.01	1084	Calgary International
CYZH	55.18	114.47	581	Slave Lake
CYZU	54.08	115.40	782	Whitecourt
CZDY	53.05	116.48	1393	Coal Valley
CZPC	49.31	114.00	1190	Pincher Creek

TABLE 2.6   British Columbia synoptic surface sites.

Station ID	Latitude	Longitude	Elevation (m ASL)	Name
WAE	50.12	122.95	671	Whistler
WCL	51.15	121.50	1057	Clinton
WIR	48.37	123.75	32	Victoria Marine
WLY	50.23	121.58	258	Lytton
WPU	52.12	124.08	909	Puntzi Mountain
WSW	49.75	114.88	116	Sparwood
WVG	48.42	123.32	70	Victoria
WVK	50.23	119.28	556	Vernon
YCD	49.05	123.87	30	Nanaimo
YCG	49.30	117.63	495	Castlegar
YCP	52.12	119.30	683	Blue River
YDC	49.47	120.52	700	Princeton
YDQ	55.75	120.18	655	Dawson Creek
YHE	49.37	121.48	39	Hope
YJM	54.42	124.25	704	Fort St. James
YKA	50.70	120.45	346	Kamloops
YLW	49.97	119.38	430	Kelowna
YPB	49.25	124.23	2	Comox
YQZ	53.03	122.52	545	Quesnel
YRV	50.97	118.18	443	Revelstoke
YSE	49.78	123.17	52	Squamish
YVR	49.18	123.17	2	Vancouver International Airport
YWL	52.18	122.05	940	Williams Lake
YXC	49.62	115.78	939	Cranbrook
YXJ	56.23	120.73	695	Fort St. John
YXS	53.88	122.67	691	Prince George
YXX	49.03	122.37	58	Abbotsford
YYE	58.83	122.60	382	Fort Nelson
YYF	49.47	119.60	344	Penticton
YYJ	48.65	123.43	19	Victoria International Airport
YZY	55.30	123.13	700	MacKenzie

TABLE 2.7   Saskatchewan synoptic surface sites.

Station ID	Latitude	Longitude	Elevation (m ASL)	Name
WEH	49.45	108.98	1078	East End
WFJ	51.13	106.58	595	Elbow
WFN	57.35	107.13	499	Cree Lake
WKO	49.17	105.97	917	Rockglen
YBE	59.57	108.48	318	Uranium City
YBU	53.33	104.00	374	Nipawin
YLJ	54.13	108.52	483	Meadow Lake
YMJ	50.33	105.55	577	Moose Jaw
YPA	53.22	105.68	428	Prince Alberta
YQW	52.77	108.25	598	North Battleford
YVC	55.15	105.27	379	La Rouge
YVT	55.83	108.43	434	Buffalo Narrows
YXE	52.17	106.68	504	Saskatoon
YYN	50.28	107.58	818	Swift Current

CHAPTER 3.

DATA ANALYSIS METHODS

3.0 INTRODUCTION

In order to describe the evolution of the moisture fields for this case study, two analysis regions were defined. The first region encompassed Alberta and southeastern British Columbia. The main purpose of this analysis region is to delineate the large scale surface moisture fields. The second region which reflects the LIMEX85 study area is used to focus on the mesoscale surface and upper air analysis of the moisture fields, and to link these fields to the observed storms from the radar images.

3.1 THE ALBERTA ANALYSIS REGION

The Alberta analysis region is a large area ranging from 49.00° to 60.00° latitude and from 110.00 to 120.00° longitude. This area will be referred to as the Alberta region. In order to facilitate contouring of the moisture fields on the Alberta grid, synoptic surface stations west of 125° longitude and east of 105° longitude were included in the analysis. These stations from British Columbia and Saskatchewan are listed in Tables 2.6 and 2.7, respectively. Figure 3.1 illustrates the distribution of surface data stations with the borders of Alberta shown.

3.2 THE LIMEX85 ANALYSIS REGION

The LIMEX85 analysis area extends from 50.80° to 52.67° latitude and from 113.58° to 116.45° longitude. This LIMEX85 study region is shown in Figure 3.2.
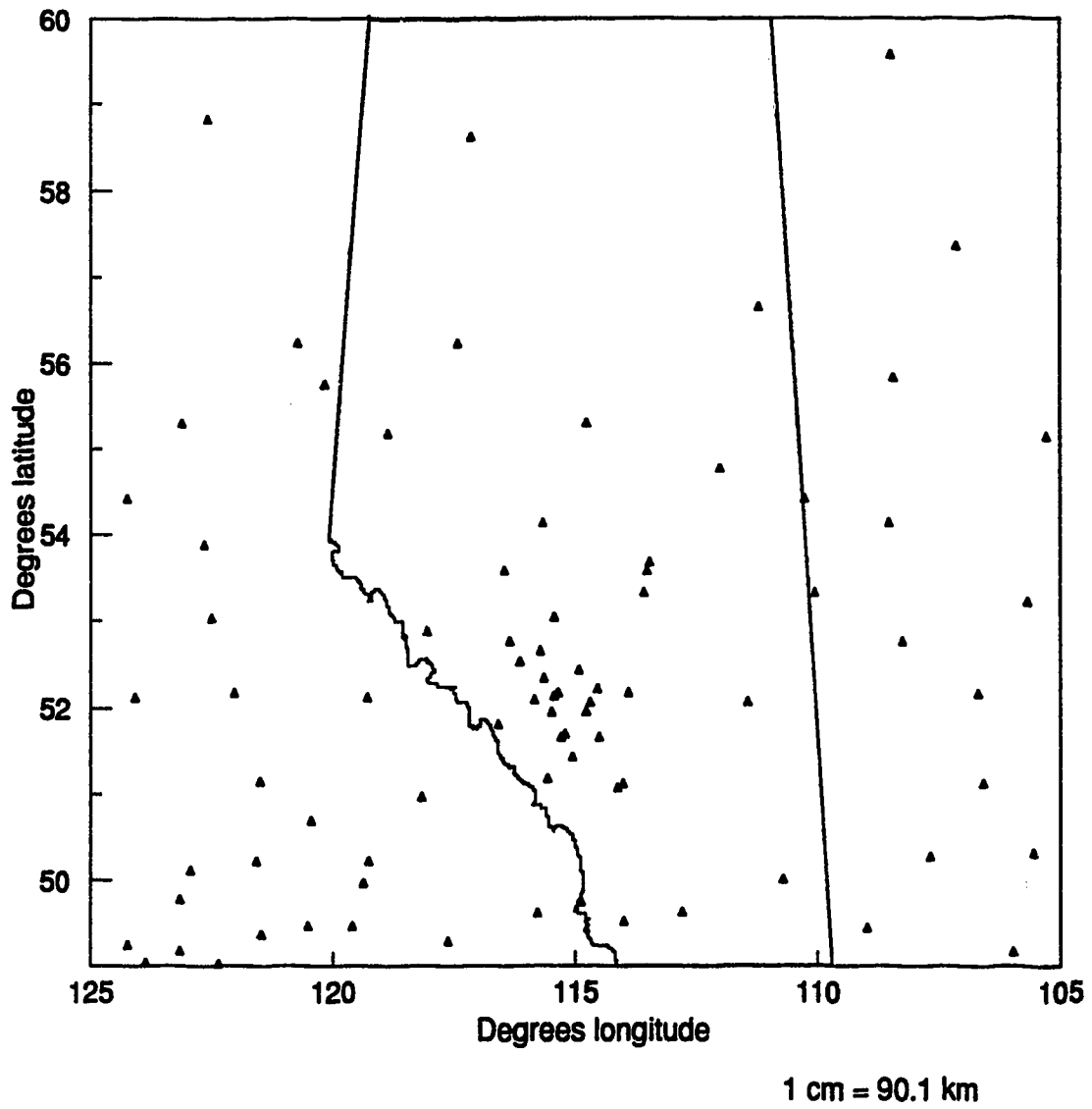
Figure 3.1 Distribution of surface data sites in and around Alberta.

31
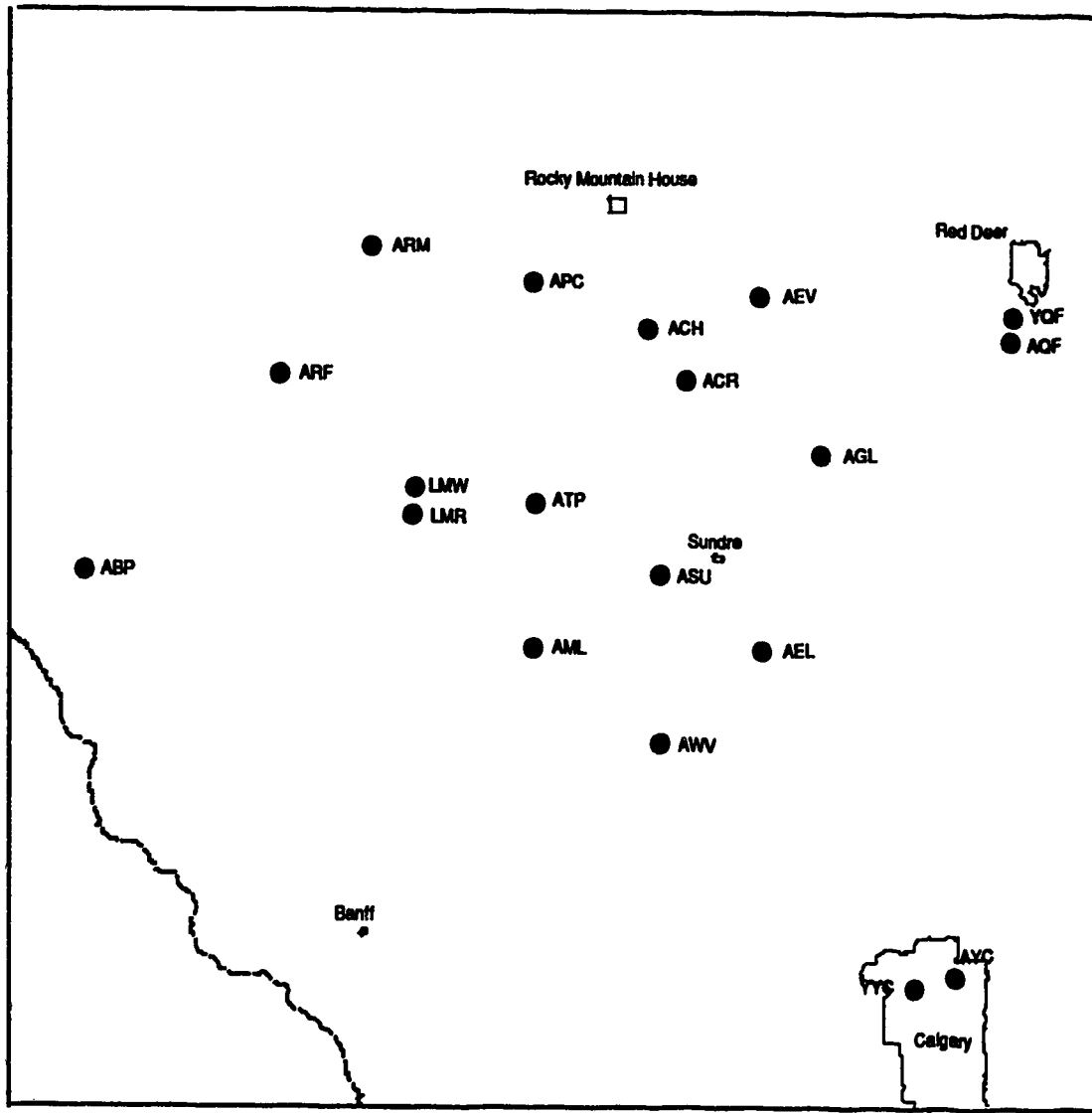
Figure 3.2   LIMEX85 study region.

3.3   PROJECTION, GRIDDING AND CONTOURING

Station location coordinates in degrees latitude and longitude were converted to kilometers about a point of origin at 49° latitude, 120° longitude using a polar stereographic projection. The map location coordinates (X, Y) corresponding to a given longitude and latitude are given by (Haltiner, 1971):

$$X = \frac{2a \cos \phi \cos \lambda}{1 + \sin \phi} \tag{3.1}$$

$$Y = \frac{2a \cos \phi \cos \lambda}{1 + \sin \phi} \tag{3.2}$$

$$r = r \tag{3.3}$$

where:
- λ and ϕ refer to the longitude and latitude of the point of origin,
- r is the distance from the center of the Earth and,
- a = mean earth radius (6367.650 km) (Wenst, 1968).

In order to contour the moisture fields for each region, objective analysis was performed on the irregularly spaced data points to yield moisture content values at regularly spaced intervals across a grid. Contours were then constructed based on the resulting evenly-spaced values. This analysis was performed by the commercially available software package Surfer (1989). The Alberta grid was divided into 8 points in the X direction (east/west) and 14 points in the Y direction (north/south). This translates into a grid spacing of 100 km. This grid spacing was chosen as a value less than the average station spacing. Average station spacing (Δ) was calculated using a formula based on overlapping representative hexagons suggested in Strong (1974):

$$\Delta = 1.075 \sqrt{\frac{area}{\# \, stations}} \tag{3.4}$$

where:
- Δ = average station spacing
- # stations = number of irregularly spaced data points.

33

The area encompassing the Alberta study region is roughly 650 km by 1250 km and the average number of surface stations used was 81. This yields an average station spacing of 108 km. Due to missing data, the number of surface stations ranged from 78 to 84.

The average station spacing of 108 km suggested a reasonable Alberta grid spacing of 100 km. The area in the LIMEX85 region is roughly 200 km by 200 km and the average number of stations used for the surface analysis is 81. The average station spacing for the LIMEX85 region is 22 km. This suggested a surface LIMEX85 grid spacing of 20 km. For the LIMEX85 region upper air analysis, there are only nine stations; therefore, the average station spacing is 67 km suggesting a grid spacing of 50 km to depict the LIMEX85 region upper air analyses.

The LIMEX85 upper air region was divided into a grid of 5 x 5 lines which yields a grid spacing of 50 km. In both the Alberta and the LIMEX85 areas, the regularly spaced grid point moisture values were calculated using a $1/d^2$ weighting scheme using the measurements of the irregularly spaced stations, where d is the distance between station and grid points. The size of the radius of influence was calculated such that the closest ten neighbouring points were used. After selecting the ten stations within the radius of influence, the regularly spaced grid point values were calculated using the formula (Surfer, 1989):

$$Z = \frac{\sum_{i=1}^{10} \frac{Z_i}{(d_i)^2}}{\sum_{i=1}^{10} \frac{1}{(d_i)^2}}$$

(3.5)

where d_i is the distance between the station and the grid point pair and Z_i is the measured value at one of the ten nearest neighbours. The methodology of this gridding procedure reflects the default settings within the surfer software package (Surfer, 1989).

34

3.4   VALIDITY OF GRIDDING AND CONTOURING

The gridding of irregularly spaced data and the subsequent contouring of the surface provides a valuable visualization tool. The resulting contoured maps depict the variation of a variable in space by the use of contours (isolines). The gridding process is one of interpolation/extrapolation from a measured set of irregularly spaced points to a regularly spaced set of grid points. If the input data do not fulfil certain assumptions, the resulting surface may not be representative of the field or meaningful. The assumptions pertaining to the input data include (Harbaugh, Doveton, and Davis, 1977):

- The data fields are single valued at any specific point
- The data fields are continuous everywhere over the map
- The data are autocorrelated over a distance greater than the typical spacing between input data points.

A surface which contains discontinuities will be mapped as one with areas of steep slopes, thereby misrepresenting the surface in the region of the discontinuities.

Sharp (1987) suggests the following two specific rules to ensure construction of a valid contour map from point data:

- Rule 1. The data must exhibit spatial persistence (autocorrelation) out to a radius 1.5 times the average distance between the irregularly spaced data points. This rule expresses the requirement that the data exhibit sufficient continuity such that a reasonable determination of spatial slope and curvature can be obtained from the use of interpolation.

- Rule 2. The contour interval should be selected to be less than twice the probable error of any point.

35

To determine whether the data fulfil the autocorrelation requirement (Rule 1), a covariogram was constructed (Sharp, 1987). Contourable data should have a covariogram which exhibits an appreciable amount of persistence, with the contour interval selected to be twice the value of the probable or calculated error of the input data.

A variety of contoured surface maps depicting four main thermodynamic moisture indices were prepared to delineate the spatial and temporal variations of these parameters in the Alberta and LIMEX85 study regions. A sample covariogram for these four moisture measures is shown in Figure 3.3. The input data sets were from the 1400 UTC time period. The persistence exhibited is beyond the second nearest neighbour (2 grid intervals) indicating valid contouring as long as the contour interval is twice the probable or calculated error (see Section 4.8 Error Analysis). Four additional input data sets were tested. All of these exhibited persistence beyond the two grid intervals chosen.

It should be noted that the autocorrelation in the equivalent potential temperature field may be due to the autocorrelation of temperature and not the moisture field components. Since θe has a larger autocorrelation distance than r it is likely that the autocorrelation of surface temperature is better than that of mixing ratio. However, the fact that the autocorrelation of equivalent potential temperature exhibits persistence beyond two grid intervals (200 km) justifies the use of gridding and contouring depictions of this variable as long as the contour interval is twice the estimated error of the equivalent potential variable (see Section 4.8). The IMC variable is only depicted in the LIMEX85 study region where the mesoscale upper air data is available. Hence the autocorrelation of IMC must exhibit persistence beyond 40 km (2 grid intervals). This condition is satisfied, hence the depiction of IMC values through gridding and contouring procedures is justified as long as the contour interval used is twice the estimated error in IMC (see section 4.8).

The lower autocorrelation values displayed by the integrated moisture convergence parameter in comparison to the other three may be due to the three dimensional column structure of IMC which has a greater degree of variability than the two dimensional structure of the other three moisture measures.
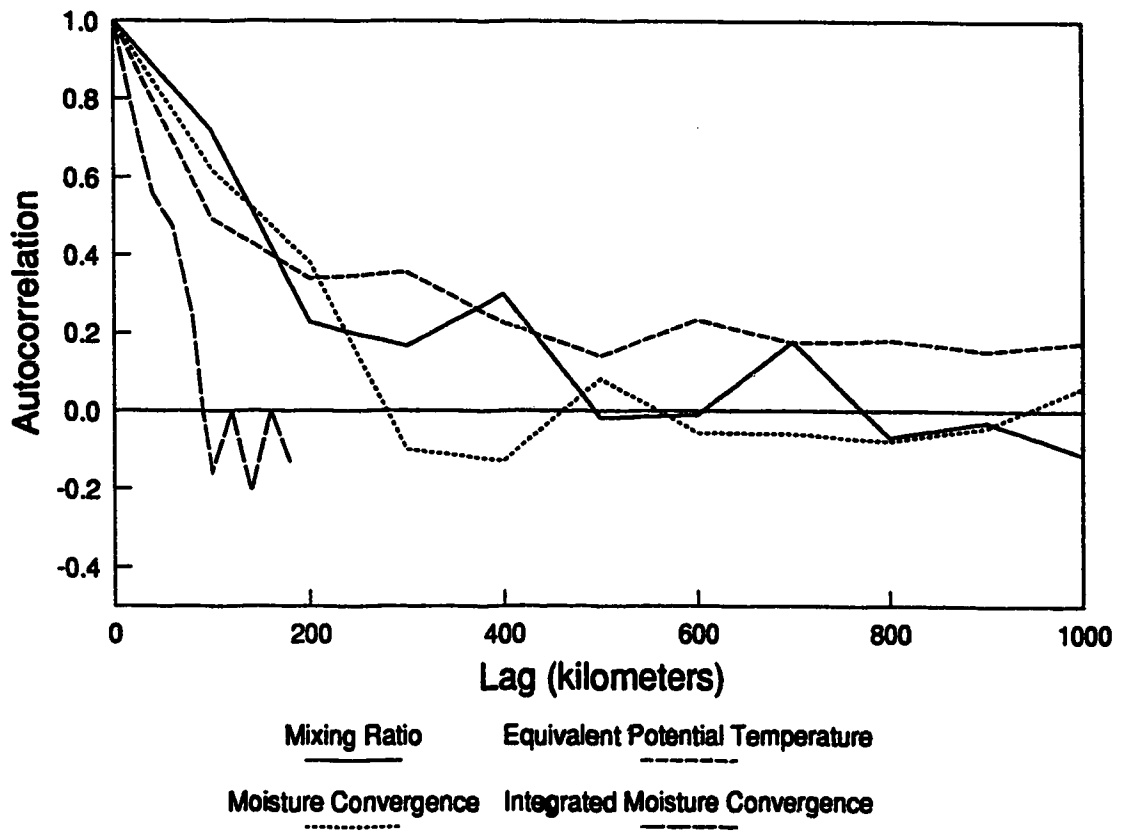
Figure 3.3 Autocorrelation vs lag for the four moisture measures used.

CHAPTER 4.

DATA ANALYSIS

4.1   INTRODUCTION

The following sections will describe and discuss the synoptic maps, radar imagery, vertical soundings and the prepared contoured moisture fields. The synoptic maps provide information concerning the large scale wind fields for the surface and one upper-level (500 mb). Radar images provide the spatial and temporal evidence of storm location and storm track. Vertical soundings indicate the presence or absence of the capping lid and temperature profiles. The contoured plots of moisture variables yield the evolution of the moisture fields in time and space. These fields will be discussed with specific reference made to the radar images in order to link the observed storms to the surrounding moisture fields. In order to assess the range of influence that a small storm (like those which appear in the LIMEX85 study area) with a surface area of 100 km^2 could have on the surrounding boundary layer air mass, the following scenario is presented (Lozowski, 1991: personal communication). For a storm with an area of 100 km^2, and an average updraft velocity of 10 m/s, there is a total of 1 km^3 of air processed per second. In one hour, this translates to a volume of 3600 km^3 of air processed from the boundary layer. If the boundary layer depth is 1 km deep then air from a region 60 by 60 km has been processed in one hour. This is an area 36 times the area of the storm itself and reflects three grid intervals on the LIMEX85 study region. Hence the suggested range of influence should be discernible at this scale of analysis.

4.2   SYNOPTIC SUMMARY

The surface synoptic analysis for 1200 UTC July 11, 1985, (Figure 4.1) shows a high pressure centre of 1025 mb off the west coast of Washington State. A low pressure centre of 1009 mb sits over southwestern Saskatchewan resulting in a northwesterly flow over southern Alberta. The low, with an associated cold front extending southward down through Montana, has been tracking east-southeast at 15 km/h. The mean surface flow in central and southern Alberta is northwesterly. A broad trough extends northwestward from the low into northern British Columbia. A broad ridge of high pressure lies north-south over the eastern prairies. Surface winds over southern Alberta and Saskatchewan were generally light from either the northwest or southeast depending on the stations position relative to the low pressure centre.

The 500 mb synoptic analysis for July 11, 1985 1200 UTC (Figure 4.2) shows a ridge centred just west of the Alberta/Saskatchewan border with winds from the west-southwest. Upper level winds over Alberta were from the west to southwest at 45 to 55 km/h. The 500 mb height contours indicate a region of upper level divergence over central Alberta. Divergence aloft typically infers low-level convergence, which is favourable for storm formation. There is also evidence of weak cold air advection in central Alberta occurring at 500 mb indicated by the crossing of the thickness lines and the height contours. This upper level cooling tends to destabilize the air mass by lowering the temperature lapse rate and increasing the potential instability. The 1800 UTC synoptic surface analysis (Figure 4.3) shows the cold front now situated from the mid-Alberta/Saskatchewan border down through south central Alberta, into south central British Columbia and northern Washington State. The surface winds over southern Alberta are light with the direction ranging from north- northwest to easterly. The low pressure centre (1012 mb) is over the central Saskatchewan/Montana border, having tracked southeast at 40 km/h. A new low has appeared in northern Alberta.

The July 12, 0000 UTC surface synoptic analysis (Figure 4.4) shows the cold front originating near the central Alberta/Saskatchewan border pushing into south central British Columbia. This front has remained essentially stationary since 1800 UTC. The

40

southeastward tracking low (1006 mb) is now in northern North Dakota. The 500 mb synoptic analysis at 0000 UTC (Figure 4.5) shows the ridge having decayed and propagated into eastern Saskatchewan. The winds over Alberta are from the west at 80 km/hr.

Strong (1986) states that storm development in Alberta is often associated with an upper-level trough and a southwest to west flow aloft. The upper trough usually promotes surface strengthening of cyclonic circulation in the lee of the mountains. A surface low center will often appear over southern Alberta. North of this low, regions of upslope flow develop in the surface layer which results in moisture convergence over the Alberta Foothills. These synoptic factors combined with an unstable air mass tend to promote storm formation in Alberta. The synoptic situation for July 11, 1985 reflects the synoptic situation described by Strong (1986) as one favorable for the development of convective storms.

4.3   RADAR SUMMARY

In order to determine the location and time for the convective storms which formed on July 11, 1985, radar images were prepared. These images provided by the Alberta Research Council serve to define the location and timing of observed storms and storm tracks. Since several storms were formed in the Alberta region on this day, the storms will be labelled by capital letters to distinguish between them, and for reference in the following analysis sections.

The Alberta Hail Project S-Band radar data from Penhold, for the LIMEX85 period were processed at the Alberta Research Council facilities in Edmonton during the LIMEX85 experiment. Figures 4.6 to 4.11 show a time series of the processed plan position indicator analyses for July 11, 1985 at the following times:

41
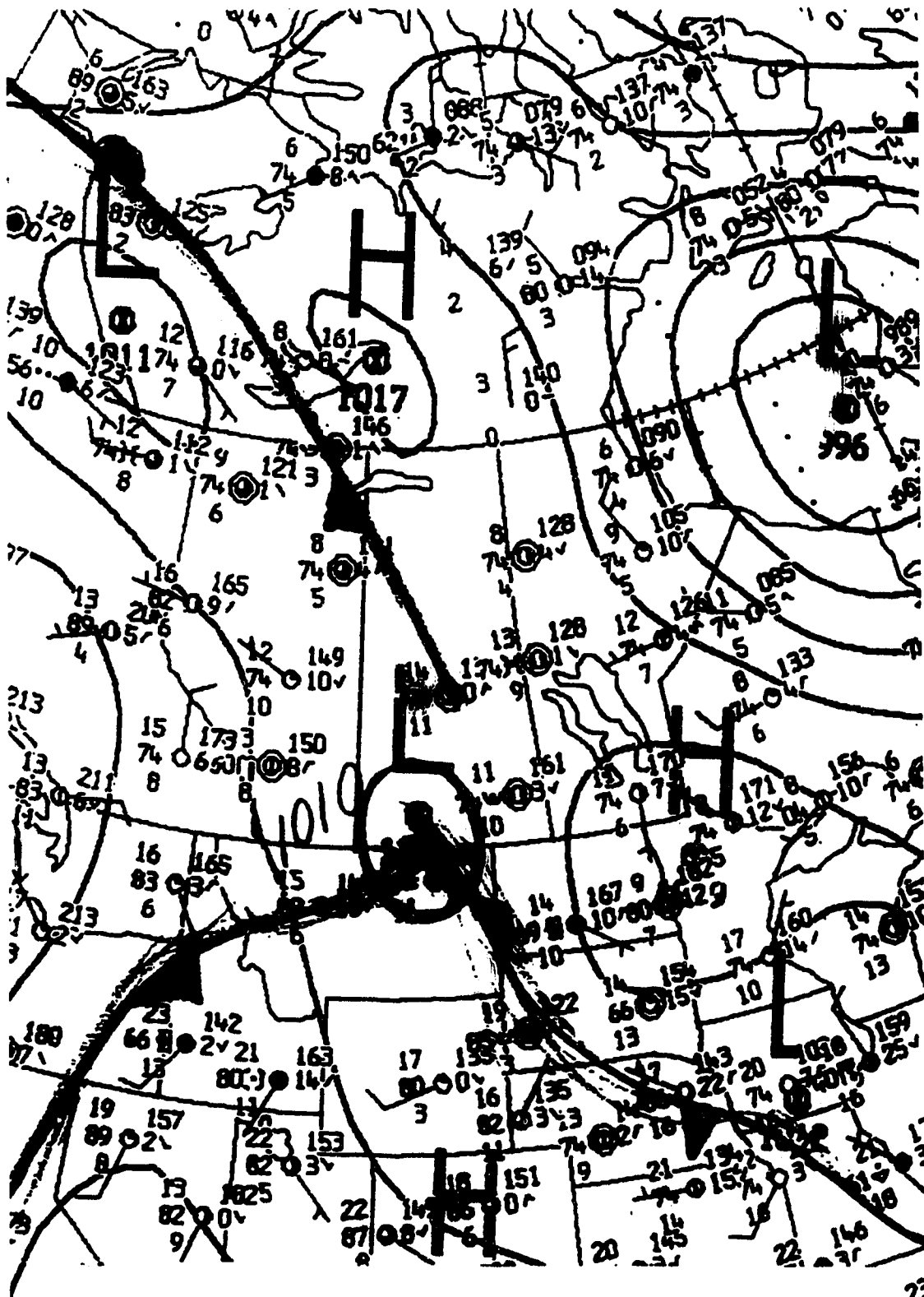
Figure 4.1.   Surface synoptic analysis for July 11, 1985, 1200 UTC.
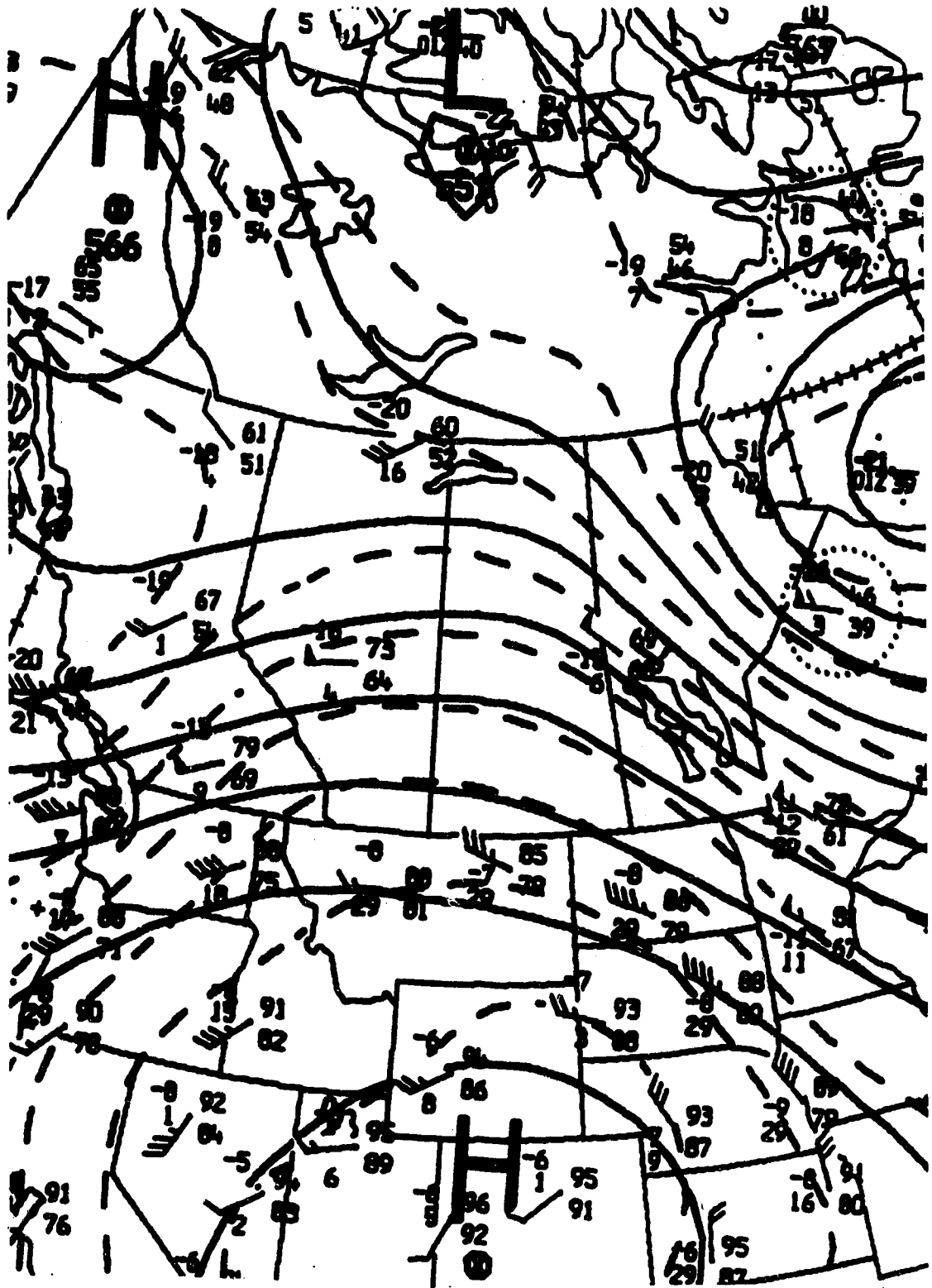
Figure 4.5.   500 mb synoptic analysis for July 12, 1985, 0000 UTC.
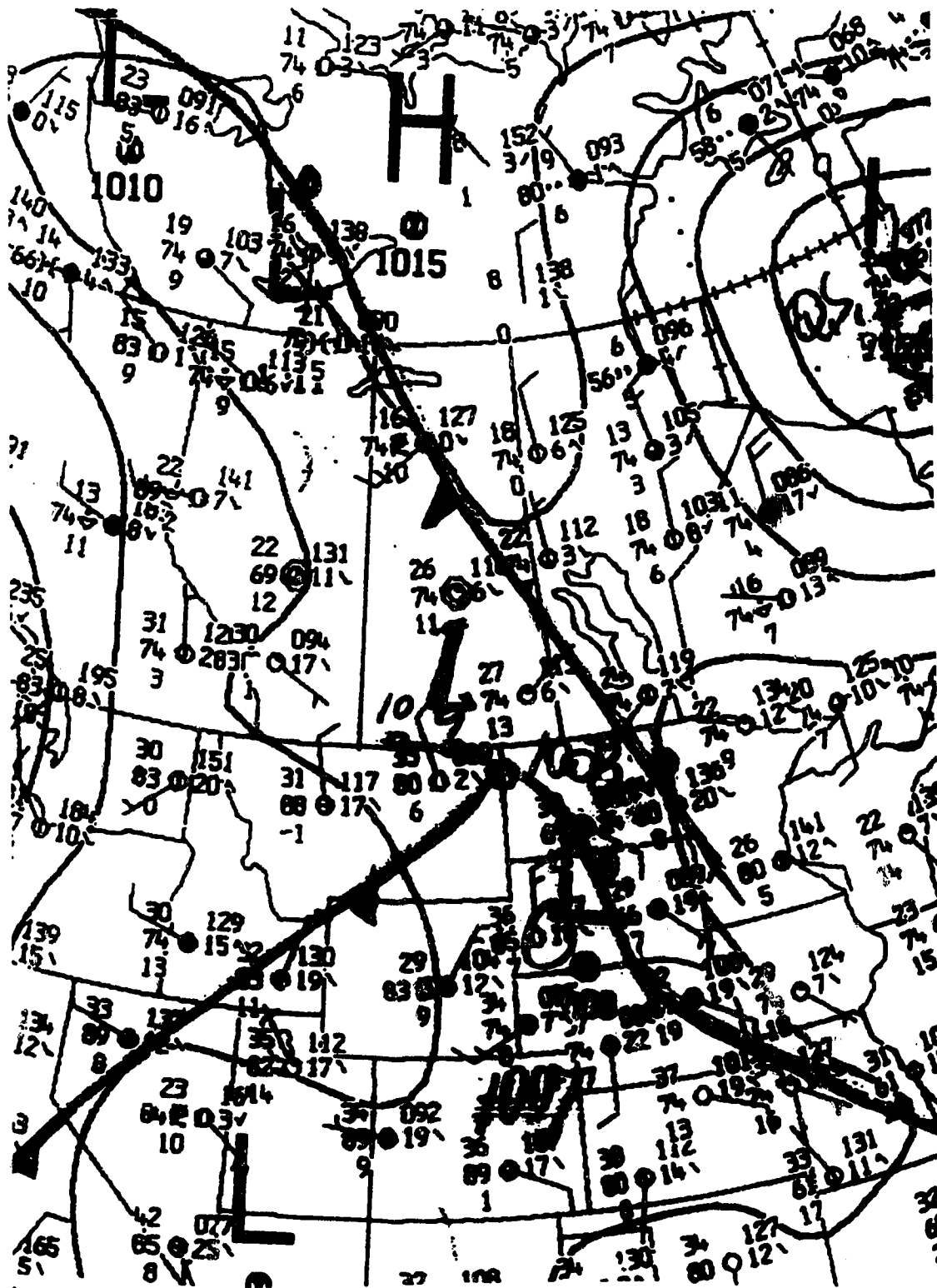
Figure 4.4. Surface synoptic analysis for July 12, 1985, 0000 UTC.
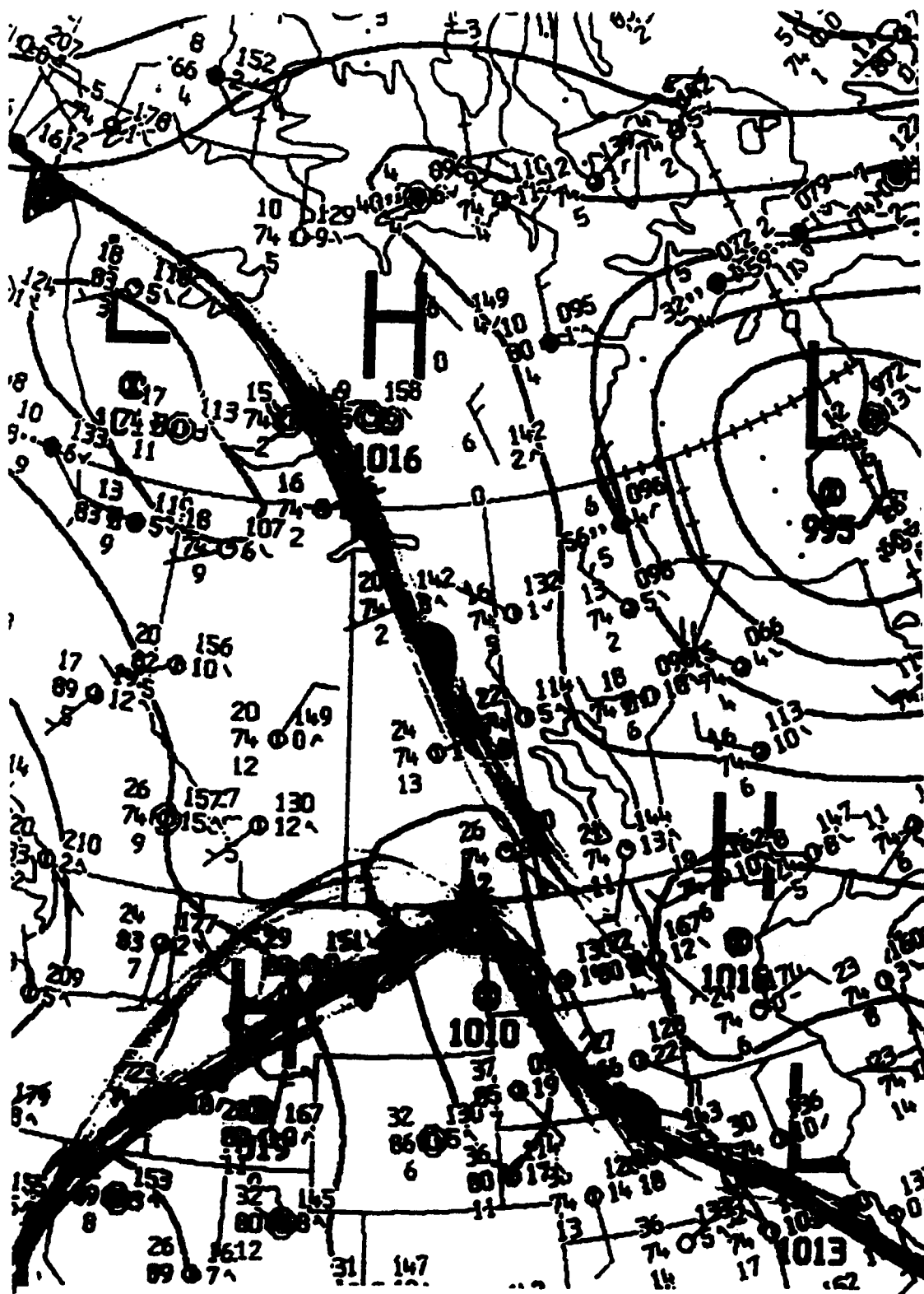
Figure 4.3.   Surface synoptic analysis for July 11, 1985, 1800 UTC.
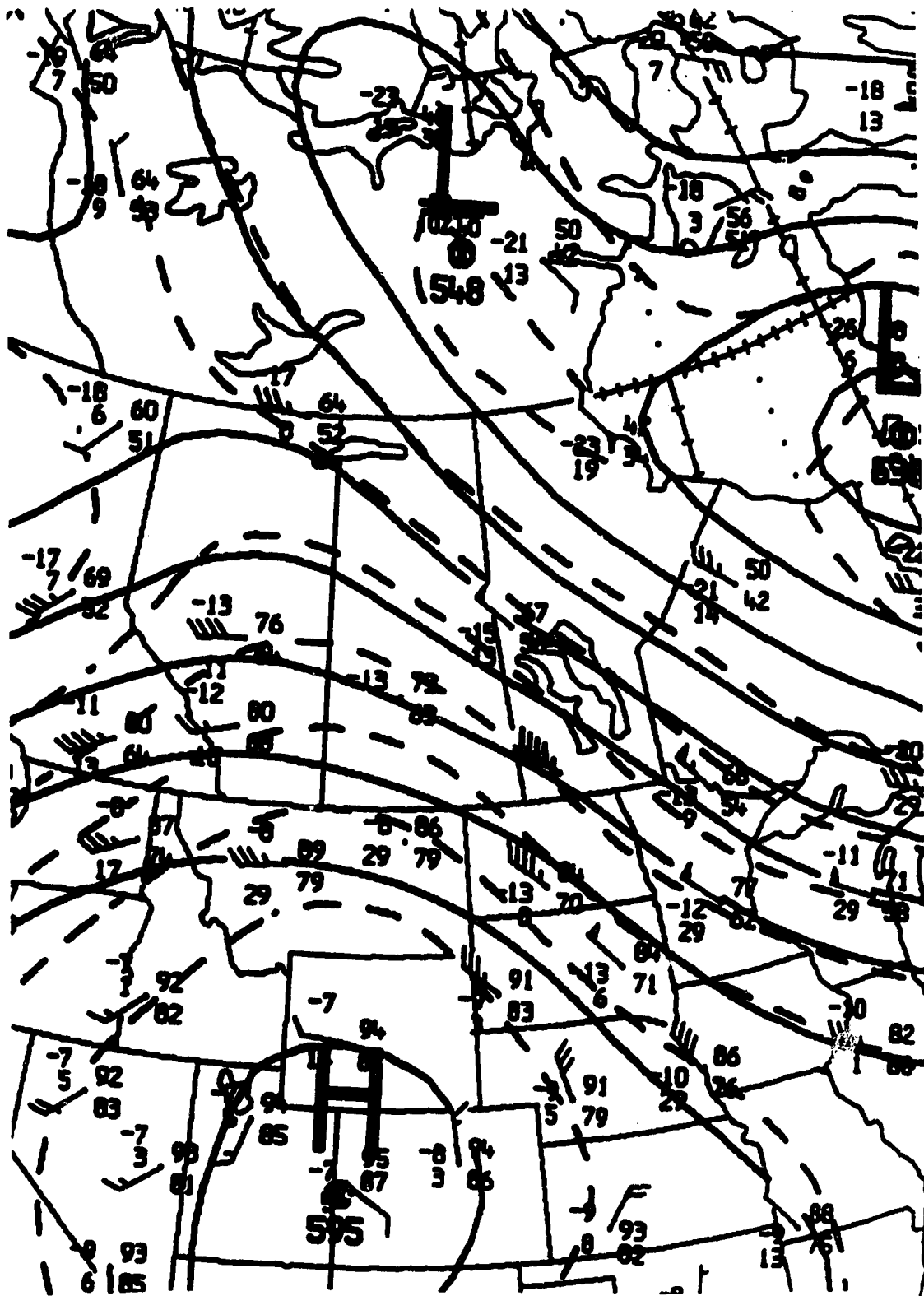
Figure 4.2.   500 mb synoptic analysis for July 11, 1985, 1200 UTC.

- 1800 UTC (Figure 4.6)
- 1900 UTC (Figure 4.7)
- 2000 UTC (Figure 4.8)
- 2100 UTC (Figure 4.9)
- 2200 UTC (Figure 4.10)
- 1700 to 2000 UTC in colour (Figure 4.11)

Figures 4.7 through 4.10 show a circular region extending from Edmonton to south of Calgary and from the Kootenay Plains Natural Area to Coronation in an east-west plane. The range rings are in 22.5 km increments. The contours of reflectivity start at 20 dBZ and go up in steps of 10 dBZ until 70 dBZ. Figure 4.11 is a colour radar image with the range ring increment of 27.5 km and contour colour intervals starting at 15 dBZ in steps of 10 dBZ.

There are a set of consistent dash shaped radar echoes in the southwest region of each figure which tend not to move or change. There are ground clutter echoes from the tops of the mountains. There is also evidence of ground clutter echoes within the inner 20 km core region around the radar facility. In interpreting the radar figures it is useful to relate the observed radar reflectivity values Z expressed in dBZ with expected rain fall rates R (mm/h) and rain water content M (g/m^3). For convective rain situations these variables can be empirically related by the formulas

$$Z = 300 \, R^{1.2} \text{ and } Z = 480 \, M^2.$$

Some benchmark values are listed below:

Z (mm^6/m^3)	316	3162	31623	316228
dBZ	25	35	45	55
R (mm/h)	1	7	49	330
M (g/m^3)	0.8	2.6	8.1	25.7
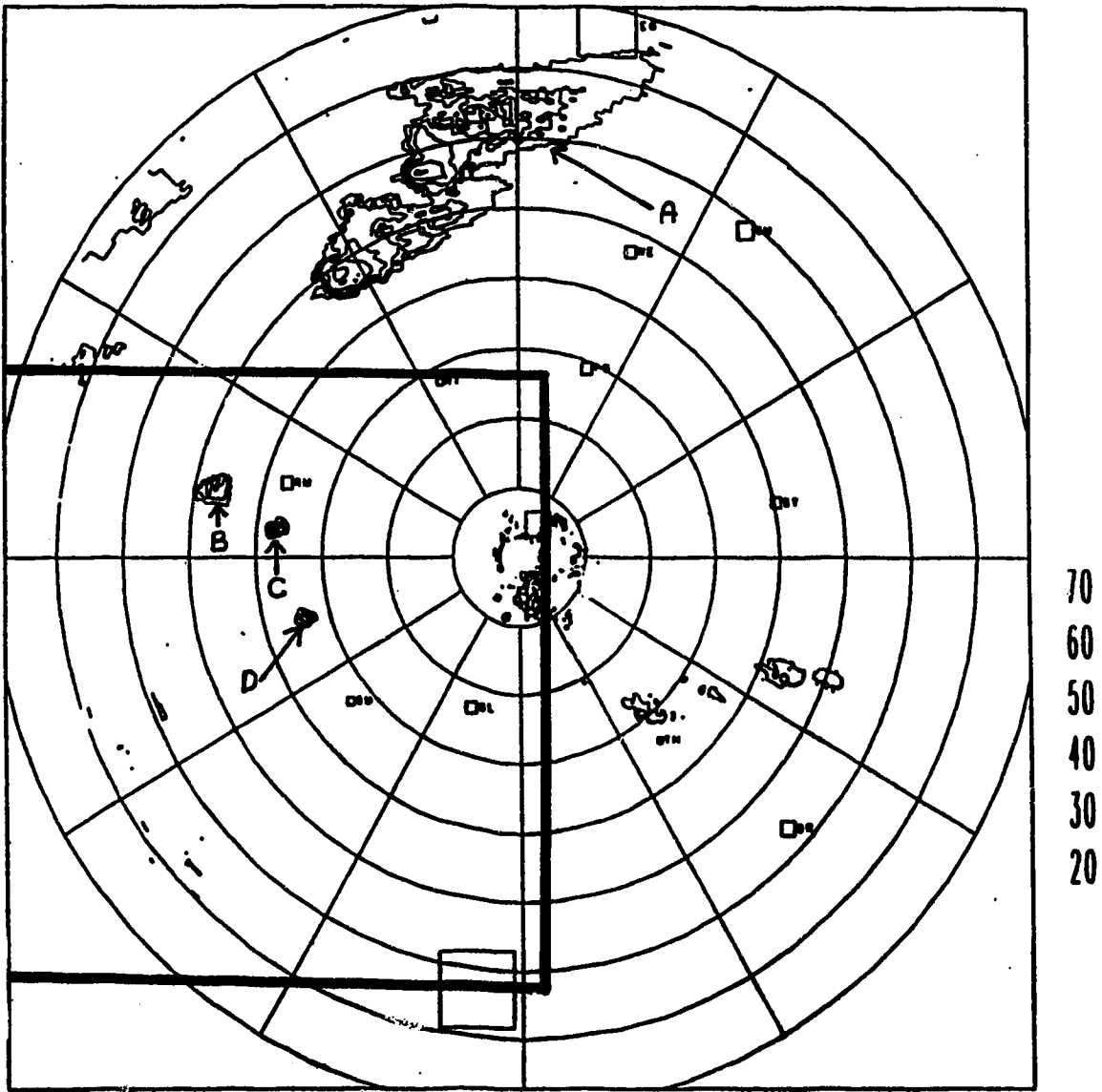
1985-Jul-11 17:59:41.183 1985-Jul-11 17:59:48.000
Reflectivity dBZ PPI MIN 1.3 Deg MAX 2.3 Deg

Figure 4.6   Alberta Hail Project S-band radar plan position indicator imagery
for July 11 1800 UTC.
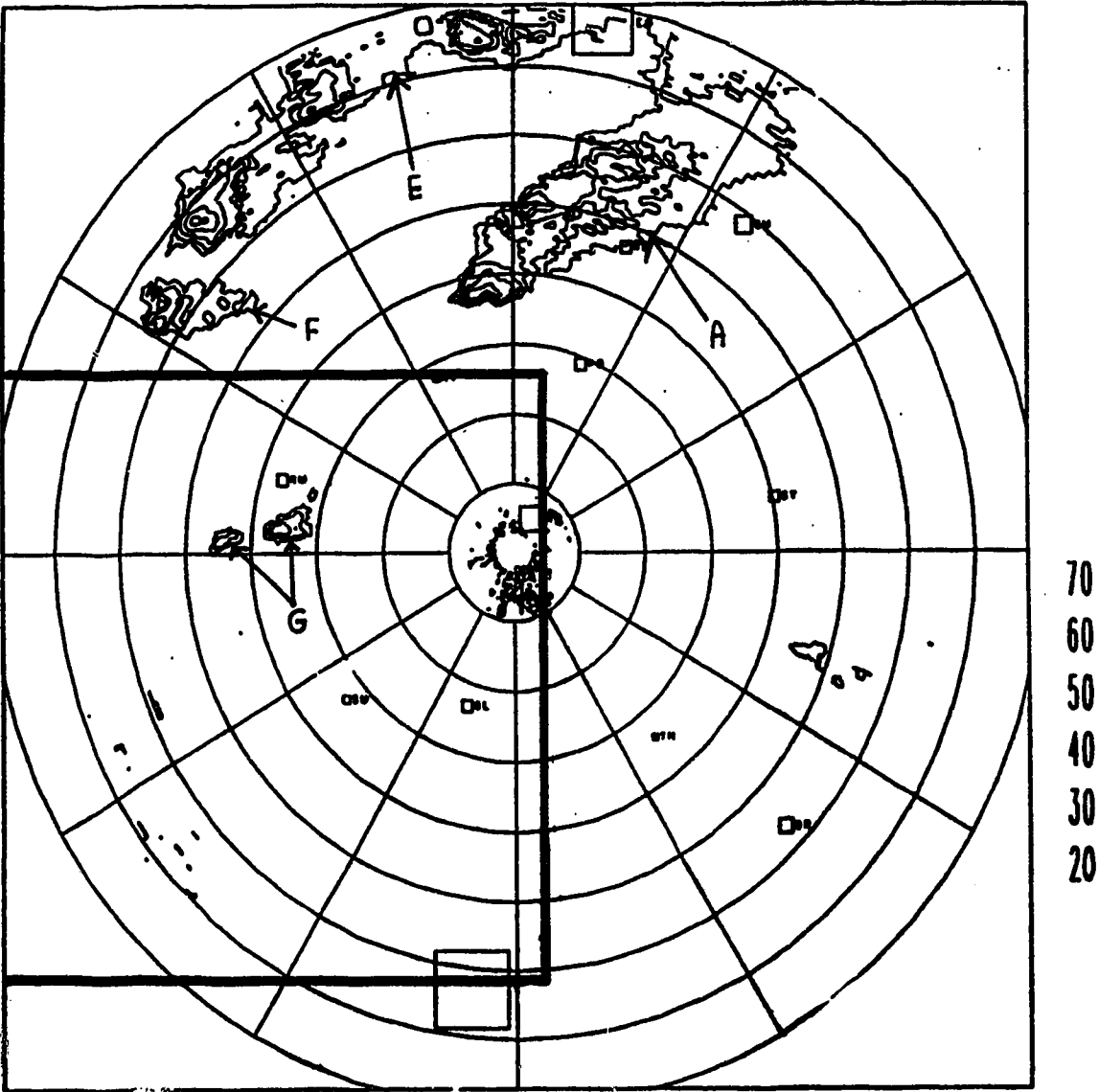
1985-Jul-11 18:59:28.683   1985-Jul-11 18:59:35.500
Reflectivity PPI MIN 1.3 Deg MAX 2.3 Deg

Figure 4.7   Alberta Hail Project S-band radar plan position indicator imagery
for July 11 1900 UTC.
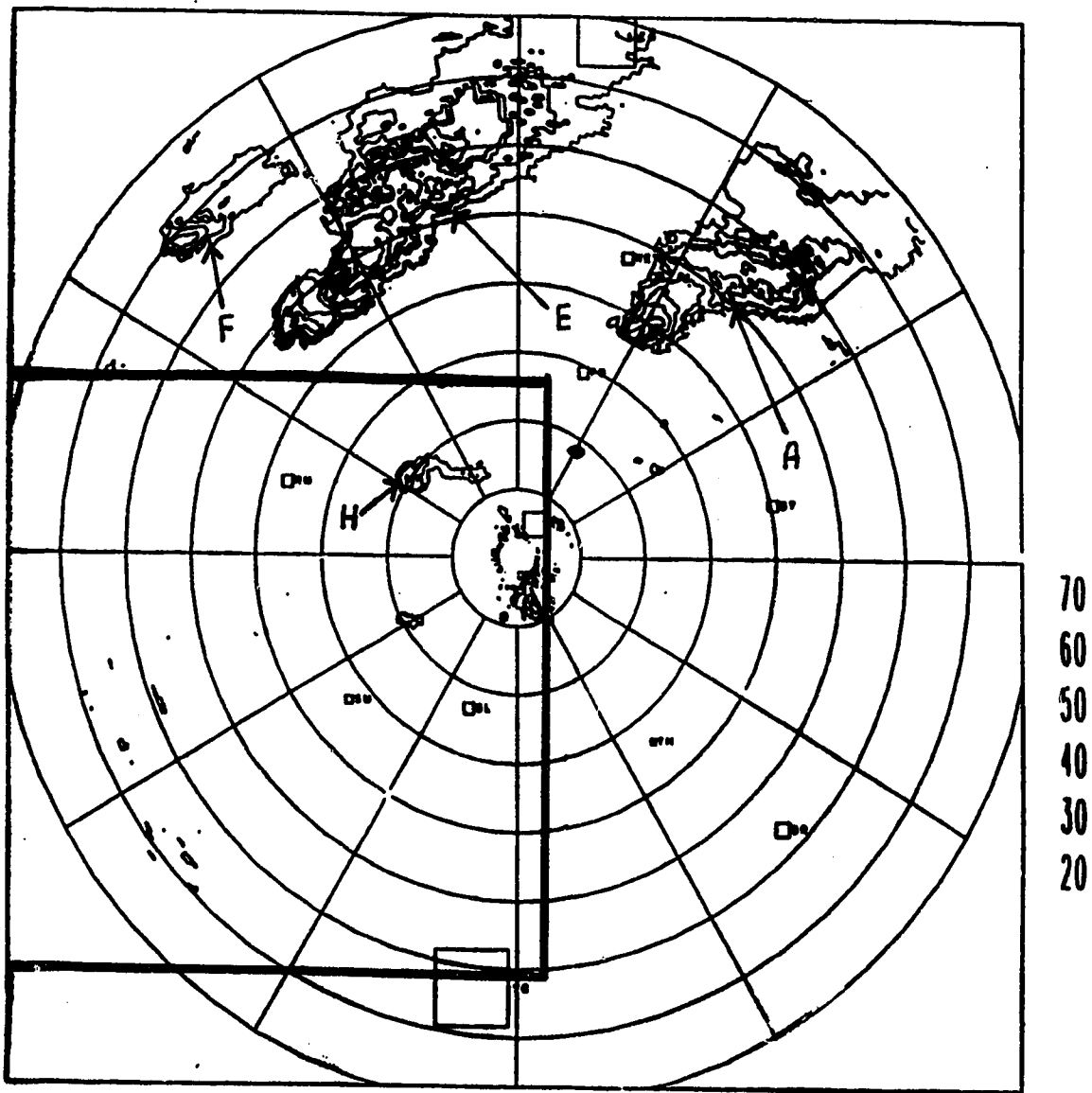
1985-Jul-11 19:59:16.183   1985-Jul-11 19:59:23.000
Reflectivity dBZ PPI MIN 1.3 Deg MAX 2.3 Deg

Figure 4.8   Alberta Hail Project S-band radar plan position indicator imagery
             for July 11 2000 UTC.
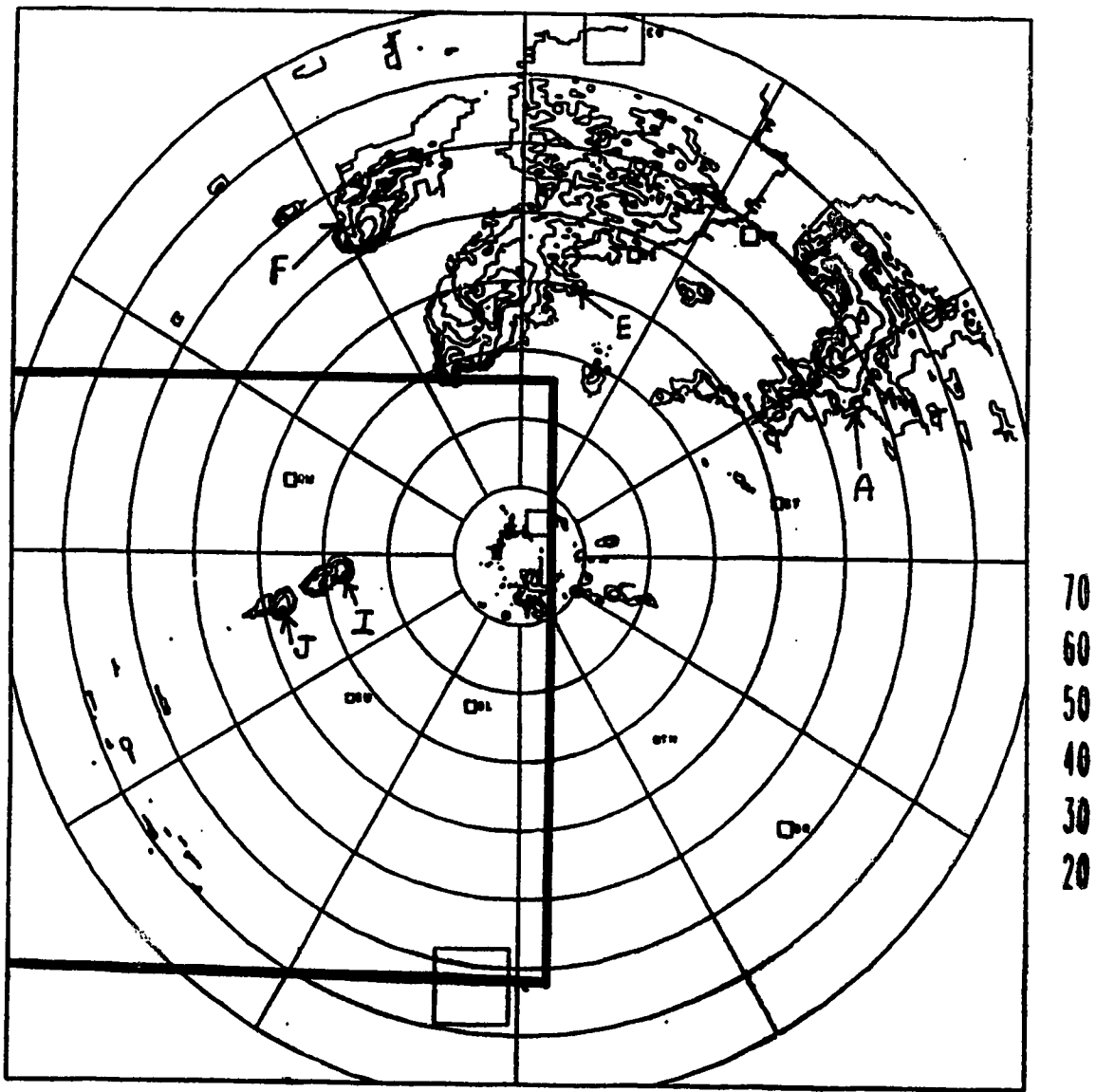
1985-Jul-11 20:59:03.683   1985-Jul-11 20:59:10.500
Reflectivity dBZ PPI MIN 1.3 Deg MAX 2.3 Deg

Figure 4.9   Alberta Hail Project S-band radar plan position indicator imagery
             for July 11 2100 UTC.
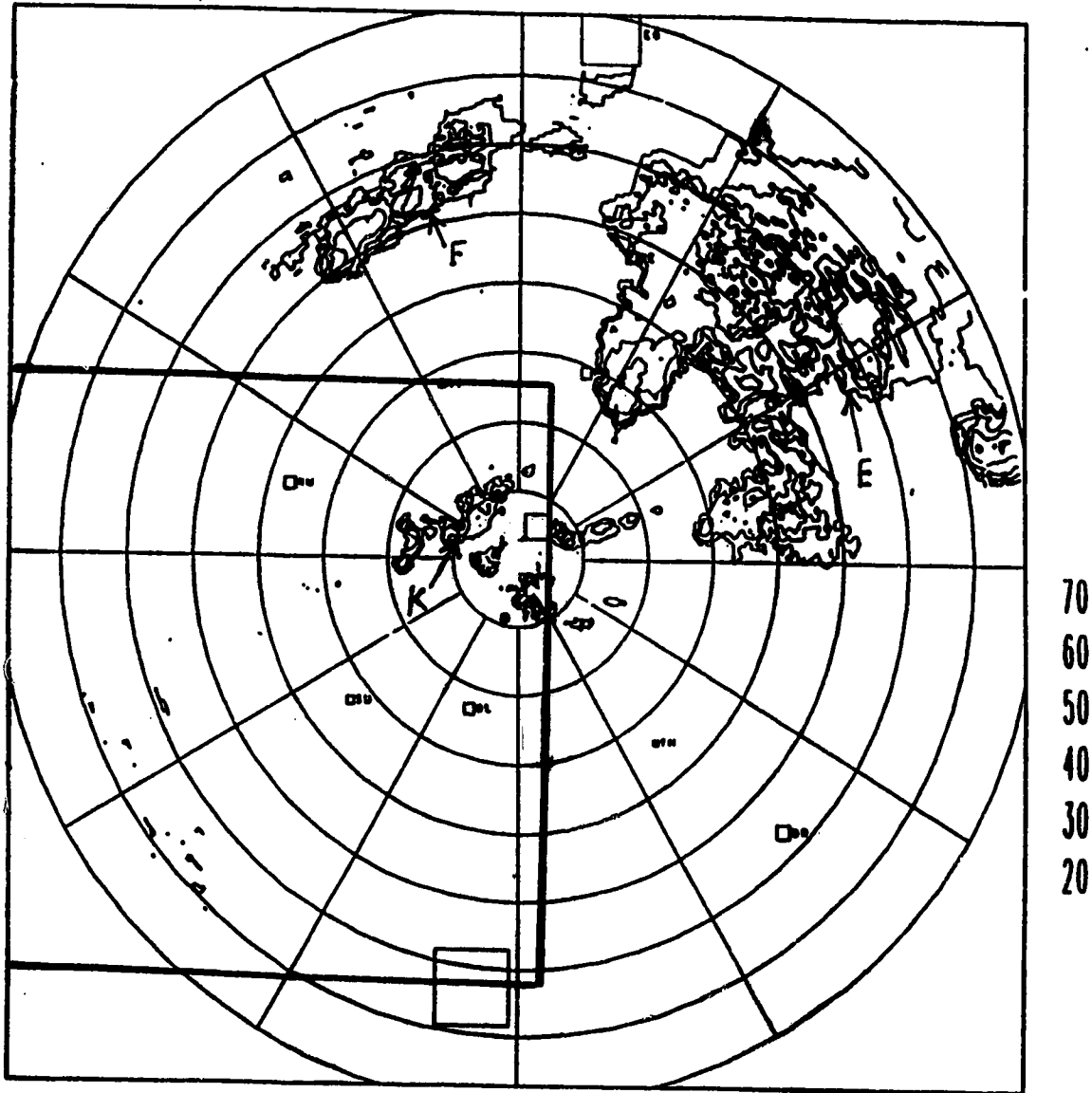
1985-Jul-11 22:00:18.683   1985-Jul-11 22:00:25.500
Reflectivity dBZ PPI MIN 1.3 Deg MAX 2.3 Deg

Figure 4.10   Alberta Hail Project S-band radar plan position indicator imagery
for July 11 2200 UTC.
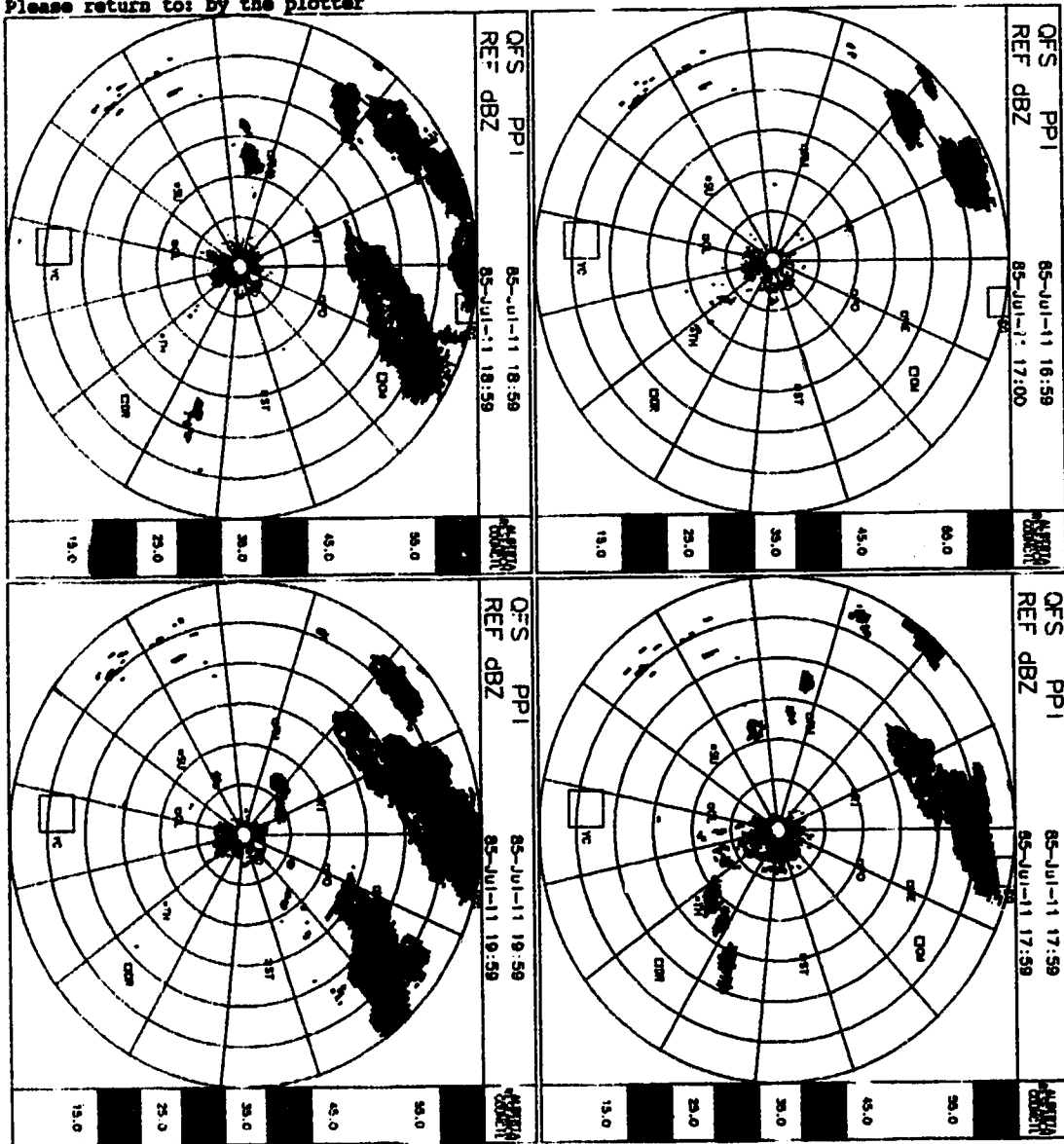
Figure 4.11   Alberta Hail Project S-band radar plan position
indicator colour imagery for July 11 1700 to 2000 UTC.

It should be noted that M measures only the local mass of rain water per unit volume and hence neglects small droplets and the water substance in vapour form. Therefore it is less than the total volume water content.

At 1800 UTC, a large cell exists southwest of Edmonton (Storm A) with maximum reflectivities reaching 60 dBZ. Three small cells (area ≈ 100 km²) (Storms B, C, D) with maximum reflectivities over 30 dBZ are located west and south of Rocky Mountain House within the LIMEX85 study region. The 1900 UTC radar image has several large cells to the south and southwest of Edmonton with maximum reflectivities of 60 dBZ. The large cell southeast of Edmonton is Storm A which has propagated 30 km east since 1800 UTC. Two new large storms west and southwest of Edmonton (Storms E, F) have reflectivities in excess of 50 dBZ. Within the LIMEX85 study region, two small storms (maximum reflectivity 30 dBZ) are located south of Rocky Mountain House. These two storms will be collectively referred to as Storm G. The 2000 UTC radar image shows two large storms (Storms E and F) to the southwest and southeast of Edmonton with maximum reflectivity values over 60 dBZ. Storm A has propagated east roughly 40 km. A small storm (area ≈ 20 km²) within the LIMEX85 region boundary (Storm H) now resides 45 km west of Rocky Mountain House with maximum reflectivities greater than 40 dBZ. At 2100 UTC, the southwest tails of the large cell south of Edmonton (Storm E) has crossed the north LIMEX85 study area boundary with reflectivity values still exceeding 60 dbZ. Two new small storms (areas 100 and 150 km²) have appeared within the study area (Storms I and J) occupy a position 30 km south of Rocky Mountain House with 40 dBZ reflectivities. The last radar image at 2200 UTC shows the large Storm E southeast of Edmonton and Storm F southwest of Edmonton. The LIMEX85 study area has several small cells clustered west of Red Deer with maximum reflectivities of over 40 dBZ. These storms will be collectively referred to as Storm K.

Unfortunately, the largest storms observed by radar are not within the LIMEX85 study area. Hence only surface moisture fields can be linked to these large storms (Storms A, E and F). The smaller storms which are observed to form in the LIMEX85 study area (Storms B, C, D, G, H, I, J and K) are not necessarily separate storms,

however, without a finer time interval, evidence of propagation versus new formation is weak. The moisture fields in the LIMEX85 study area can be depicted at the surface and upper levels. These moisture fields, in the form of contoured depictions, will be discussed with their possible relationship to the observed storm positions being the primary focus.

4.4 TEPHIGRAM SOUNDING ANALYSIS

The two main purposes of the sounding analysis are to look for evidence of the capping lid and to note the height of the lifting condensation level (LCL). The LCL is the level at which a parcel of moist air lifted dry adiabatically from the surface would become saturated, provided mixing in the sub-cloud layer is insignificant.

These objectives are discussed with respect to the stations proximity to an observed storm. Six stations were chosen for sounding analysis. Five out of six stations are within the LIMEX85 study area. A summary of the stations, average surface pressures, and times of the various soundings is provided in Table 4.1. See Table 2.1 for a listing of station names, locations and elevations. See Figure 2.1 for a map of the station locations.

TABLE 4.1   Stations and times of vertical sounding presented.

Station	Times (UTC)				Average Station Surface Pressure (mb)
ACR	1400	1600	1800	2000	893
AYC	1400	1600	1800	2000	888
ARM	1400	1600	1800	2000	903
AQF	1400	1600	1800	2000	911
AML	1400	1600	1800	2000	855
WSE	1200	2400			1010

The choice of these particular stations reflects a desire to contrast the sounding results between stations which showed radar evidence of a nearby storm, and those which did not, as well as the contrast between mountain stations and prairie stations. ARM, ACR, AQF and WSE were chosen as stations near to a passing storm, while AYC and AML did not experience close storm passage based on the radar images. AML was selected as a mountain station and AYC and AQF were used to represent prairie stations.

The main feature or signature found on tephigrams in a region prior to storm formation is evidence of the capping lid. The capping lid, or capping inversion, traps moisture within the boundary layer and temporarily prevents convection and latent heat release (Strong, 1986). Strong suggests that a combination of synoptic and mesoscale ascent and orographic lifting eventually removes or partially removes the inversion, through diabatic cooling, allowing a sudden release of trapped energy which facilitates explosive storm growth. The outbreak of convection is often focussed in a narrow region along the boundary of the capping lid. All heights refer to the distance above ground level. Each sounding has two curves, temperature (the right most curve) and dew point temperature. The LCL is marked with a small arrow. It is important to note

that the cloud base is close to the convective condensation level (CCL) not the LCL. The CCL may be considerably higher than the LCL because of the mixing of moisture in the near-surface layer. The well mixed surface layer grows due to surface heating and this process erodes away the capping lid. After the loss of the capping lid the increasing surface temperatures induce more mixing and reduce the surface water vapour content. This is reflected in the retreating surface dew point temperature.

The only two available soundings for Edmonton Stony Plain (WSE) (Figure 4.12) are from early morning and late afternoon (1200 and 2400 UTC, respectively). The early sounding shows evidence of a shallow inversion layer 1 km (900 mb) deep as well as an upper-level region of saturation at 3 km (675 mb). The late sounding (2400 UTC) shows a well mixed boundary layer and a region of saturation at 5 km (545 mb). The 1200 UTC is about 1.1 km at the 890 mb level. The LCL at 2400 UTC is located at 1.6 km (840 mb).

Tephigrams from ARM (Figure 4.13) show the early pre-storm presence of the capping lid at 1400 and 1600 UTC (0.7 km, 825 mb) as well as its breakdown over time (1800, 2000 UTC). Storms B, C and G occur to the east (25 km) and south (15 km) of ARM at 1800 and 1900 UTC. After this breakdown, the boundary layer moisture is distributed upward, resulting in higher dew point temperature values then previously noted. The breakdown of the lid occurs primarily due to adiabatic cooling from low-level ascent (Strong, 1986). The LCL levels are raised from 0.7 km (830 mb) at 1400 UTC to 1.3 km (760 mb) at 2000 UTC.

The ground-based inversion at AQF (Figure 4.14) develops into a capping lid at 0.7 km (835 mb) by 1600 UTC, which is removed by 1800 UTC. Storm H appears 40 km northwest of AQF at 2000 UTC. The capping lid exhibited by soundings taken at ACR (Figure 4.15) persist until after 1800 UTC (0.8 km, 810 mb). Storm D occurs 20 km southwest of ACR at 1800 UTC. Stations near the regions of storm development (ARM, ACR, AQF) show more defined and longer lasting capping inversions than those far removed from storm development (AYC, AML). This observation concurs with that of Mahrt (1977) where a longer lasting capping lid

57
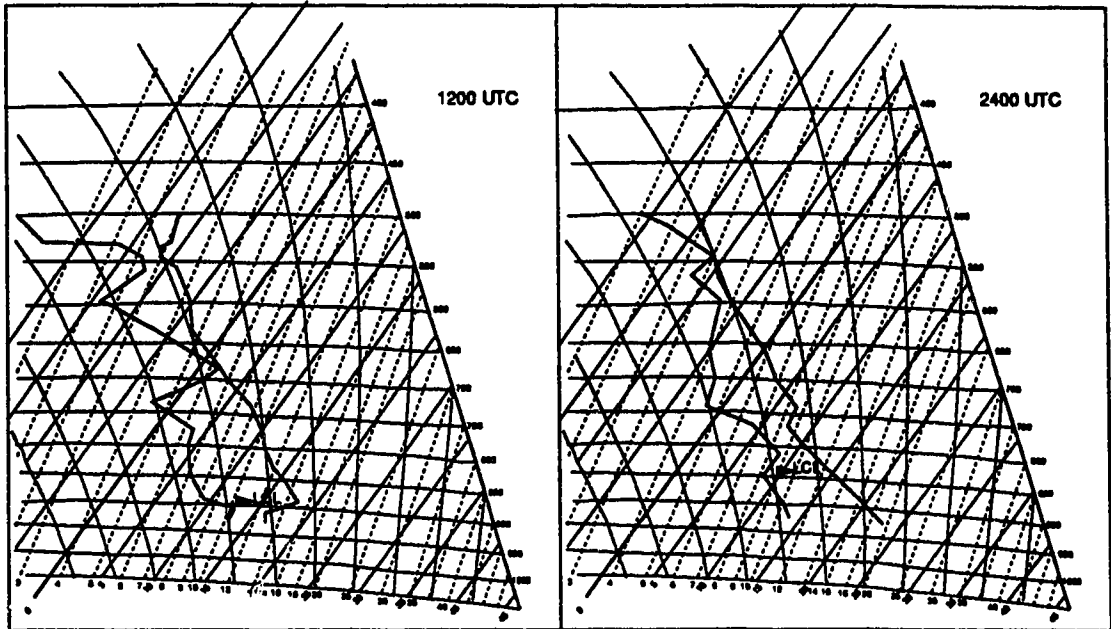
Figure 4.12. Tephigrams for station WSE (Stoney Plain).
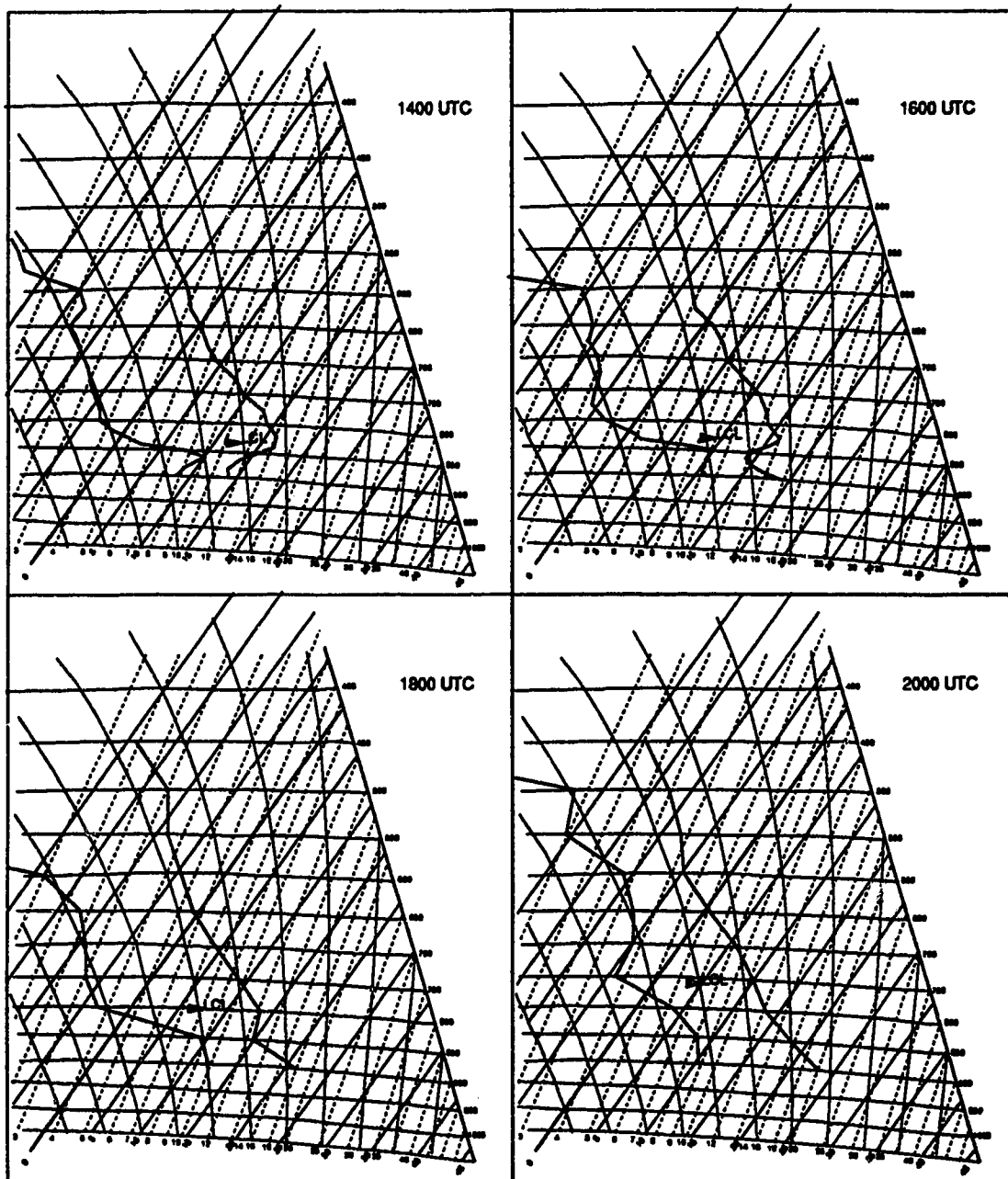
Figure 4.13. Tephigrams for station ARM (Rocky Mountain House).

59
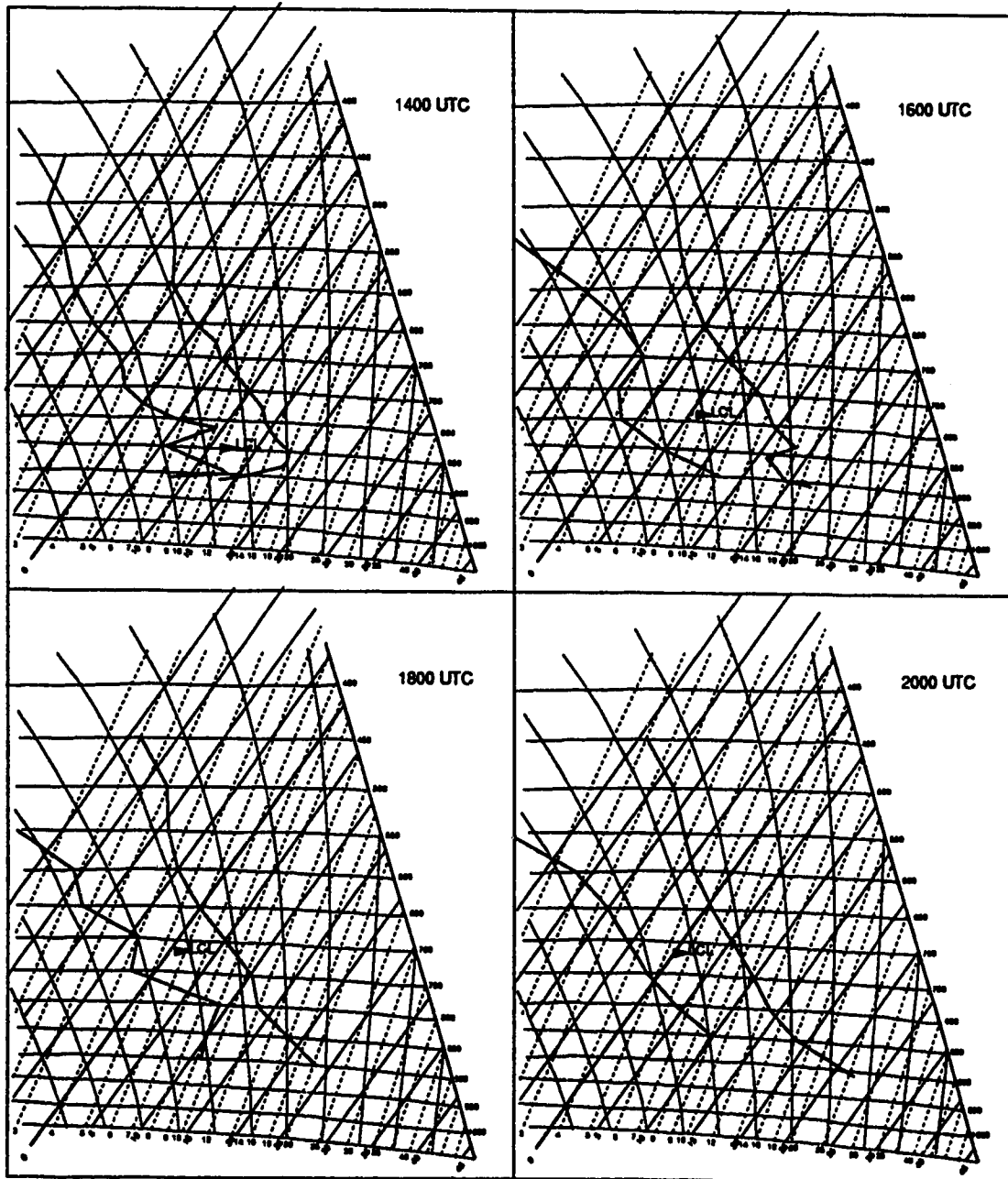
Figure 4.14. Tephigrams for station AQF (Red Deer).
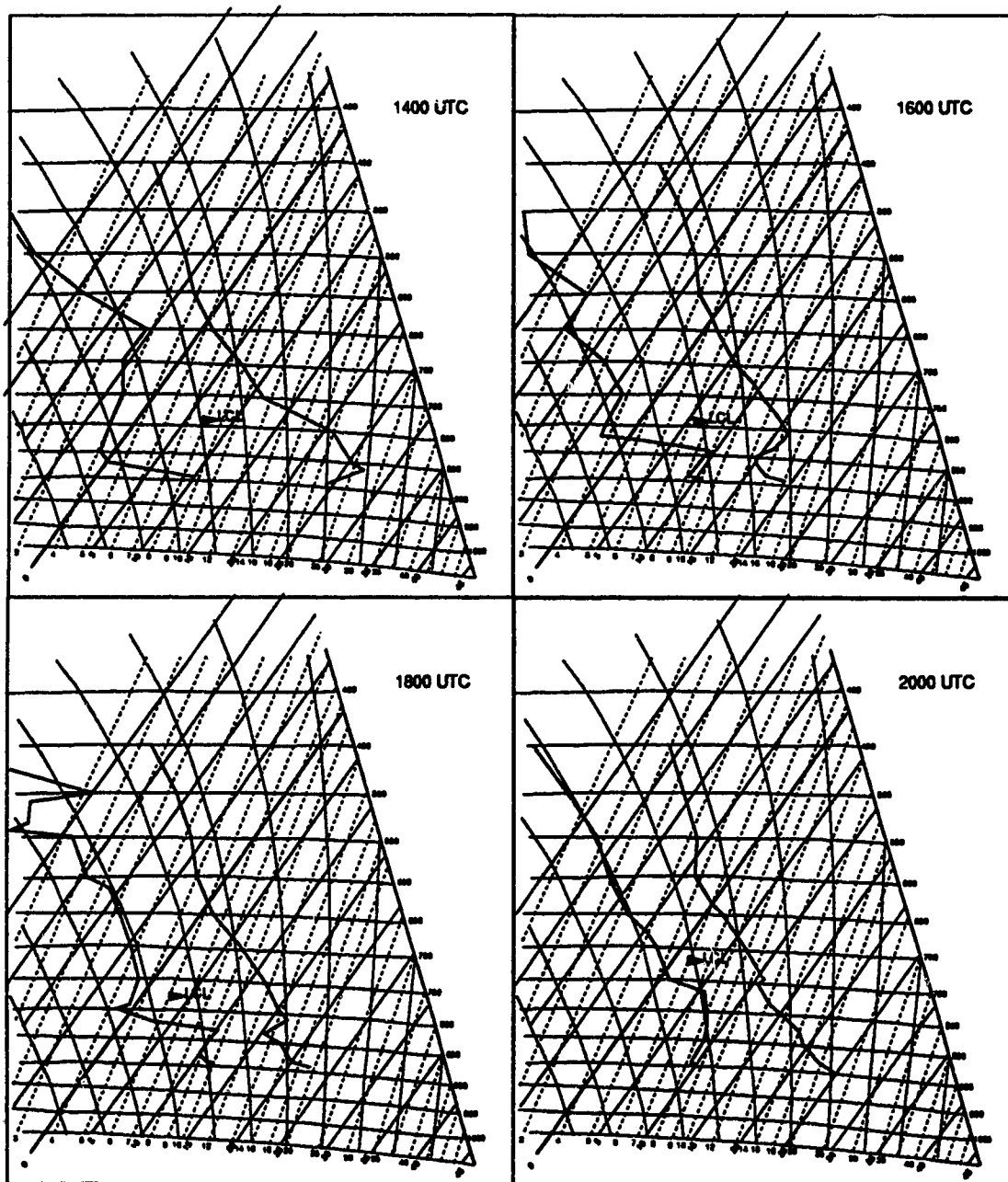
Figure 4.15. Tephigrams for station ACR (Caroline).

61

associated with convective activity is noted. Those stations (ARM, AQF, ACR) near the positions of storm passage as indicated by radar images show cooling as time progresses, and lower LCL's (averaging 0.9 m at 1600 UTC and 12.6 km at 1800 UTC) than stations removed from radar evidence of storm passage. At 2000 UTC the 500 mb difference in the ambient temperature and the adiabatic temperature is roughly 4°C indicating a significant amount of convective available potential energy consistent with the convective activity depicted on the radar images in the Red Deer area at this time.

The early (1400 UTC) ground-based inversion (0.2 km, 870 mb) at AYC (Figure 4.16) and AML (0.4 km, 810 mb, Figure 4.17) has been removed by 1600 UTC with the rest of the soundings showing a deeper boundary layer. These stations are representative of regions where no storm formation was evident on the radar images. They do not show the cooling evident in stations near storm formation. The LCL's average 1.7 km at 1600 UTC and 2.0 m at 1800 UTC. These values are higher than those from stations near storm formation. Lower LCL's often indicates a higher potential for convection. The temperature profiles below the cloud base is roughly dry adiabatic indicating a well mixed boundary layer in terms of temperature. The moisture profiles seem well mixed in the 800 to 650 mb layer but not in the lowest 100 mb layer. This would be due to strong low-level moisture content. The stratification of moisture at 1600 and 1800 UTC may be due to a combination of processes such as the differential advection of moisture, evaporation and rain drops into the air mass or moisture sinks due to the formation of the cumulus clouds.

In order to delineate the wind profile in the areas of storm development, the profiles for stations ARM and AQF are shown below for 1800 UTC.
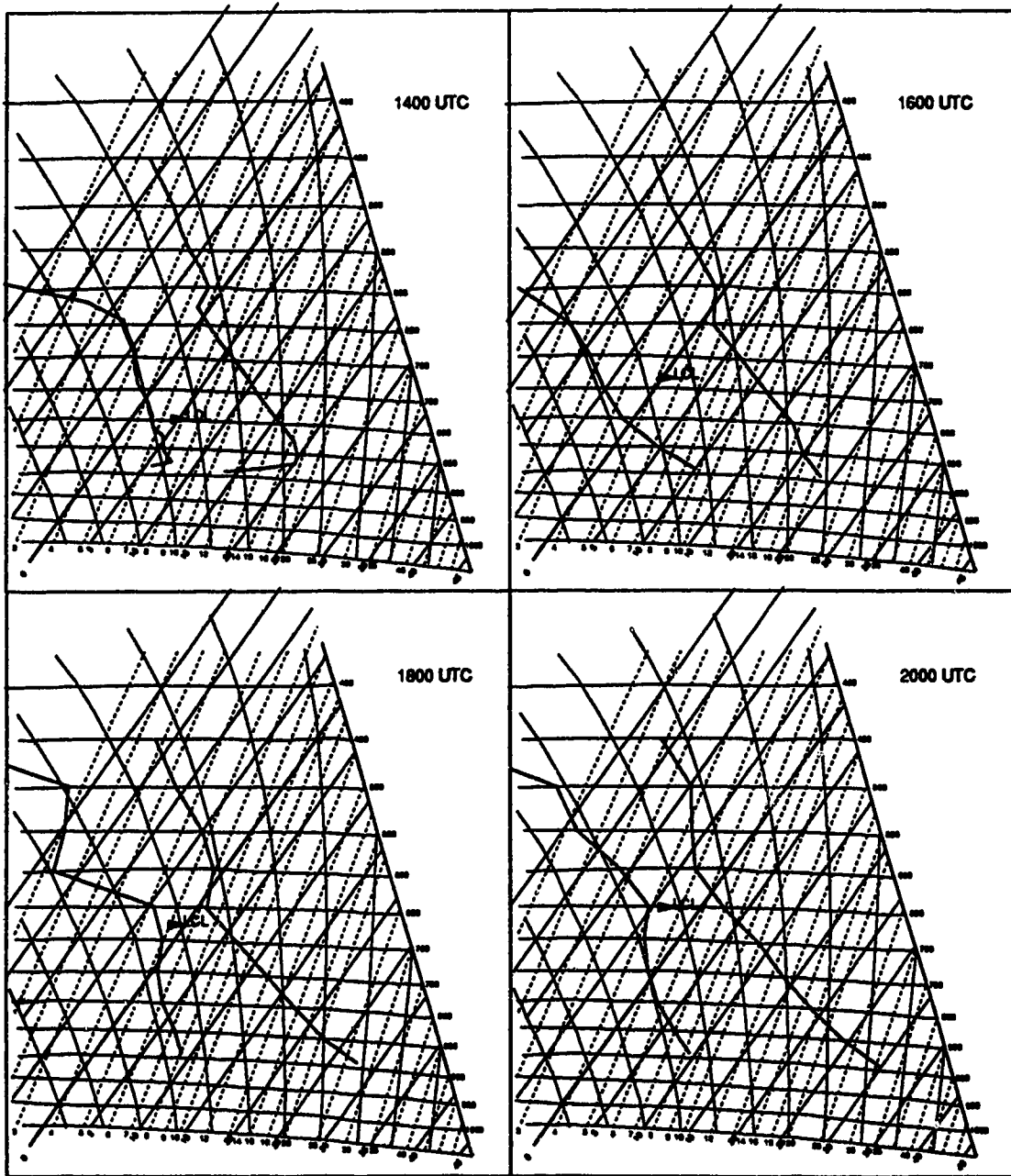
Figure 4.16. Tephigrams for station AYC (Calgary).
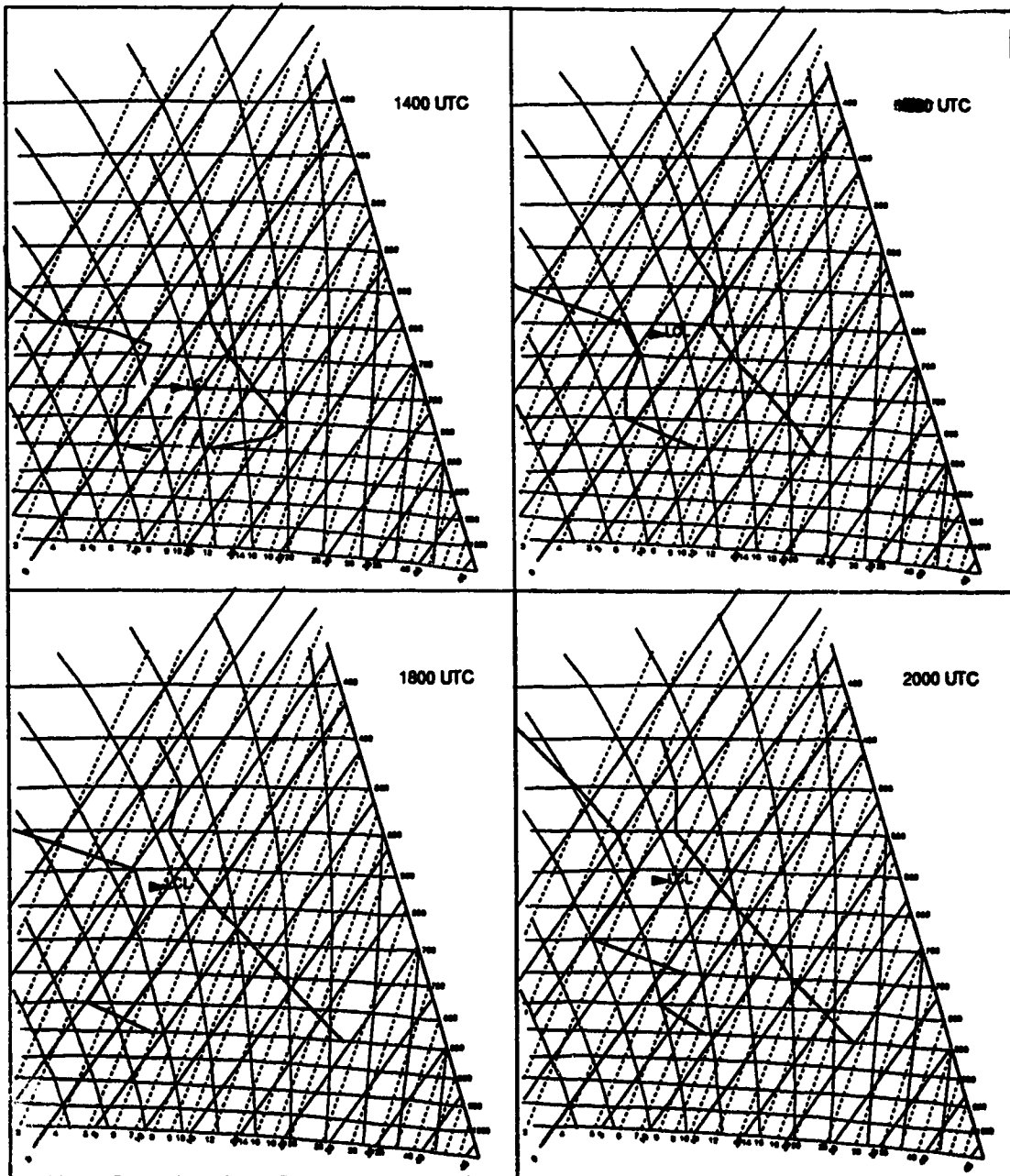
Figure 4.17. Tephigrams for station AML (Mountainaire Lodge).

64

	ARM Wind Direction (degrees)	Wind Speed (m/s)	AQF Wind Direction	Wind Speed
900 mb	330	2.6	330	2.6
850 mb	18	4.2	5	4.7
800 mb	296	3.1	326	3.3
750 mb	244	6.0	342	6.3
700 mb	244	8.7	231	8.5
650 mb	249	11.3	248	9.9
600 mb	258	14.4	251	12.7
550 mb	253	12.7	245	14.7
500 mb	254	19.3	243	18.7

At ARM there is backing between 850 and 750 mb. In the layer between 500 and 750 mb there is only a small variation in wind direction accompanied by wind speed increases from 6.0 to 19.3 m/s. This unidirectional wind is favourable for multi cell storm development. The wind profile from 1600 UTC is similar to that of 1800. The multi cellular storms B, C and G depicted in Figures 4.6 and 4.7 are consistent with the observed wind profiles.

The wind profile from AQF is similar to that of ARM. The multi cellular storm cloud cluster K in Figure 4.10 evolved in a wind profile environment characterized by unidirectional wind shear aloft and moderate changes in wind direction in the lowest layers.

4.5   HORIZONTAL CROSS-SECTIONS IN SPA(

In this section, fields of absolute humidity (represented by mixing ratio, r) and convective potential (as represented by equivalent potential temperature, θe) are contoured and described in order to delineate their evolution in time and to relate them

to the observed storms. Strong (1986) suggests that the analysis of these fields is preferable to the typical forecast operational analysis of dew point temperature (t_d) or dew point depression ($t - t_d$) over Alberta because they are less sensitive to the highly variable elevation changes over the Foothills and mountains. The low-level dynamics are also discussed in this section through the analysis of surface convergence/ divergence of mixing ratio (r). These analysis will be related to convection as observed by the radar images. The connection between the observed storms and the moisture fields will be made by an analysis at two different scales.

The contoured horizontal cross-sections presented in the following sections provide a spatial and temporal characterization of the moisture fields for this case study. The purpose here is to note features in the contoured depictions which concur with previous storm related moisture field observations, and to link these moisture field storm signatures to the observed convective activity. Regions that show no evidence of convective storm activity based on radar images should be associated with a lack of moisture field storm signatures. These moisture field storm signatures which have been delineated by previous researchers are as follows.

In order for a convective storm to form, there must be a source of boundary layer moisture for the storm to draw upon as a moisture source (Braham, 1952). This boundary layer moisture source should show an area of horizontal surface moisture convergence. This surface moisture convergence maximum is often organized to the east and northeast of the observed storm location (Moore, 1982). The convective activity tends to develop in a region which has moisture convergence in a substantial depth of the lower troposphere (Moore, 1982). Park and Sikdar (1982) concluded that for the storms observed in the NSSL mesoscale network, a warm, moist air mass from the southeast converged and the development of localized convection ensued. Maddox (1983) noted that thunderstorms interact with their environments by moistening a deep layer of the troposphere as they pass. Hudson (1971) and Moore (1982) state that evidence of maximal horizontal moisture convergence usually precedes the formation of convective storms by one to six hours, with a typical lag time of three to four hours.

Equivalent potential temperature can be used as a convective storm signature as it is a measure of the convective potential of an air-mass. High values of θe at the surface combined with a potentially unstable gradient of θe in the vertical, form a necessary but not a sufficient condition for the onset of convective storm formation (Strong, 1991: personal communication). Park and Sikdar (1982) found that the pre-storm environment was characterized by a strong decrease of θe in the vertical, with the minimum values occurring near the 500 mb pressure level. Sikdar and Fox (1983) observed their maximum values of θe in a potentially unstable storm environment to be located in the same region as the radar echoes showed evidence of storm formation. They also concluded that during the storms, positive gradients of θe in the vertical were associated with regions of downdraft, while negative gradients occurred in the updraft zone. It is important to note that in order for convective storm formation to occur, a combination of the aforementioned conditions must be met along with the presence of a positive vertical field to transport the boundary layer moisture into the cloud. The work of Honch (1989) which focused on the same LIMEX85 case study concluded that the LIMEX85 study area showed the presence of upward motion fields five hours prior to storm events. He also found that the horizontal surface velocity fields showed convergence aligned along the Foothills of Alberta. Moore (1982) found that the integrated moisture convergence patterns were spatially correlated with radar summaries, with the maximum being closely related to regions of convective storm development.

4.5.1 SURFACE Mixing Ratio Alberta Region (Figure 4.18)

A moisture pool, centered just south of Edmonton at 1400 UTC, intensifies until 2000 UTC when values exceeding 11 g/kg occur south of Edmonton. The centre of this pool moves west to near Lloydminster by 0000 UTC. The tightest gradients are observed at 2000 UTC along with the largest values south of Edmonton. This is the region with significant storm development from 1800 until 2200 UTC (Storms A, E and F) as indicated by radar. This moisture pool satisfies the first condition of storm development (that being a source of surface layer moisture).

67

1400 UTC
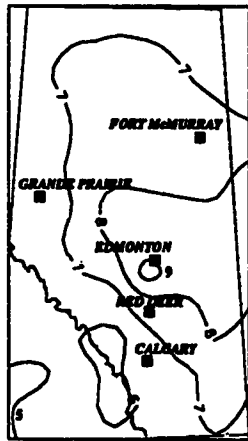
1600 UTC
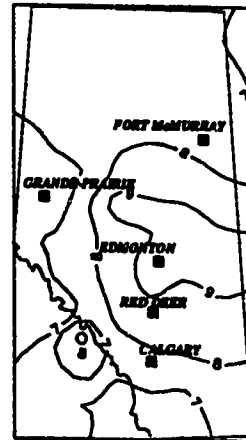
1800 UTC
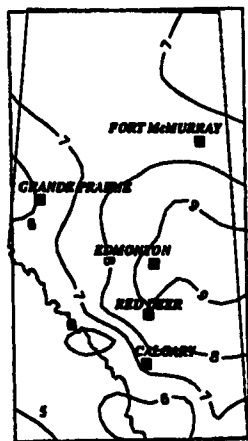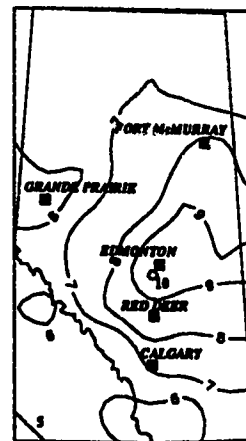
2000 UTC

2200 UTC
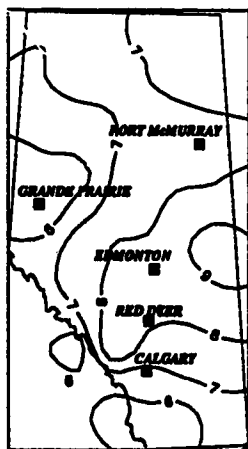
0000 UTC
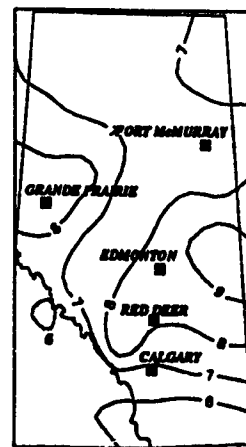
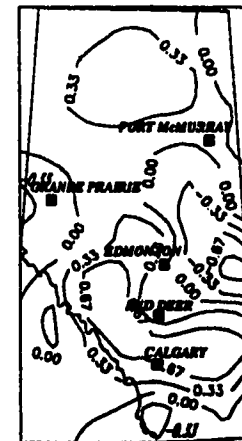Figure 4.18. Contours of surface mixing Ratio r [g/kg] for the indicated times in the Alberta study region July 11 and 12 1985.

Based on the magnitude of the average error in the mixing ratio values (0.25 g/kg) and the consistency of the depicted mixing ratio fields it is reasonable to conclude that the major structural features of the surface mixing ratio have been adequately resolved. The large storms which developed around Edmonton would seem to have their surface moisture requirement meet by the moisture maximum extending from the Saskatchewan boarder to central Alberta.

4.5.2 SURFACE Equivalent Potential Temperature Alberta Region (Figure 4.19)

A warm, moist air mass in south central Alberta at 1400 UTC with maximum values of 318 K strengthens and moves south by 2200 UTC when values of 335 K are observed 125 km southwest of Red Deer. The gradient slowly tightens during the course of the day with the largest values also seen at 2200 UTC. Northern Alberta has the lowest values during the course of the entire period. Sikdar and Fox (1983) state that high values of surface θe should be located in the region at the convective development. In this case, the maximum surface θe values appear south of the region with the largest storms (Storms A, E and F). These storms form in an area with relatively high θe values and tight gradient.

The maximum θe values are observed over the west LIMEX85 region where the small storms (B, C, D, G, H, I and J) formed and propagated. The absence of a θe maximum southwest and south of Edmonton in the regions where the large storms (A, E and F) formed and passed may be due to a lack of station density (Figure 3.1) in this region in comparison to the LIMEX85 region. The equivalent potential temperature reflects the combined influence of temperature and the moisture field which may explain the difference in the spatial variability when compared with the vapour mixing ratio fields shown in the previous section. The local maximum of θe are of particular relevance to storm position as they indicate warm, moist air conditions.

69

1400 UTC
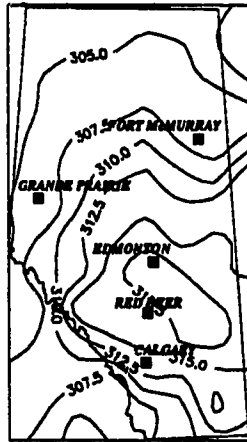
1600 UTC
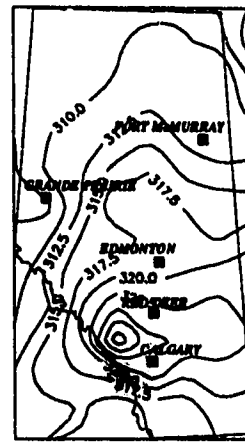
1800 UTC
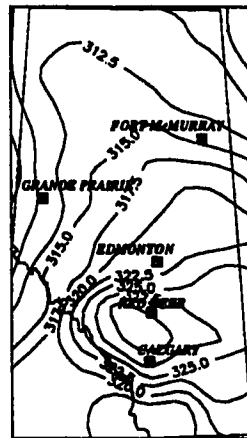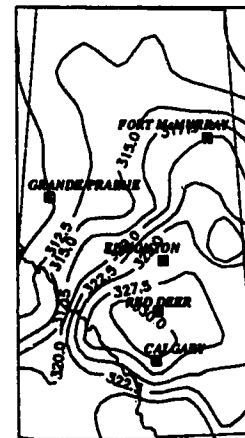
2000 UTC
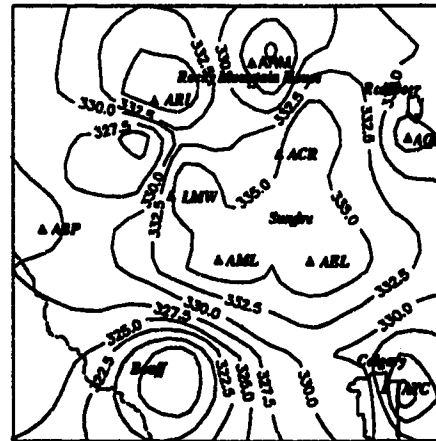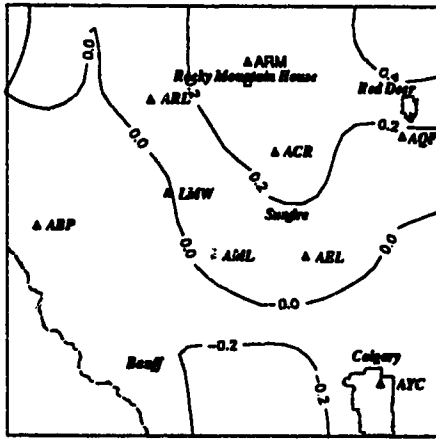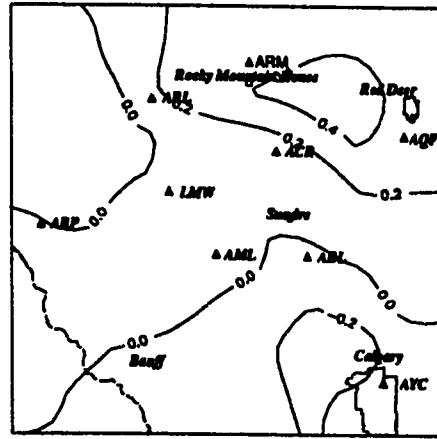
2200 UTC
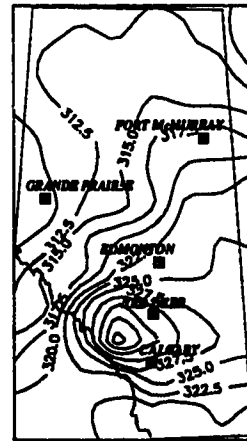
0000 UTC
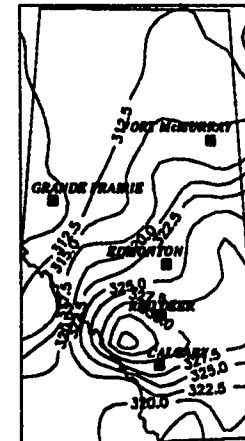
Figure 4.19. Contours of surface equivalent potential temperature θe [degrees K] for the indicated times in the Alberta study region July 11 and 12 1985.

70

4.5.3 SURFACE Moisture Convergence Alberta Region (Figure 4.20)

A region of intense moisture convergence greater than 0.67 (g (kg h)) occurs near Red Deer at 1400 UTC. This coincides with the position of storm E seven hours later at 2100 UTC. Southwestern central Alberta moisture convergence increases to maximum values values of greater than 1 (g (kg h)) near Rocky Mountain House at 2200 UTC. In general, regions west and south of Red Deer show moisture convergence, while regions north and east of Red Deer exhibit moisture divergence. A pocket of moisture convergence 0.67 (g (kg h)) appears in northwestern Alberta at 2200 UTC. The maximum moisture convergence north of Red Deer at 1400 UTC is situated in the region of storm development at 1800 UTC (Storms A, B, C, D). Hudson (1971) states that moisture convergence maximums correlate well with radar echoes one to six hours later.

The maximum at 1600 UTC west of Red Deer also is spatially correlated well with the small storm at 2000 UTC (Storm H). The moisture convergence maximum associated with the large storms which form southwest and south of Edmonton (Storms A, E, and F) occurs between 1400 and 1600 UTC, however, the spatial correlation is weak. This may be due to a lack of data points in that region (see Figure 3.1). Differing grid densities on the Alberta grid and the LIMEX85 grid have the effect of yielding different grid maximas using the same input data set. An example of this can be seen in Figures 4.20 and 4.23 at 1800 UTC. The maximum on the larger scale figure is 1.0 (g (kg h)). The smaller scale figure shows only a 0.6 (g (kg h)) maximum of MC.

4.5.4 SURFACE Mixing Ratio LIMEX85 Region (Figure 4.21)

The surface contours of the LIMEX85 area were gridded at 20 km intervals as suggested by the calculation of average station spacing. The surface contours of the Alberta grid were gridded at 100 km intervals. This is a substantial increase in resolution, hence the resulting contours for the Alberta and LIMEX85 grids do not precisely match, although they do display similar patterns.

1400 UTC
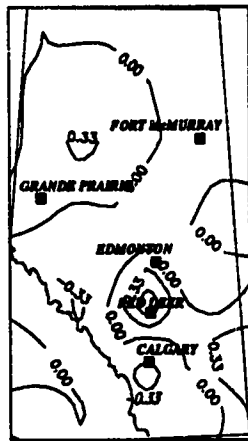
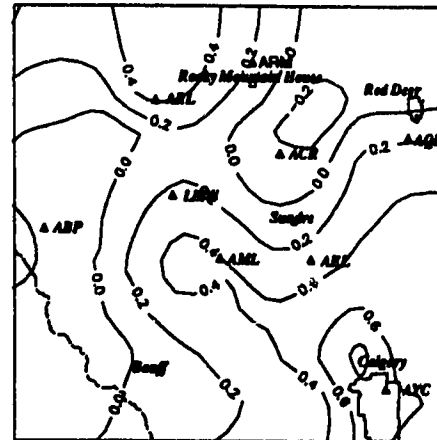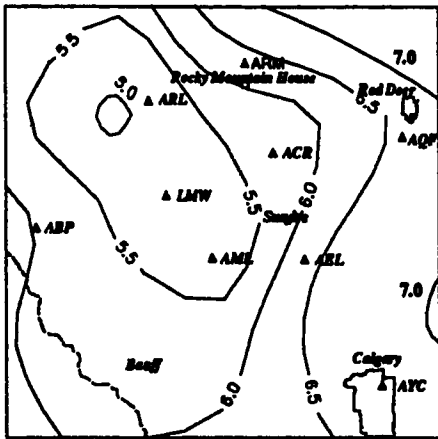**1600 UTC**
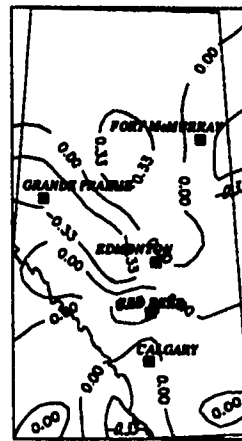
1800 UTC
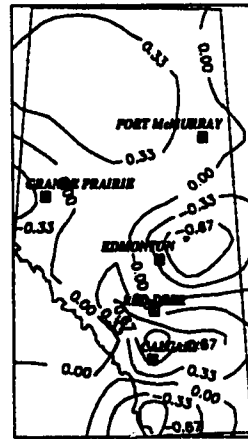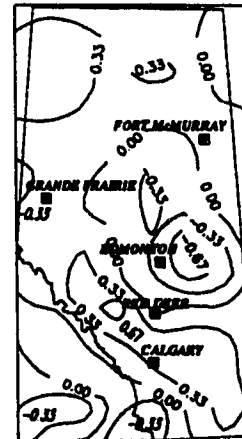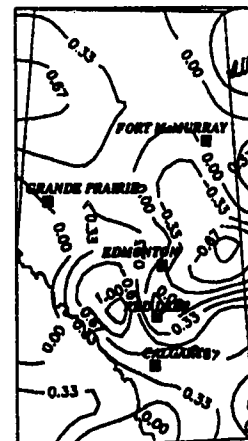
2000 UTC

2200 UTC

0000 UTC

Figure 4.20 Contours of surface moisture convergence MC [g/ kg h] for the indicated times in the Alberta study region July 11 and 12 1985.
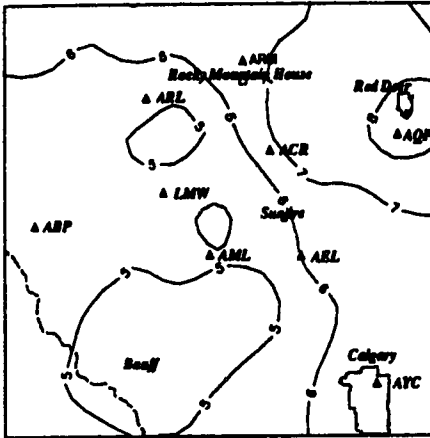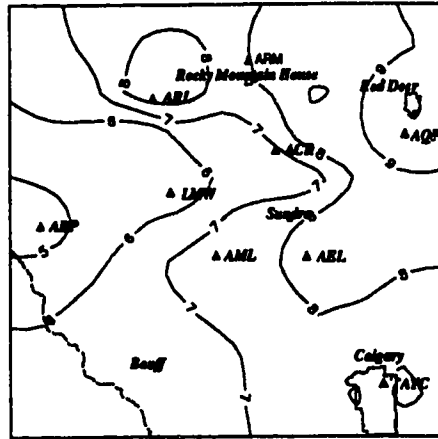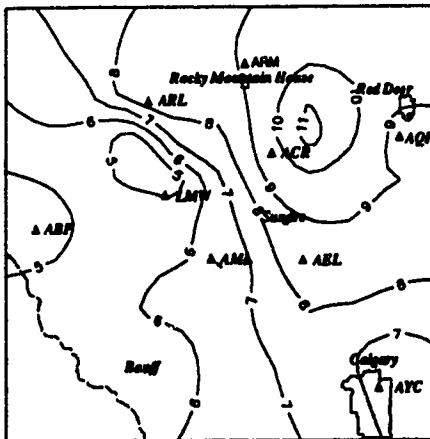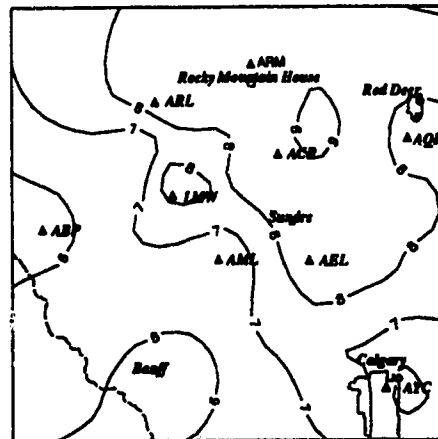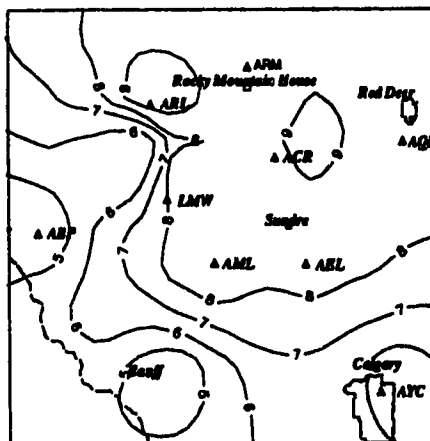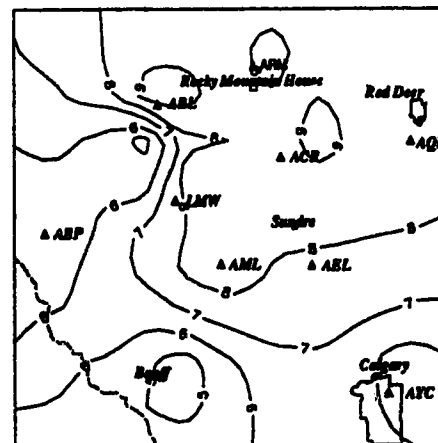
Figure 4.21 Contours of surface mixing ratio r [g/kg] for the indicated times in the LIMEX85 study region July 11 and 12 1985.

A pool of moisture enters the LIMEX85 region from the northeast near Red Deer and reaches maximum values of 11 g/kg near Caroline by 1800 UTC. This pool dominates the northeastern quadrant of the LIMEX85 area until 0000 UTC. The 1800 UTC gradient is the tightest for the entire period. The two small 1800 UTC storms (Storms B and C) occur 75 km west of the moisture maximum position. The storms at 2000 (Storm H) and 2200 UTC (Storm K) occur right in the region of moisture maximum 90 km west of Red Deer. The small pockets of mixing ratio values in excess of 9 g/kg near ARL, ARM and ACR could indicate as boundary layer moistening after the storms in these regions had passed. This type of post-storm moistening was observed by Maddox (1983) in his analysis of ten mesoscale convective complexes. Stations which do not exhibit storm development like AML and AYC typically have mixing ratios of 7 g/kg or less with weak gradients in the regions. The regions with high mixing ratios are generally located in front of the storms possibly indicating that the east edge of the storm is its updraft inflow section.

4.5.5 SURFACE Equivalent Potential Temperature LIMEX85 Region (Figure 4.22)

Two warm moist air masses over ACR and ARM of 320 K at 1400 UTC merge and advect to near ARL by 1600 UTC with values of 330 K. These values indicate a high convective potential and are found in the same region as the storms which develop over the LIMEX85 area from 1900 until 2200 UTC (Storms G, H, I, J and K). During the same time period, a region of cooler θe values predominates in the southwest corner of the LIMEX85 region. This region persists with the lower θe values for all time periods. No convective activity is observed in these regions. From 1800 UTC to 0000 UTC the highest values of θe remain in the ACR, AEL region with the peak value 340 K occurring northeast of Caroline at 1800 UTC. The position of this maximum is very close to the 1900 UTC storm position (Storm G). The tightest θe gradients are observed at 1600 UTC between ACR and AEL. This indicates that there was a discontinuity of convective potential in that region. No storms were observed to form or propagate through regions south of Sundre, where lower values of surface θe persist.

74
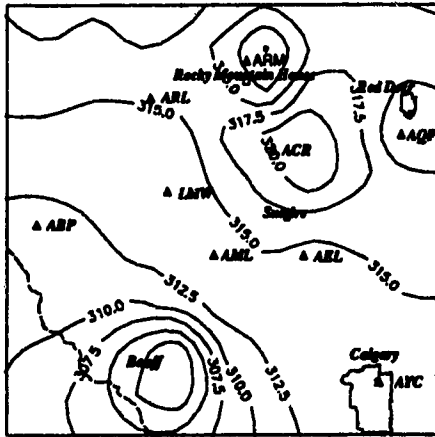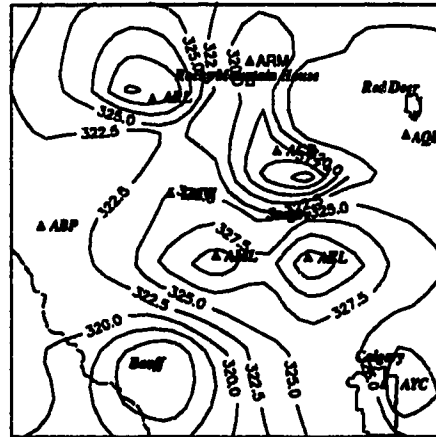
1400 UTC
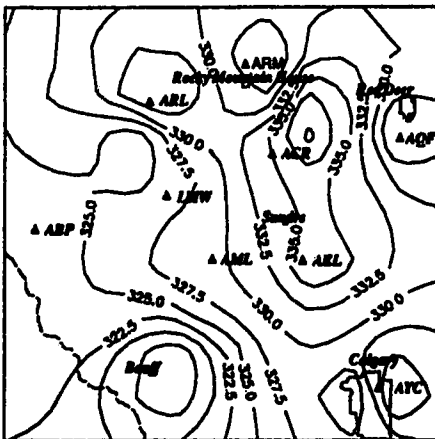
1600 UTC
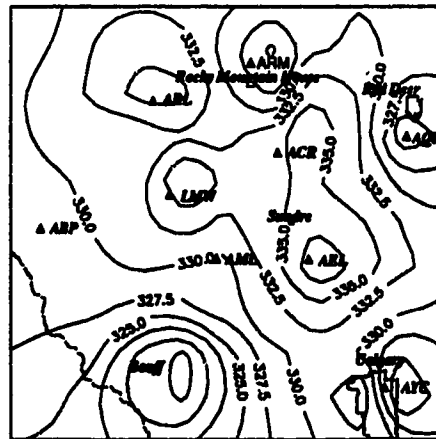
1800 UTC
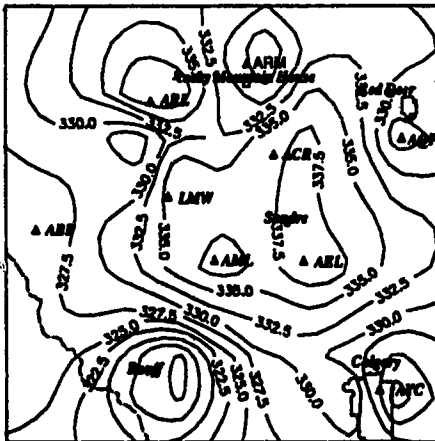
2000 UTC

2200 UTC

0000 UTC

Figure 4.22 Contours of surface equivalent potential temperature θe [degrees K] for the indicated times in the LIMEX85 study region July 11 and 12 1985.

1400 UTC   **1600 UTC**
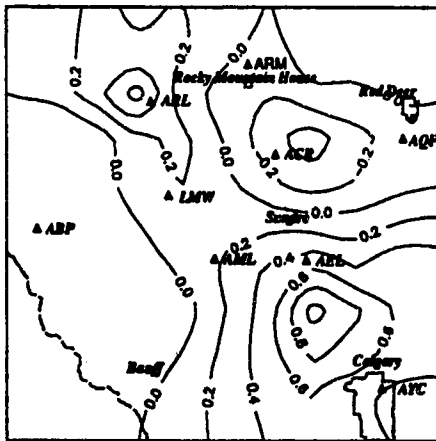
1800 UTC   **2000 UTC**
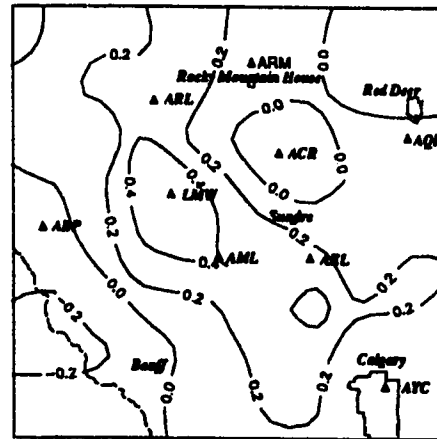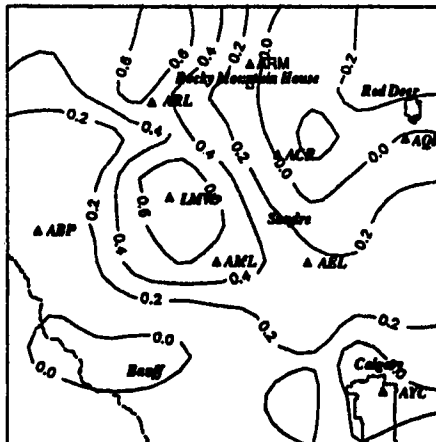
2200 UTC   **0000 UTC**

Figure 4.23. Contours of surface moisture convergence MC [g/kg h] for the indicated times in the LIMEX85 study region July 11 and 12 1985.

76

4.5.6 SURFACE moisture convergence LIMEX85 Region (Figure 4.23)

A regional area of moisture convergence in the northeast quadrant of the LIMEX85 area exists at 1400 UTC to south of AEL by 1800 UTC. This area does produce a storm four hours later at 2000 UTC (Storm H). A centrally located region of moisture convergence at 2200 UTC with peak values greater than 0.6 g/kg h occupies the region around LMW. A region of intense moisture convergence (values in excess of 0.8 g/kg h) is located near Calgary at 0000 UTC. However, the data set used for this analysis has no radar images for 0400 UTC, hence no link can be made to storms which may have formed later. The area of moisture convergence between ARM and AQF at 1600 UTC precedes the storms which develop in that area by 3 to 4 hours (Storms G and H). The rapid change in the forms of these contours (lack of temporal continuity) make any conclusions concerning storm development difficult. These rapid changes are due to changes in the wind fields as the day progresses. The other component of moisture convergence, namely mixing ratio, was slow to evolve. Another important consideration is that the wind direction values used to compute the wind components are two minute average values taken at roughly two hour intervals. Due to the high variance of horizontal surface wind speed and direction at any point during a summer day, it is very difficult to show a smooth transition of the moisture convergence fields with a two hour resolution.

The time series analysis of surface mixing ratio, and θe show a broad maximum generally aligned in the same orientation as the surface trough of low pressure (Figures 4.1 and 4.3). The moisture convergence on this scale appears less organized (low temporal continuity) due to the dependence of the wind fields on topography, which is of a much smaller scale than the analysis allows. A region of maximum moisture convergence is still evident in the areas near those of storm formation as indicated by the radar images. The smaller scale analysis relates regions of maximum mixing ratio and θe with storm positions several hours later, better than the larger scale analysis.

77
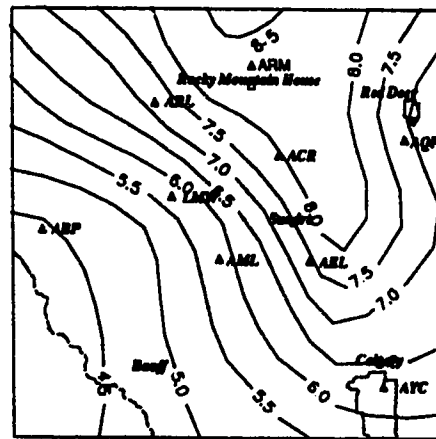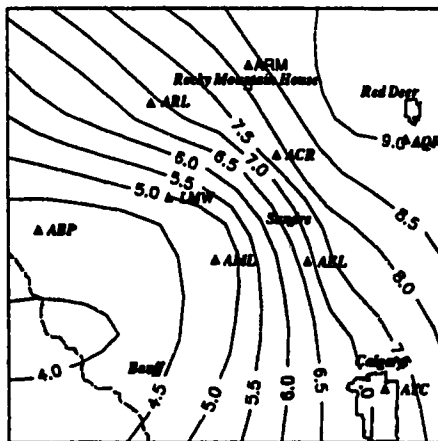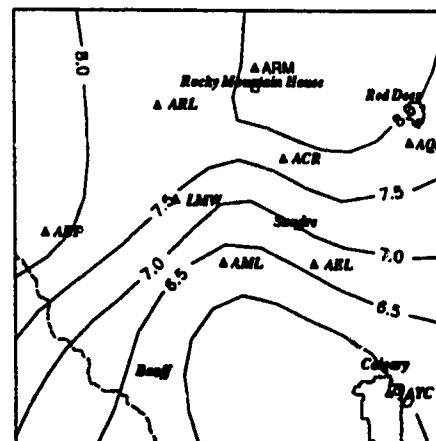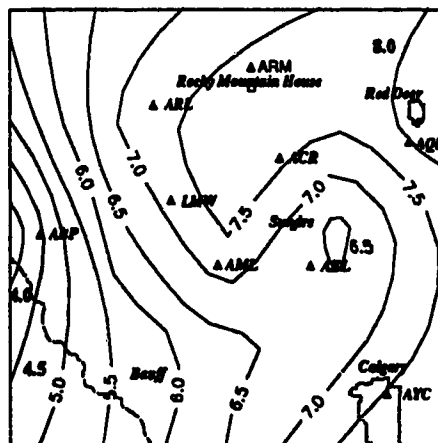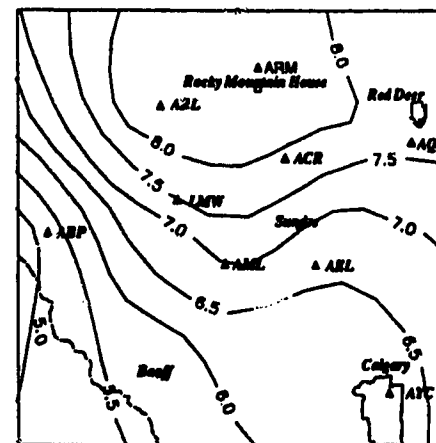
Figure 4.24 Contours of 850 mb mixing ratio r [g/kg] for the indicated times in the LIMEX85 study region July 11 and 12 1985.

78

4.5.7 850 mb Mixing Ratio LIMEX85 Region (Figure 4.24)

A moist tongue with mixing ratios greater than 8.0 g/kg dominates the north-central section of the LIMEX85 study area at 850 mb and 1600 UTC, with a dry region 4.5 g/kg occurring in the southwest. Maximum values continue to prevail in the north and east until 0000 UTC. The orientation of the moist tongue has a more SW-NE to N-S orientation than the surface moisture which was almost exclusively oriented E-W. The maximum values near ACR at 1600 and 1800 UTC precede the storms (Storms G, J and I) in that area by 2 to 5 hours. The tightest gradient is observed at 1800 UTC southwest of ACR, as was the case for the surface.

4.5.8 850 mb Equivalent Potential Temperature LIMEX85 Region (Figure 4.25)

At 1400 evidence of two separate air masses exists. One is warm and moist over the prairie and the other is cooler and dryer over the mountains. This situation persists until 2000 UTC, when the warm moist air mass ($\theta_e > 330K$) dominates the whole region except Calgary. This domination, which is likely due to diurnal heating, continues with maximum values over 337 K near LMW at 2200 UTC. The arrival of 330 K values in the ARM ACR region at 1800 and 2000 UTC coincides with the storm formation (Storms B, C and G) in those areas. The 332.5 K contour around AQF also coincides with a storm which passed through that region (Storm K) at 2200 UTC.

4.5.9 850 mb Moisture Convergence LIMEX85 Region (Figure 4.26)

Moderate moisture convergence in the northeastern sector at 1400 UTC (0.6 g/kg h) is replaced by strong centrally located values (> 0.8 g/kg h) by 2000 UTC. By 0000 UTC, northeastern regions show moisture divergence (-0.4 g/kg h) while central areas show moderate convergence (0.4 g/kg h). The tightest gradients in the region occur at 2000 UTC in the region around ACR, roughly coinciding in time with the storm passages (Storm G) in that area. All the contours from 2000 to 0000 UTC exhibit a strong dipole nature which may reflect a source/sink complex nature. This suggests that Storms H, I, J and K were drawing moisture from the southwest,

79
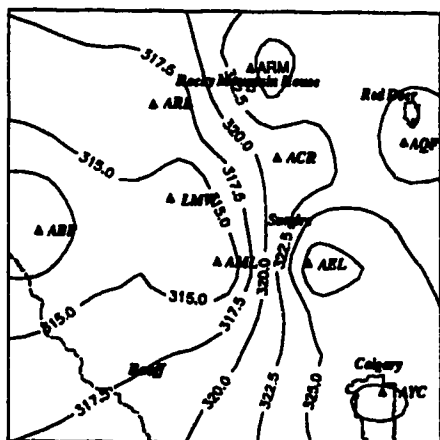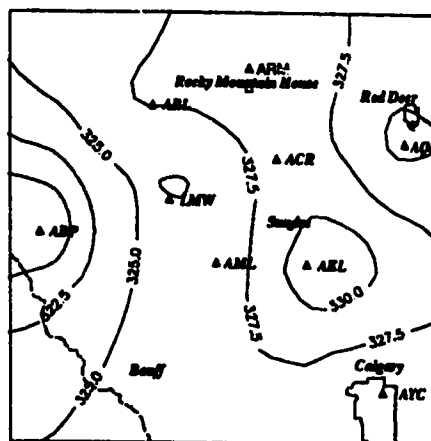
1400 UTC
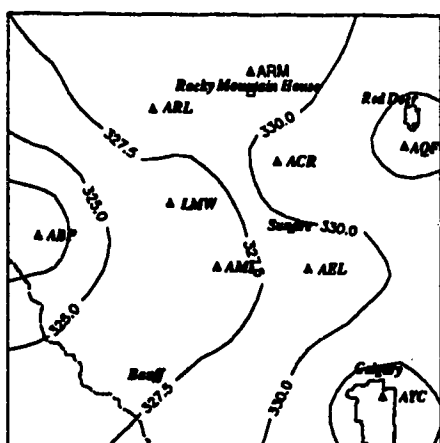
1600 UTC
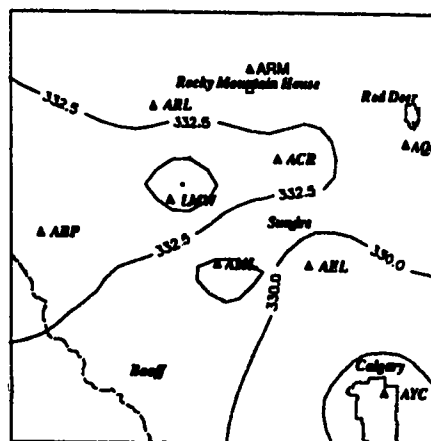
1800 UTC
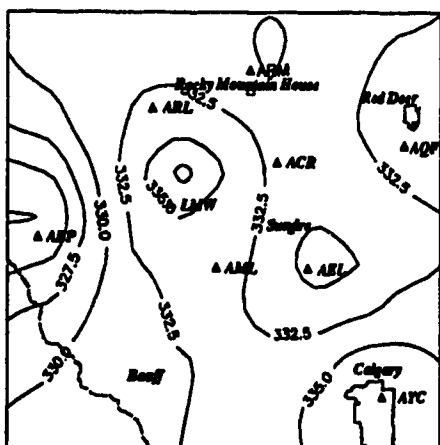
2000 UTC
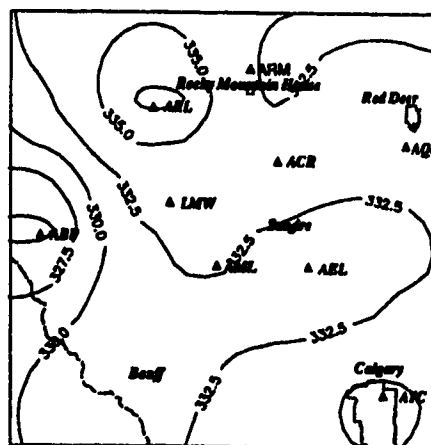
2200 UTC

0000 UTC

Figure 4.25 Contours of 850 mb equivalent potential temperature θe [degrees K] for the indicated times in the LIMEX85 study region July 11 and 12 1985.
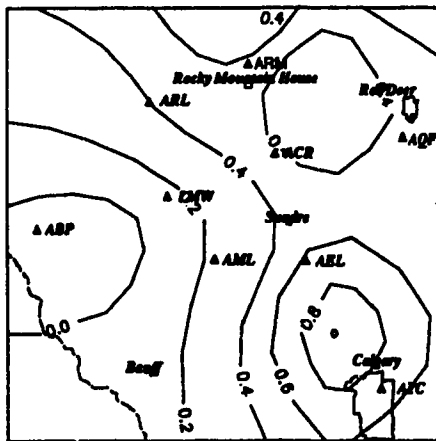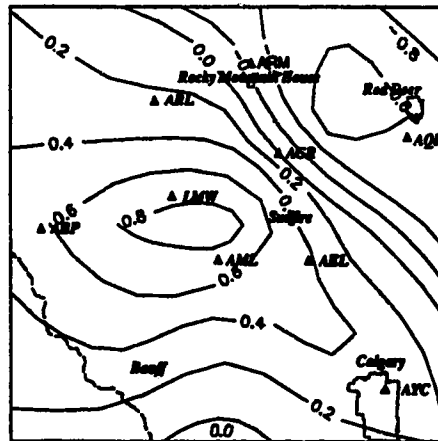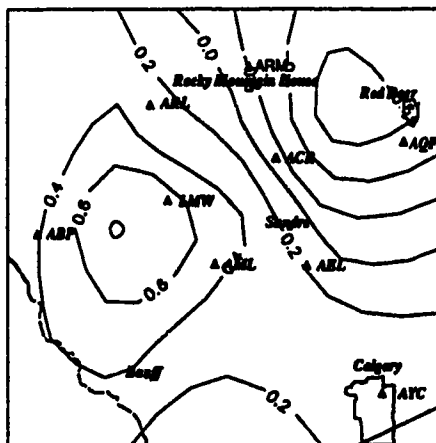
80

1400 UTC
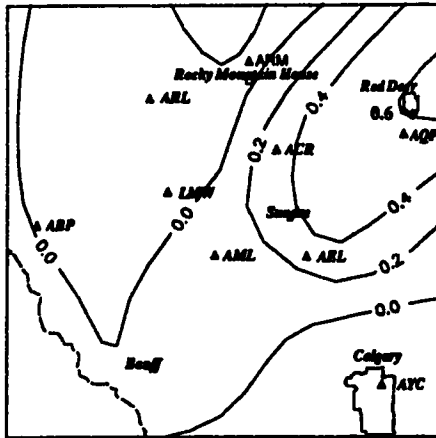
1600 UTC
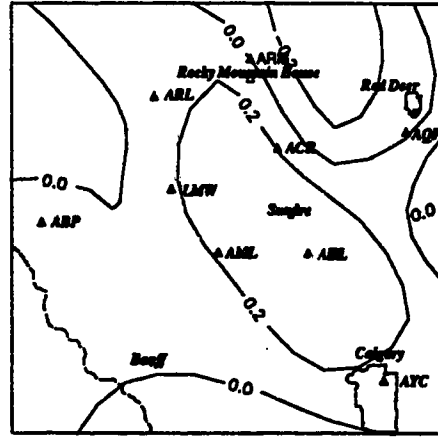
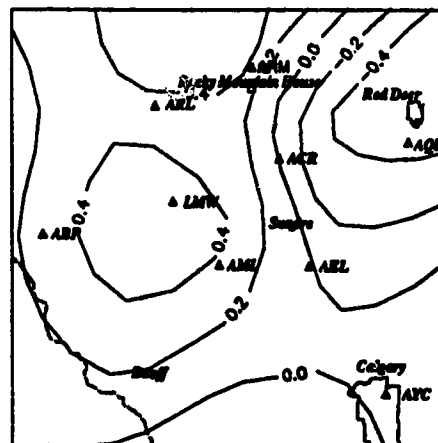**1800 UTC**

2000 UTC

2200 UTC

0000 UTC

Figure 4.26 Contours of 850 mb moisture convergence MC [g/kg h] for the indicated times in the LIMEX85 study region July 11 and 12 1985.

81

however, the 850 mb winds at ACR and ARM from 2000 to 0000 UTC were from the northwest. Therefore, a source/sink link to the observed storms is less credible.

4.5.10   700 mb Mixing Ratio LIMEX85 Region (Figure 4.27)

Moist regions to the south and east from 1400 till 1800 UTC shift to the north and northeast with maximum values greater than 5 g/kg at 0000 UTC. The orientation of the moist tongue shifts from NW-SE to N-S during the course of the day. The 700 mb contour patterns are similar at 1400 and 0000 UTC but much different at 1800. This is probably due to the mid day heating of the lower levels affecting the moisture transport and orientation. The overall gradients of mixing ratio are much reduced from those of 850 mb's or the surface.

4.5.11   700 mb Equivalent Potential Temperature LIMEX85 Region (Figure 4.28)

A warm moist air mass which is situated around AEL persists until 2000 UTC. The region of maximal θe (325 K) resides near ARL at 1800 UTC, roughly coinciding with the storm position (Storm B) at that time. Storms at 2200 (Storm K) and 2000 UTC (Storm H) do not seem to be associated with regions of 700 mb θe maximas. Gradients of θe are fairly small except at 1800 UTC.

4.5.12   700 mb Moisture Convergence LIMEX85 Region (Figure 4.29)

An absence of either convergence or divergence at 1400 UTC is replaced by a divergence dominated field at 1800 UTC with maximum values greater than 0.6 g/kg h around 100 km north of Calgary. The region returns to conditions of moisture divergence dominance by 0000 UTC at 2000 UTC, moderate values of moisture convergence greater than 0.3 g/kg h near AQF and ACR coincide with the storms in that area at 2000 (Storm H) to 2200 UTC (Storm K). This indicates mid-level moisture convergence, which could be helping support the storms growth. Loose gradients in the morning strengthen to a maximum at 2000 UTC.

1400 UTC
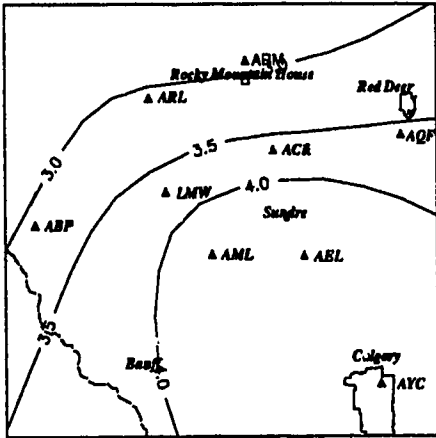
1600 UTC
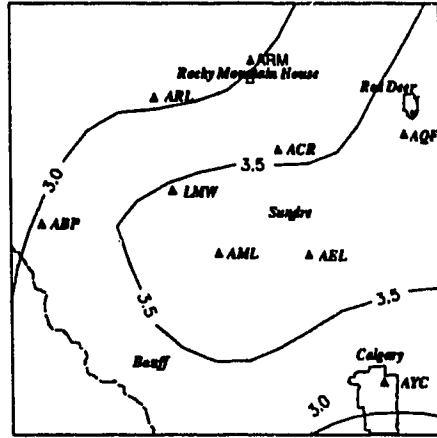
1800 UTC
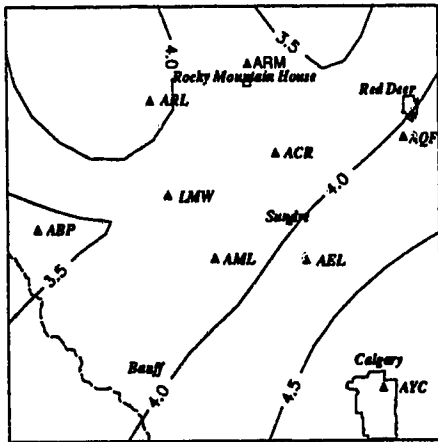
2000 UTC

2200 UTC

0000 UTC

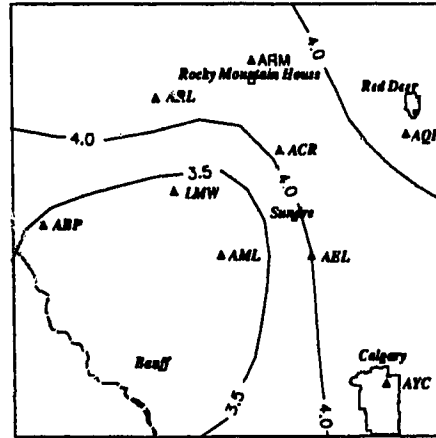Figure 4.27 Contours of 700 mb mixing ratio r [g/kg] for the indicated times in the LIMEX85 study region July 11 and 12 1985.
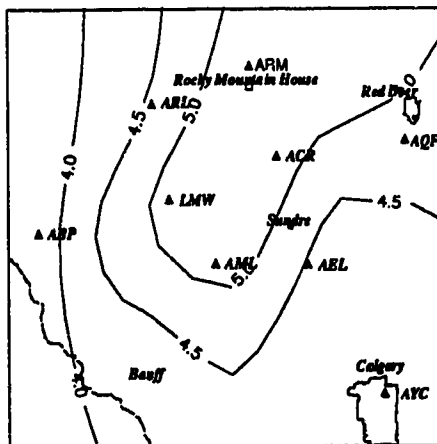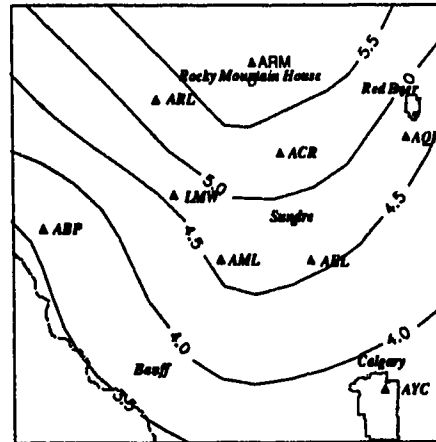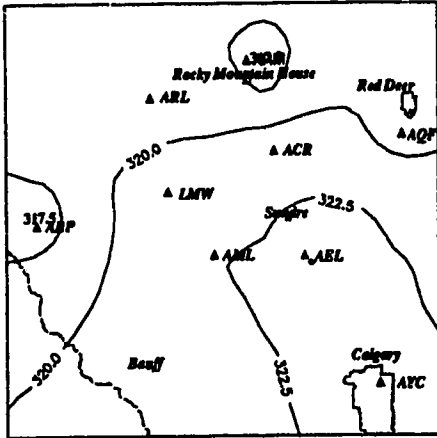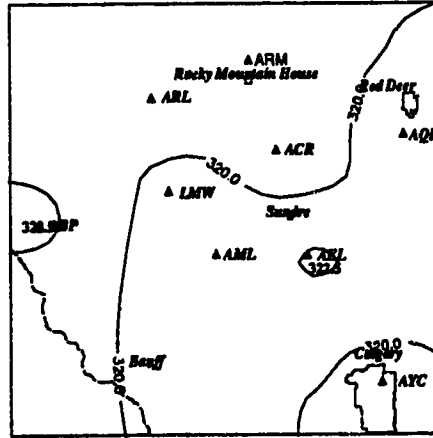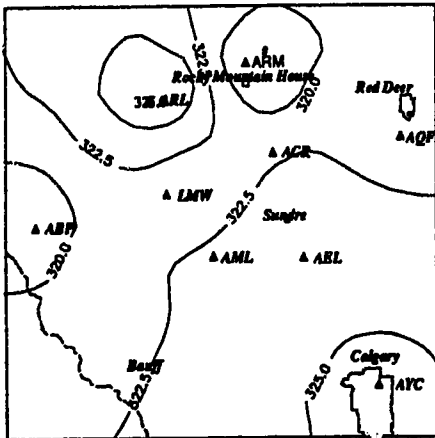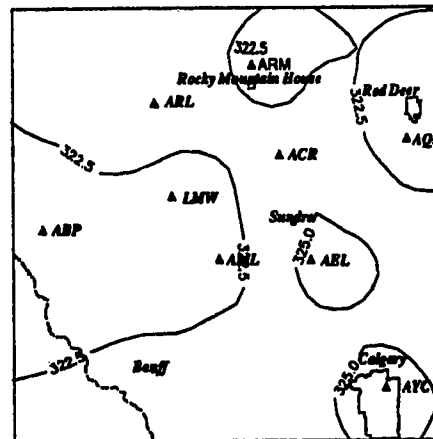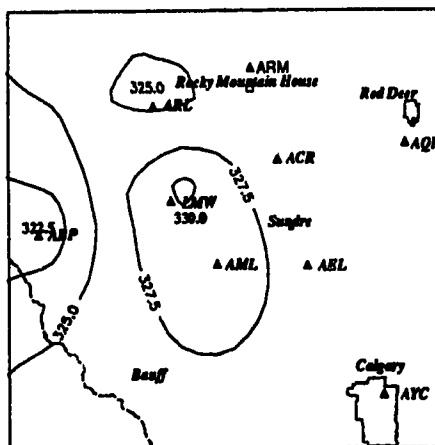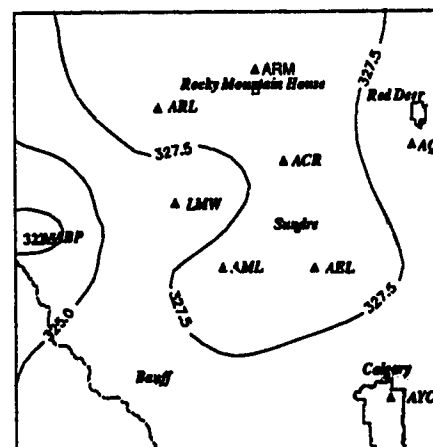
83

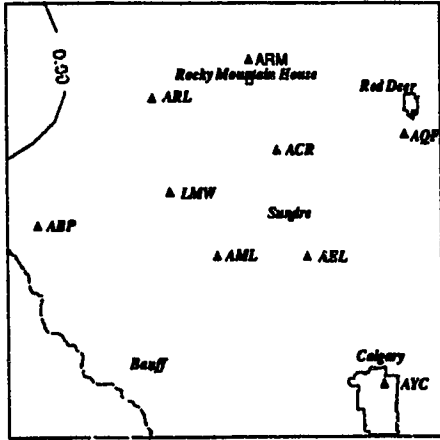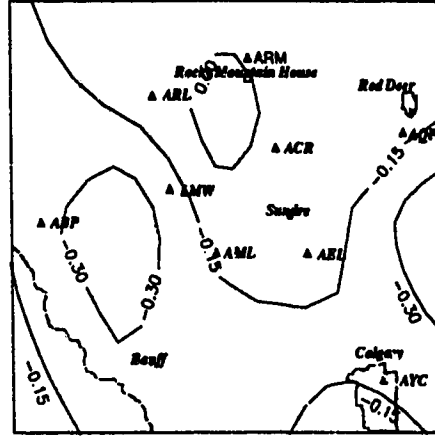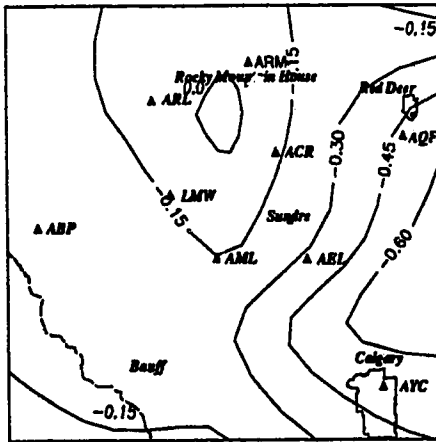1400 UTC

1600 UTC

1800 UTC

2000 UTC

2200 UTC

0000 UTC

Figure 4.28 Contours of 700 mb equivalent potential temperature θe [degrees K] for the indicated times in the LIMEX85 study region July 11 and 12 1985.
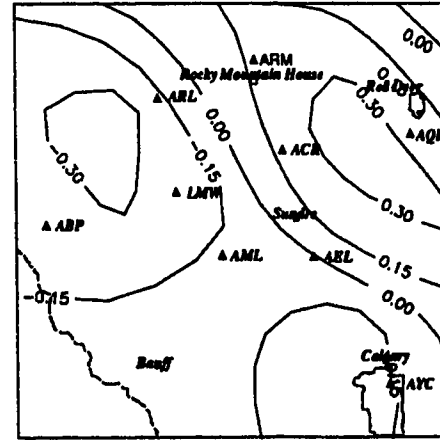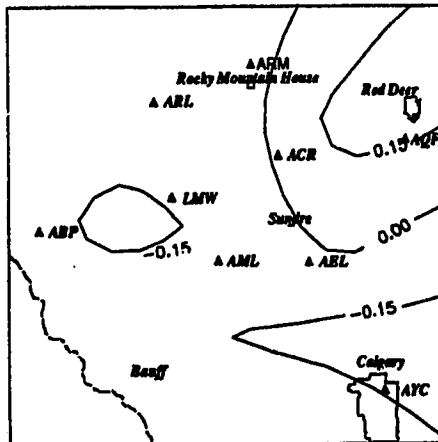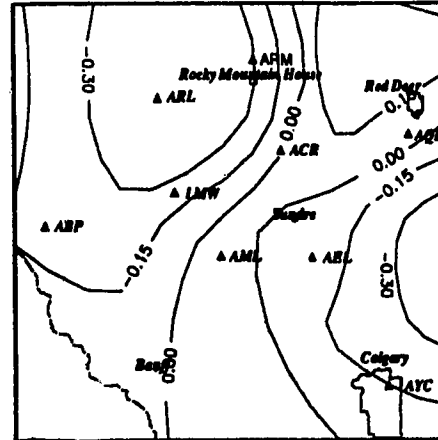
1400 UTC

1600 UTC

1800 UTC

2000 UTC

2200 UTC

0000 UTC

Figure 4.29 Contours of 700 mb moisture convergence MC [g/kg h] for the indicated times in the LIMEX85 study region July 11 and 12 1985.

85

4.5.13   600 mb Mixing Ratio LIMEX85 Region (Figure 4.30)

Maximum values to the northwest at 1400 UTC become a pool in the south central region of the grid by 1800 UTC. Maximal values dominate the south and east for 2200 and 0000 UTC. Weak gradients persist for the whole test period. No correlation is evident between storm position and regions of maximum mixing ratio at the 600 mb pressure level. The lack of temporal continuity exhibited by the contours of mixing ratio at 600 mb is most likely related to the high values of wind speed at this level (averaging 12.9 m/s). Winds of this speed are capable of advecting moisture roughly 90 km in a 2 hour interval.

4.5.14   600 mb Equivalent Potential Temperature LIMEX85 Region (Figure 4.31)

Equivalent potential temperature is almost constant across the region from 1400 to 1600 UTC. A gradient develops at 1800 UTC with the larger values to the southeast and the smaller values to the northeast. (Park and Sikdar, 1982) and (Foote and Fankhauser, 1973) state that regions that experience convective outbreaks often observe low values at θe at 600 to 500 mb. Storms G, H, I and K occupy a position in the northeast quadrant of the LIMEX85 grid. This gradient slackens by 2000 UTC and then tightens by 2200 and 0000 UTC retaining its overall orientation. The contours suggest that high θe values were being advected from the south or southeast. However, the winds at 600 mb for stations AML, AEL and AYC range from 240 to 270°, or from the west southwest.

4.5.15   600 mb Moisture convergence LIMEX85 Region (Figure 4.32)

An absence of moisture convergence or divergence persists till 1800 UTC when a region of moisture convergence (0.3 g/kg h) occurs 50 km southwest of Rocky Mountain House. The rest of the study hours are dominated by moisture divergence especially in the southeast quadrant. The maximum values at 1800 UTC correspond well with the position of the storms (Storms B and C) which developed at that time. It
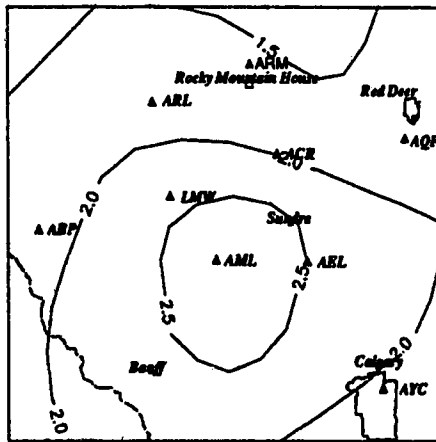
1400 UTC
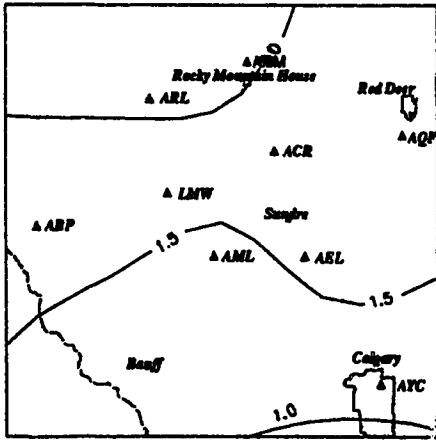
1600 UTC
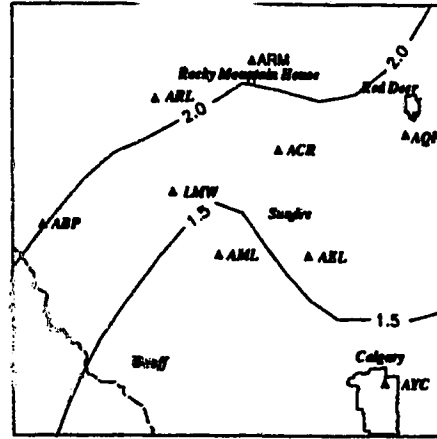
1800 UTC

2000 UTC

2200 UTC

0000 UTC

Figure 4.30. Contours of 600 mb mixing ratio r [g/kg] for the indicated times in the LIMEX85 study region July 11 and 12 1985.
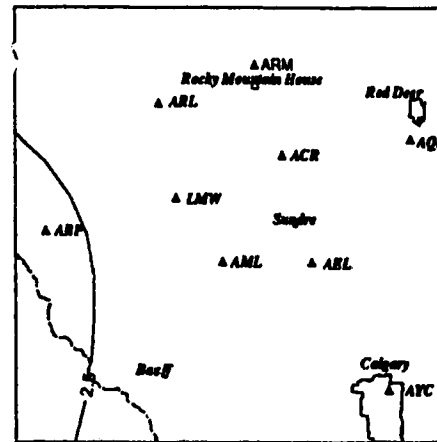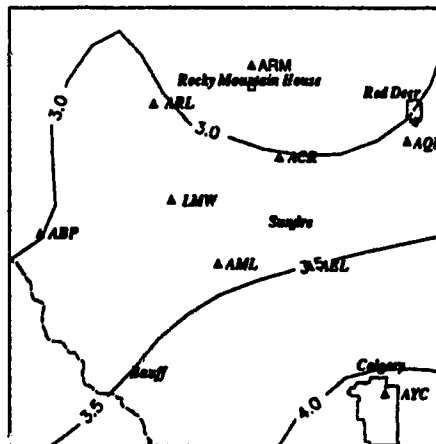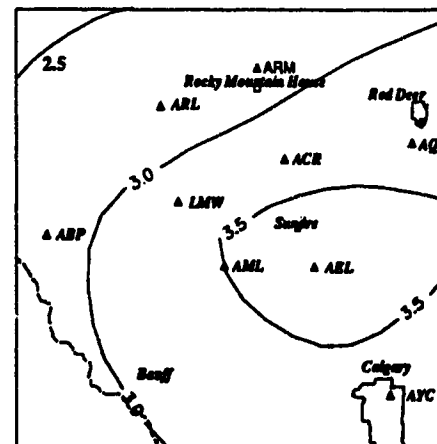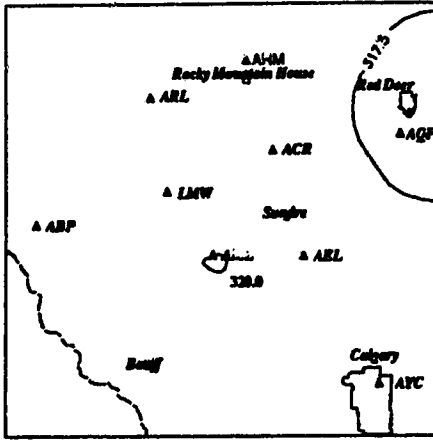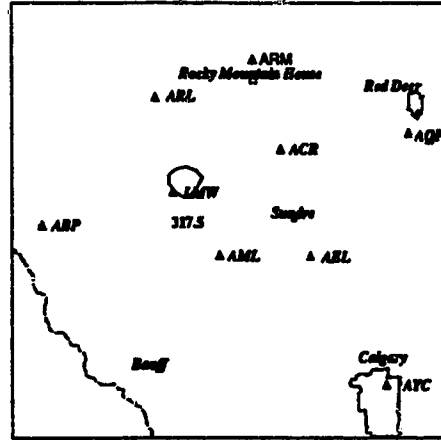
1400 UTC

1600 UTC

1800 UTC

2000 UTC

2200 UTC

0000 UTC

Figure 4.31 Contours of 600 mb equivalent potential temperature θe [degrees K] for the indicated times in the LiMEX85 study region July 11 and 12 1985.

88

1400 UTC
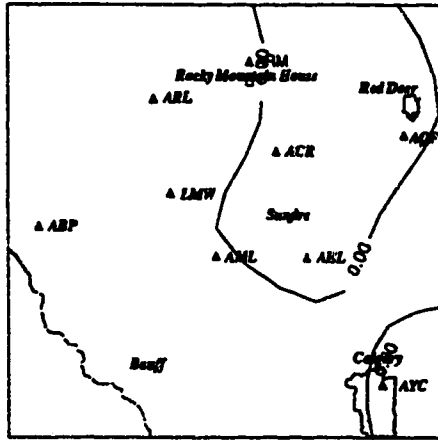
1600 UTC
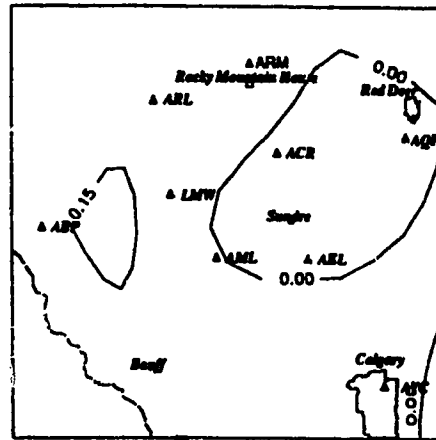
1800 UTC

2000 UTC

2200 UTC

0000 UTC

Figure 4.32 Contours of 600 mb moisture convergence MC [g/kg h] for the indicated times in the LIMEX85 study region July 11 and 12 1985.

89

would appear that these storms may have been fueled in part by upper-level moisture convergence.

4.5.16 500 mb Mixing Ratio LIMEX85 Region (Figure 4.33)

Very little variation in the LIMEX85 area moisture content occurs at 500 mb. A maximum of 2 g/kg resides in the northeast corner at 1800 UTC. This maximum reappears in the centre of the LIMEX85 area at 0000 UTC. Weak gradients persist throughout the study period. The maximum estimated error in the calculation of mixing ratio (see Section 4.8) was 1.8 g/kg, which is of the order of all the 500 mb values. It is possible that the contours at this level are dominated by errors and hence not particularly revealing.

4.5.17 500 mb Equivalent Potential Temperature LIMEX85 Region (Figure 4.34)

A tight centre of high θe values to the southwest at 1400 UTC dissipates to an almost uniform situation at 1600 UTC. A tighter gradient re-establishes at 1800 UTC with the largest values situated in the northeast (332 K). A slacker gradient persists from 2000 UTC until 0000 UTC with the largest values in the southeast corner of the grid near Calgary. Relatively low values of θe are found south of Rocky Mountain House at 1800 UTC. This is where Storm G was observed. This lends some support to the previous contention that regions where storms occur have a decrease in θe in the vertical and a minimum at the 600 and 500 mb levels.

4.5.18 500 mb Moisture Convergence LIMEX85 Region (Figure 4.35)

Early time periods 1400 and 1600 UTC show no significant values of moisture convergence or divergence. At 1800 UTC, a region of moderate moisture convergence (0.45 g/kg h) develops 50 km northwest of Caroline, with a region of significant moisture divergence occurring (-0.5 g/kg h) near Red Deer, and strong gradients in between. These conditions dissipate from 2000 until 0000 UTC. The maximum

1400 UTC
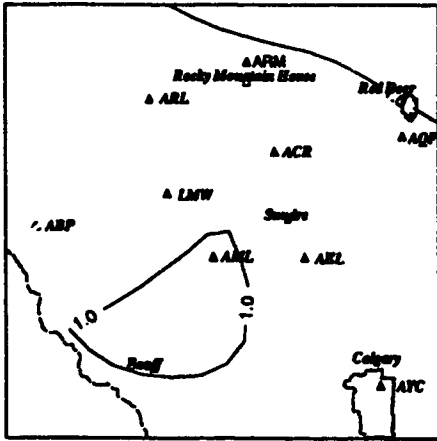
1600 UTC
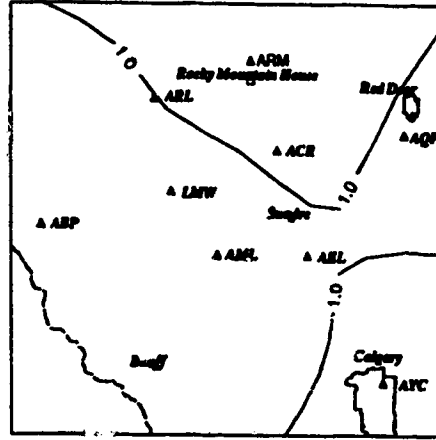
1800 UTC
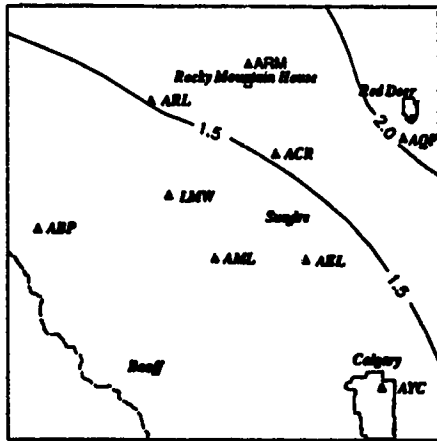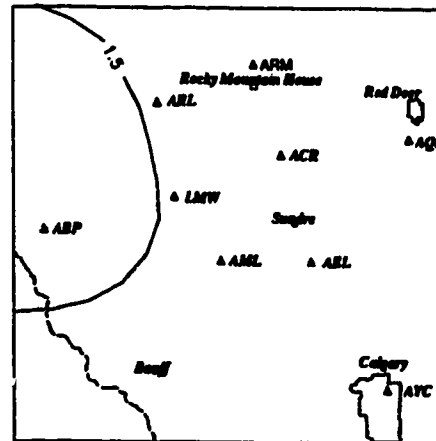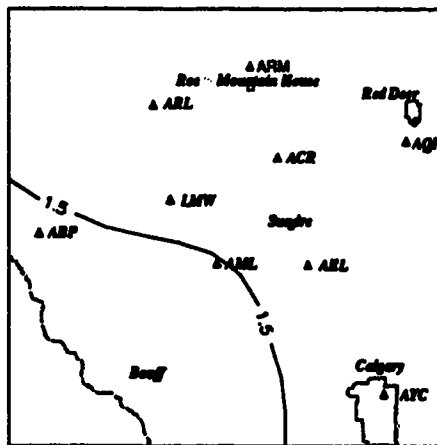
2000 UTC
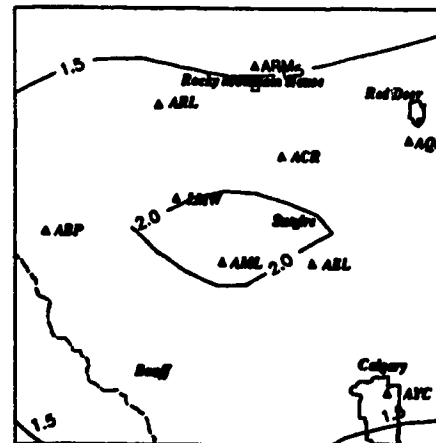
2200 UTC

0000 UTC

Figure 4.33 Contours of 500 mb mixing ratio r [g/kg] for the indicated times in the LIMEX85 study region July 11 and 12 1985.
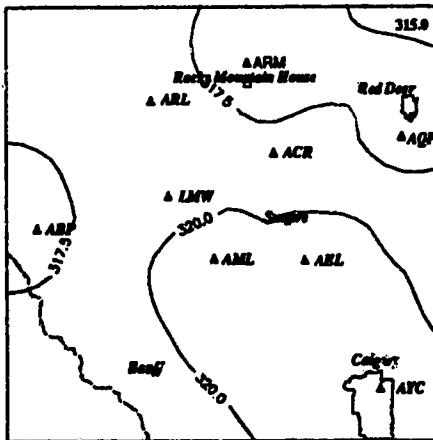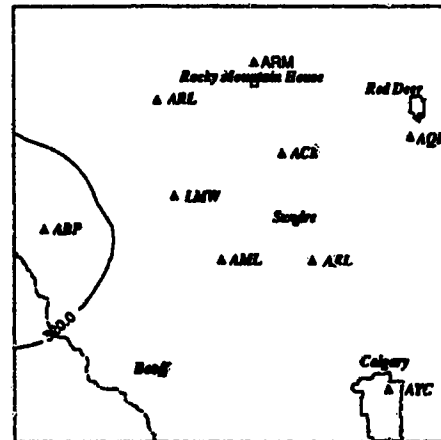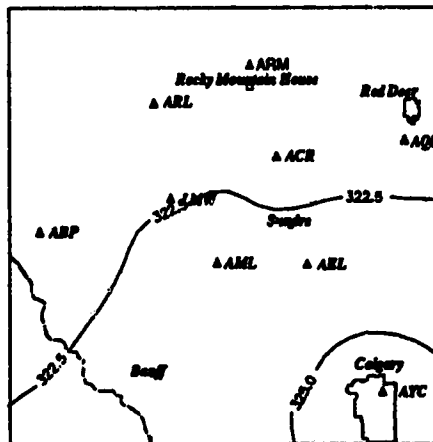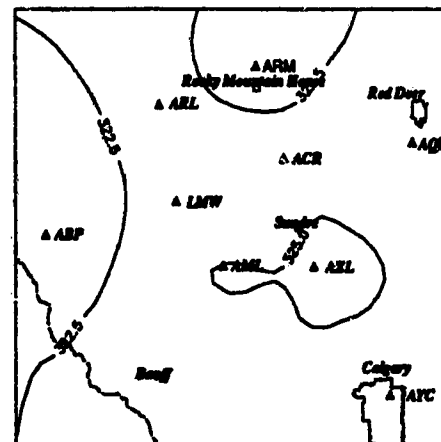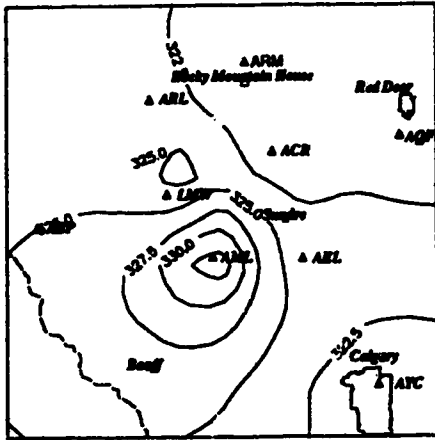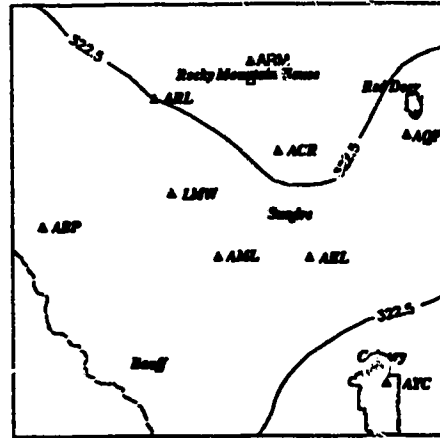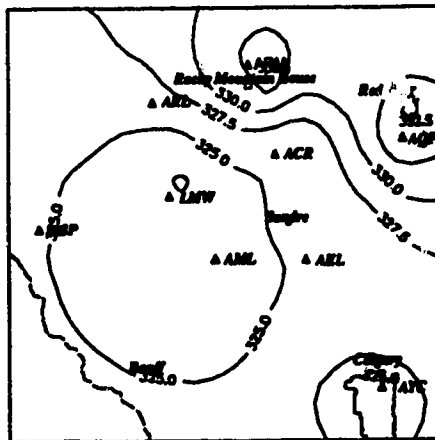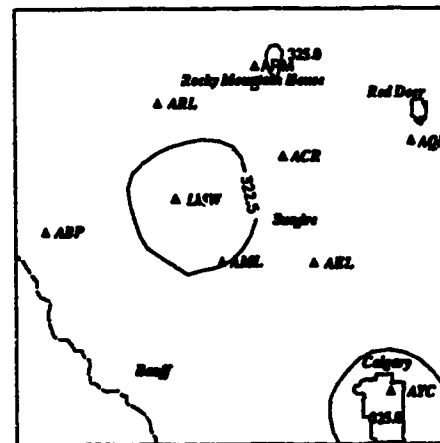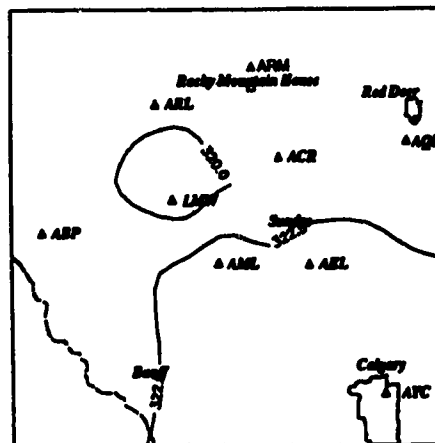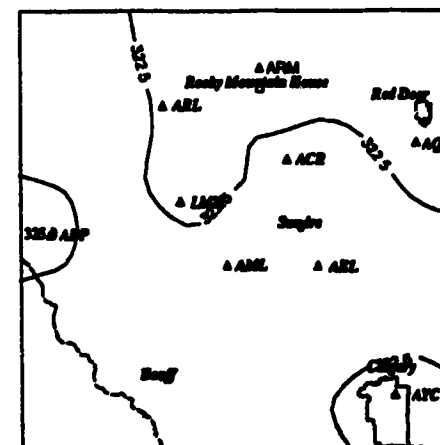
Figure 4.34. Contours of 500 mb equivalent potential temperature θe [degrees K] for the indicated times in the LIMEX85 study region July 11 and 12 1985.
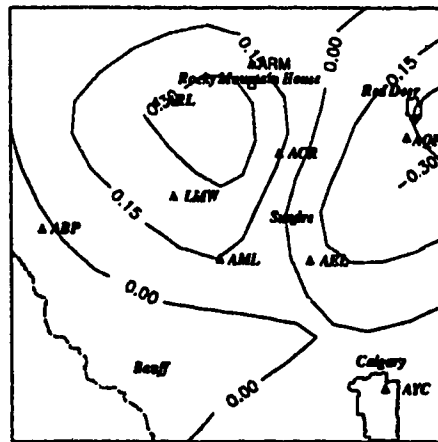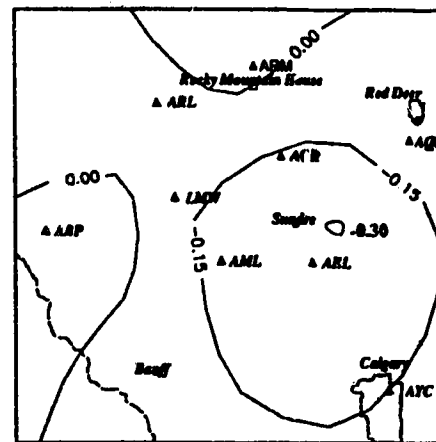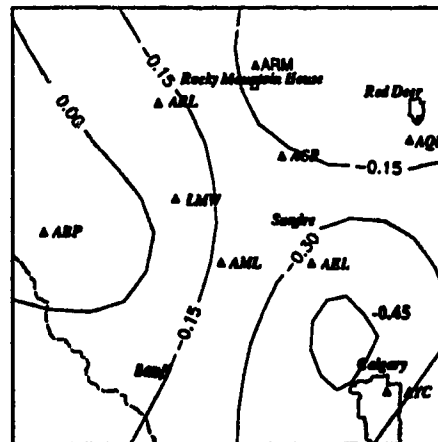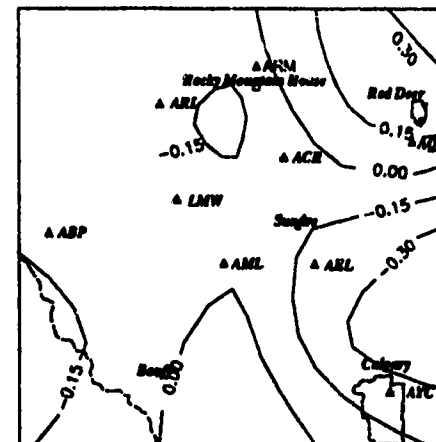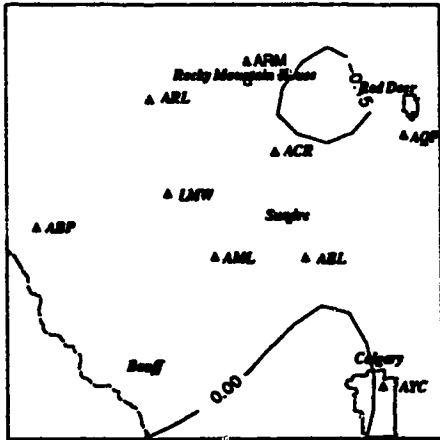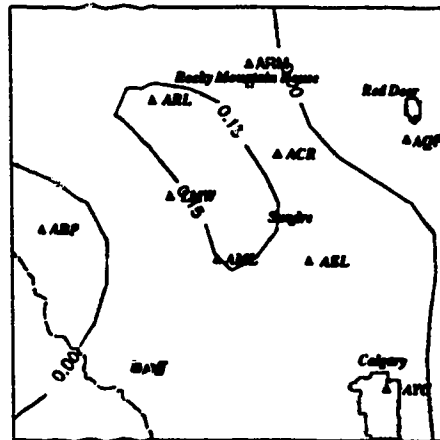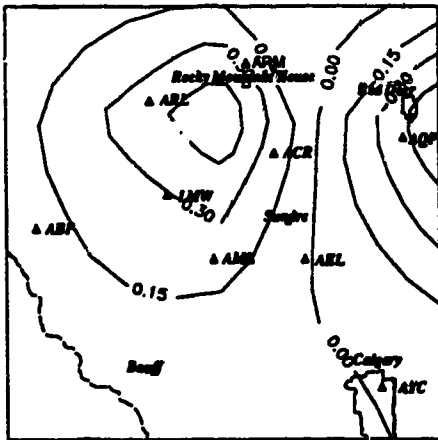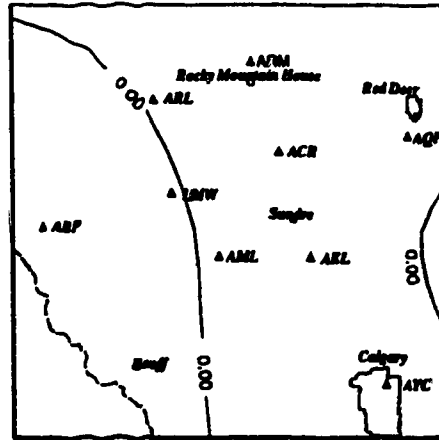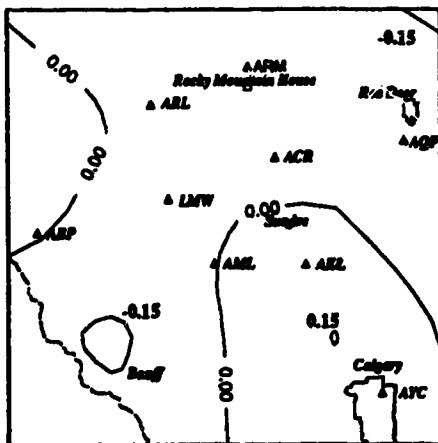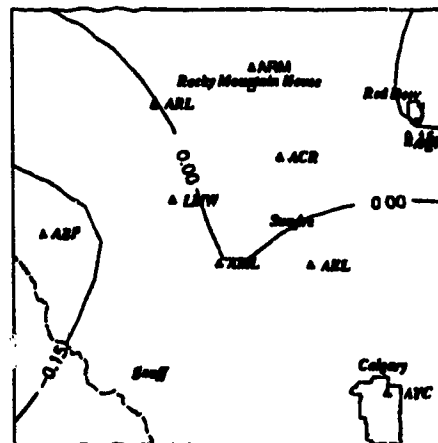
Figure 4.35 Contours of 500 mb moisture convergence MC [g/ kg h] for the indicated times in the LIMEX85 study region July 11 and 12 1985.

values of 0.45 g/kg h between ARL and ACR at 1800 UTC are near the storms positions (Storms B and C) which occur in that region. The 500 mb level would seem to be too high (5 km) for moisture convergence to be affecting small storms.

4.5.19 Integrated Moisture Convergence LIMEX85 Region (Figure 4.36)

High values of IMC dominate the northeast corner of the LIMEX85 area at 1400 UTC. By 1600 UTC, a cell of moderate IMC develops northwest of ACR. This cell intensifies by 1800 UTC with peak values greater than 100 g mb/kg h. The gradients dissipate, along with the maximum values by 2000 UTC. By 2200 UTC, a centre of divergence appears near Red Deer (80 g mb/kg h). At 0000 UTC, IMC is at a maximum (50 g mb/kg h) 50 km south of LMW. The maximum at 1600 and 1800 UTC is very near the small storms (Storms B, C, D and G) which developed from 1800 to 1900 UTC. The divergence values near Red Deer at 2200 UTC would most likely serve to dissipate the small storm (Storm K) which occupied that region.

Almost all the moisture fields at all levels show a predominant near east-west gradient at 1800 UTC. This could be related to the position of the synoptic trough (Figure 4.3) and or the mountain barrier.

4.6   TIME-HEIGHT CROSS-SECTIONS FOR INDIVIDUAL STATIONS

Contoured time-height cross-sections of mixing ratio, equivalent potential temperature and moisture convergence were prepared for the following locations:

- Mountainaire Lodge
- Site X 20 km northwest of Calgary
- Red Deer
- Site Y 20 km west of Rocky Mountain House (Storm B)
- Site Z 25 km northwest of Red Deer (Storm K)

94
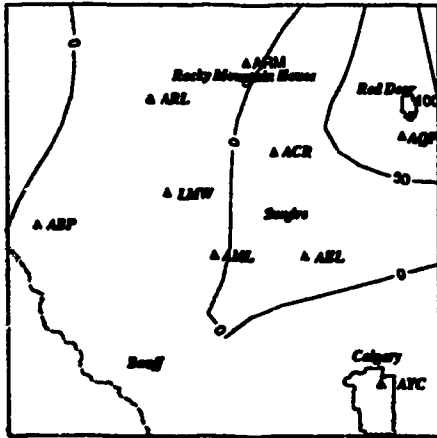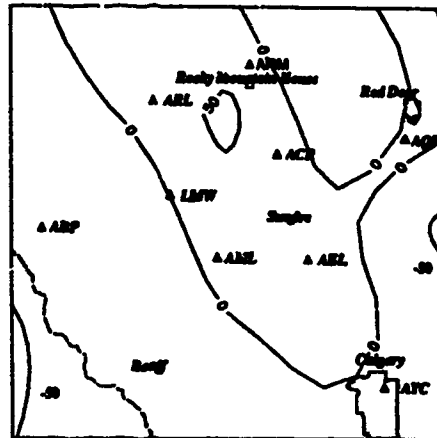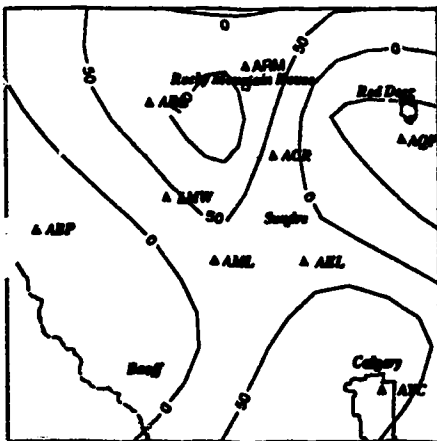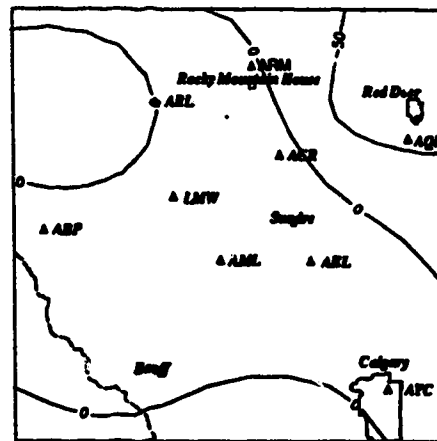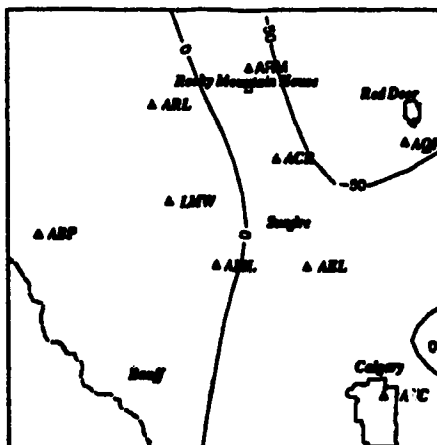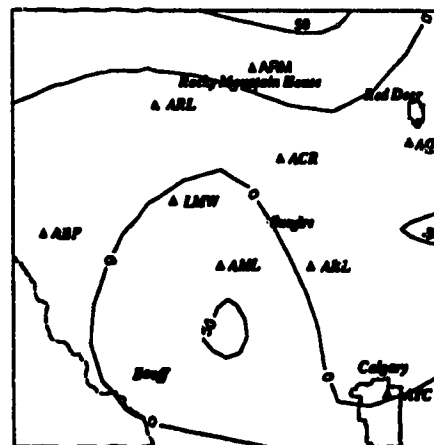
Figure 4.36 Contours of integrated moisture convergence IMC [mb g/kg h] for the indicated times in the LIMEX85 study region July 11 and 12 1985.

Mountainaire Lodge was chosen to represent a mountain station and a station which was removed from any storm activity. Site X is representative of a prairie station and one where no storms were observed. Red Deer is a prairie station and one close to the storm at 2200 UTC (16:00 MDT), Storm K. Site Y has a storm at 1900 UTC (13:00 MDT). Site Z is the approximate location of the Storm K at 2200 UTC.

The main objective in this section is to look for evidence that the evolution of the moisture fields (in the vertical), over these stations, is distinct for stations near or at storm locations, as compared to those removed from any convective activity. It should also be possible to link the moisture fields to the existence or absence of storms by noting the changes in the fields (in the vertical) over time. All heights are heights above ground level.

Figure 4.37 for AML shows a general increase in θe values (from 315 to 333 K) at the surface from 8:00 until 16:00 MDT. This represents the diurnal surface heating. At mid-levels (2.5 km), there is a much smaller increase (from 317 to 323 K). Upper levels show almost constant θe values. The equivalent potential temperature gradient below 4 km ($\partial \theta e/\partial z$) in the vertical ranges from -1 °C/km at 10:00 MDT to -2.0 °C/km at 18:00 MDT. This indicates a gradual increase in potential instability during the day. The surface mixing ratios peak at 10:00 (7 g/kg) and at 16:00 MDT (8 g/kg). There is a reduction in mixing ratios around 14:00 MDT for heights up to 3 km forming a dip in the contours. Surface moisture convergence is at a maximum at 16:00 MDT (1.0 g/kg h). Small values of upper-level moisture convergence (0.2 g/kg h) are evident from 10:00 to 12:30 MDT. Mid-level values are generally in the zero range. The increase in mixing ratio values at mid-levels at 12:00 MDT is associated with the mid-and upper-level moisture convergence at 12:00 MDT. The dip in mid-level mixing ratio values at 14:00 MDT is linked with the mid-level divergence at the same time.

Figure 4.38 shows time height cross-sections for Site X, which did not experience any storm development or passage. Lower level θe values increase from 322 K at 8:00 MDT to 334 at 20:00 MDT. Mid- and upper-level θe's also increase but to a smaller degree. $\partial \theta e/\partial z$ indicates potential instability ranging from -1.0 °C/km at

96

Figure 4.37. Time-height cross-section contours of equivalent potential temperature θe
(degrees K), mixing ratio (g/kg), and moisture convergence (g/kg h) for the Station
Mountainaire Lodge (AML).
Note 12:00 MDT = 1800 UTC

97

Figure 4.38. Time-height cross-section contours of equivalent potential temperature θe (degrees K), mixing ratio (g/kg), and moisture convergence (g/kg h)for a LIMEX85 location with no storm passage.
Note 12:00 MDT = 1800 UTC

98

12:00 MDT to -1.6 °C/km at 19:00 MDT. A surface based region of maximum mixing ratio (7 g/kg) exists from 9:30 to 12:30 MDT. A fairly tight vertical gradient slackens as the day progresses. On the whole, the mixing ratio displays little variation at a particular height above the surface throughout the day. Large values of surface moisture convergence (1.2 g/kg h) occur at 12:00 MDT. No appreciable mid or upper-level moisture convergence is evident. Mid-level moisture divergence and relatively small $\partial\theta e/\partial z$ values support the lack of convective activity over this station.

Figure 4.39 for AQF shows a slow increase in surface θe values in time (320 to 330 K). The entire day exhibits potential instability ($d\theta e/dz < 0$), with values ranging from -1.5 °C/km early in the day to -2.2 °C/km at 20:00 MDT. An early morning mixing ratio maximum (9 g/kg) occurs at 10:00 MDT. The 8 g/kg contour which is near the surface at 12:00 MDT is lifted a kilometre for the whole afternoon period. This would seem to be related to the Storm K northwest of Red Deer at 16:00 MDT. The 2 g/kg contour shows a marked rise at 12:00 MDT. Low level moisture convergence at 8:00 MDT (0.6 g/kg h) decays into small values of divergence in mid afternoon and then returns to convergence values by 10:00 MDT. A region of upper-level moisture divergence is evident for the period 10:00 to 13:00 MDT.

Conditions for the site chosen to depict Storm B Site Y are shown in Figure 4.40. A consistent increase in surface θe values (318 to 334 K) is evident as the day progresses. This is true for mid-level values also. The $\partial\theta e/\partial z$ values range from -0.5 °C/km at 9:00 MDT to -2.3 °C/km at 16:00 MDT. Surface mixing ratios of 8 g/kg at 9:00 MDT are lifted to one kilometre until 13:00 MDT. A tight vertical gradient in mixing ratio exists between 1 and 2 km for this time period. Upper level mixing ratios show a small increase after 13:00 MDT. Surface moisture convergence is at a maximum (0.8 g/kg h) at 16:00 MDT. A region of moderate upper-level moisture convergence exists from 10:00 until 14:00. There is also moderate moisture convergence at the surface for these times. This should have helped foster the Storm B, which appeared at 13:00 MDT.

Figure 4.39. Time-height cross-section contours of equivalent potential temperature θe
(degrees K), mixing ratio (g/kg), and moisture convergence (g/kg h)
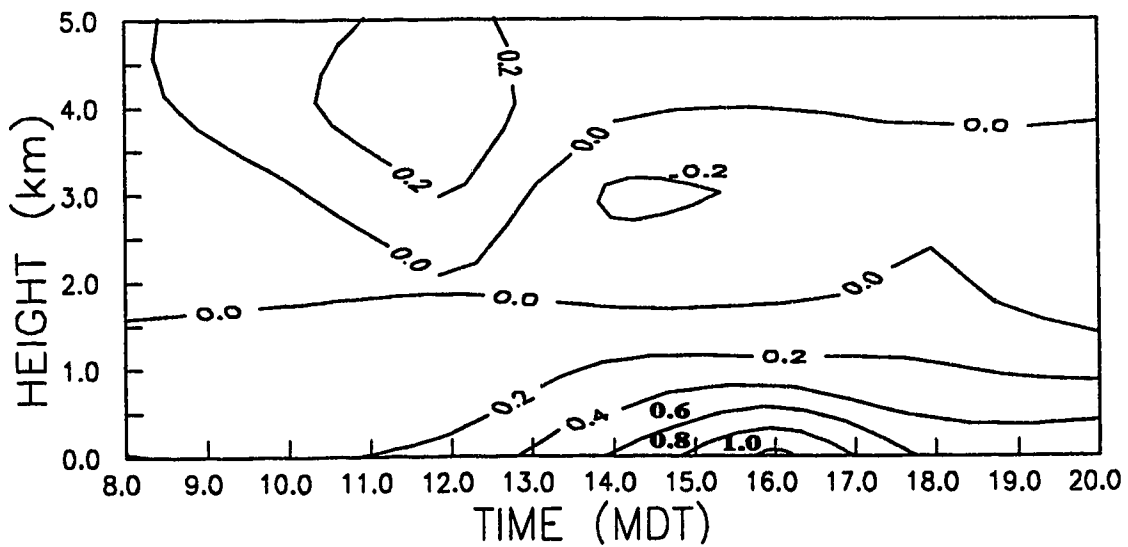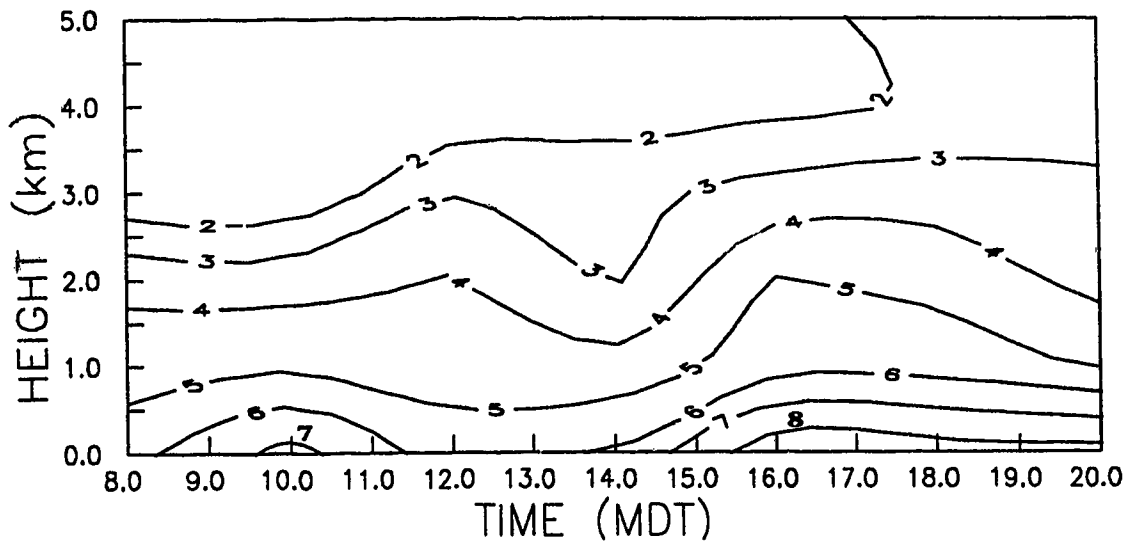for the Station Red Deer (AQF).
Note 12:00 MDT = 1800 UTC

100
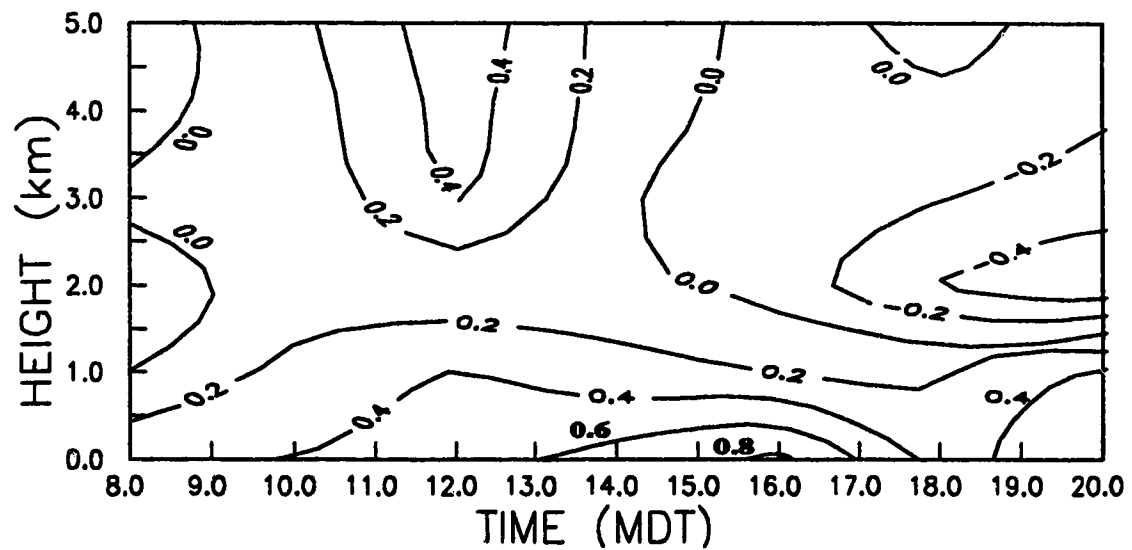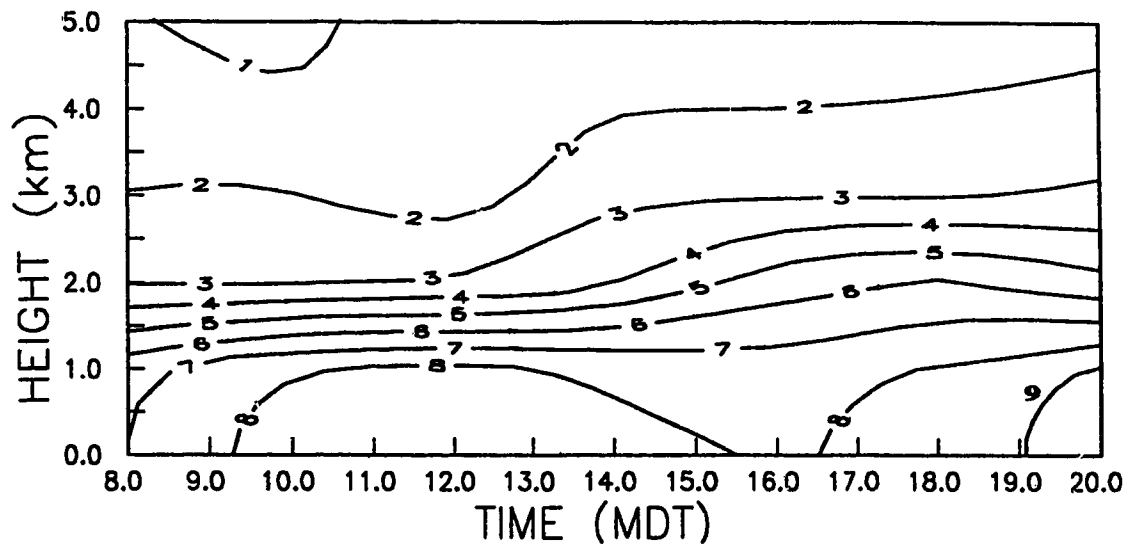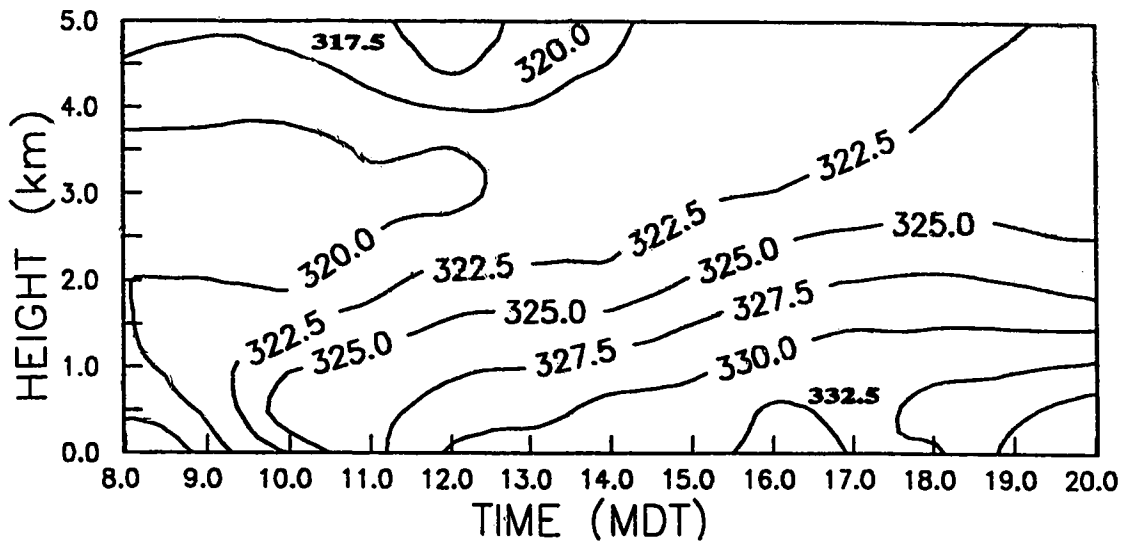
Figure 4.40. Time-height cross-section contours of equivalent potential temperature θe (degrees K), mixing ratio (g/kg), and moisture convergence (g/kg h) for the position of the LIMEX85 Storm B at 1800 UTC.
Note 12:00 MDT = 1800 UTC

Storm K (Site Z) conditions are displayed in Figure 4.41. Surface θe values increase during the day from 322 K to 331 K. Mid level values also increase but to a lesser degree. An upper-level pool of warm θe values (328 K) occurs at 11:00 MDT.

16:00 MDT $\partial\theta e/\partial z$ values are -2.4 °C/km. The 8 g/kg mixing ratio contour is lifted from the surface in the early morning to 1 km. A tight vertical gradient of mixing ratio until 12:00 MDT begins thereafter to diminish and increase in upper values. The 2 g/kg contour has a sharp rise at 12:00 MDT. Low level moisture 0.6 (g (kg h)) convergence at 8:00 MDT is replaced by divergence -0.6 (g (kg h)) by late afternoon. Slight upper-level moisture convergence is evident from 17:00 to 19:00 MDT. The mid-level moisture convergence is likely related to the Storm K, observed at 16:00 MDT.

4.6.1 Summary of Time-Height Cross-Sections

Stations over which a storm passes or which are near to storm passage show higher surface values of mixing ratio (8 to 9 g/kg), which also results in a stronger vertical gradient of mixing ratio than do other stations. The contours of equivalent potential temperature for the five locations are remarkably similar at all locales except for one feature. The stations near or at a storm development region show larger magnitudes of potential instability ($\partial\theta e/\partial z$). The location chosen to illustrate no storm passage (Site X) is dominated by mid level divergence of moisture and low-level convergence. This situation intensifies for surface convergence 1.2 (g (kg h)) at 12:00 MDT and for mid level divergence +0.4 (g (kg h)) at 11:00 and 15:00 MDT. The surface to mid-level gradient is strong at 12:00 MDT. Mountainaire Lodge shows increasing low-level and surface moisture convergence in the morning and early afternoon. Mid- and upper-levels oscillate from moisture divergence to convergence as the day progresses but the amplitude is small. The Red Deer station switches from low-level moisture convergence to divergence as morning turns to afternoon. Upper- and mid-level values of convergence peak at 12:00 MDT (g (kg h)) and then diminish to values near 0.1 (g (kg h)) in late afternoon 18:00 MDT. Site Y has high values of upper-level
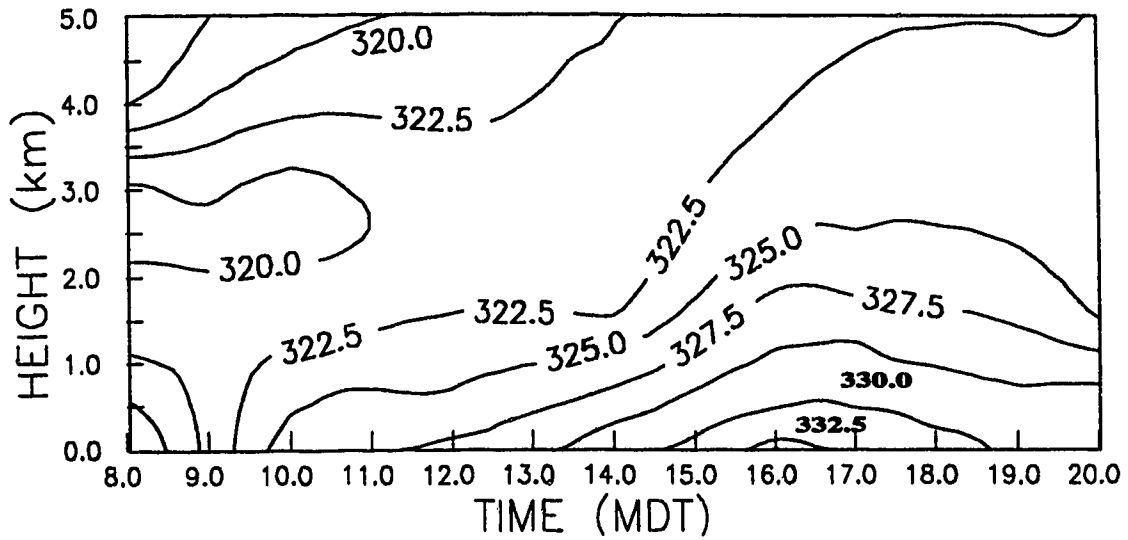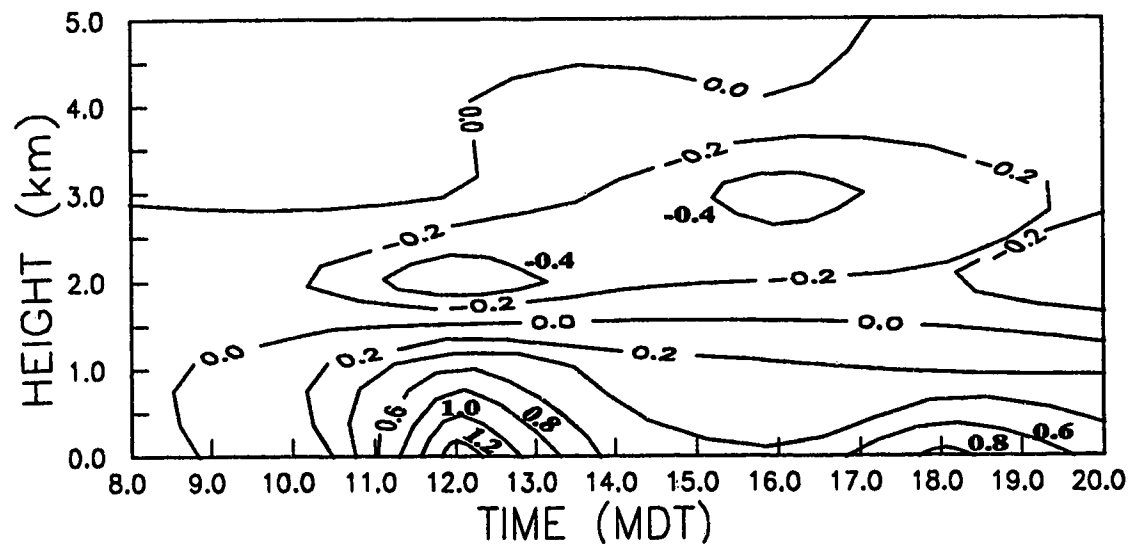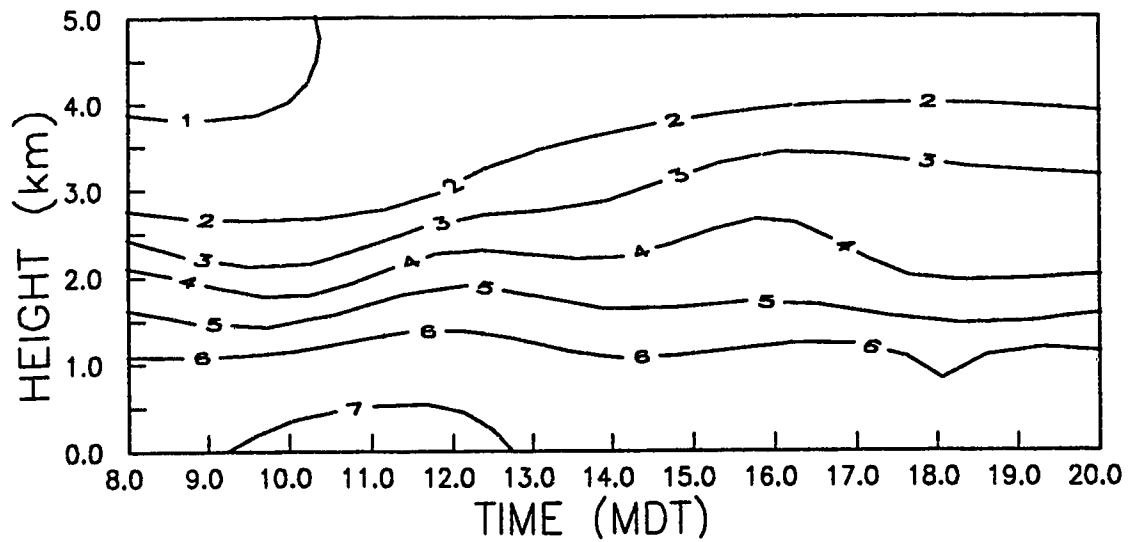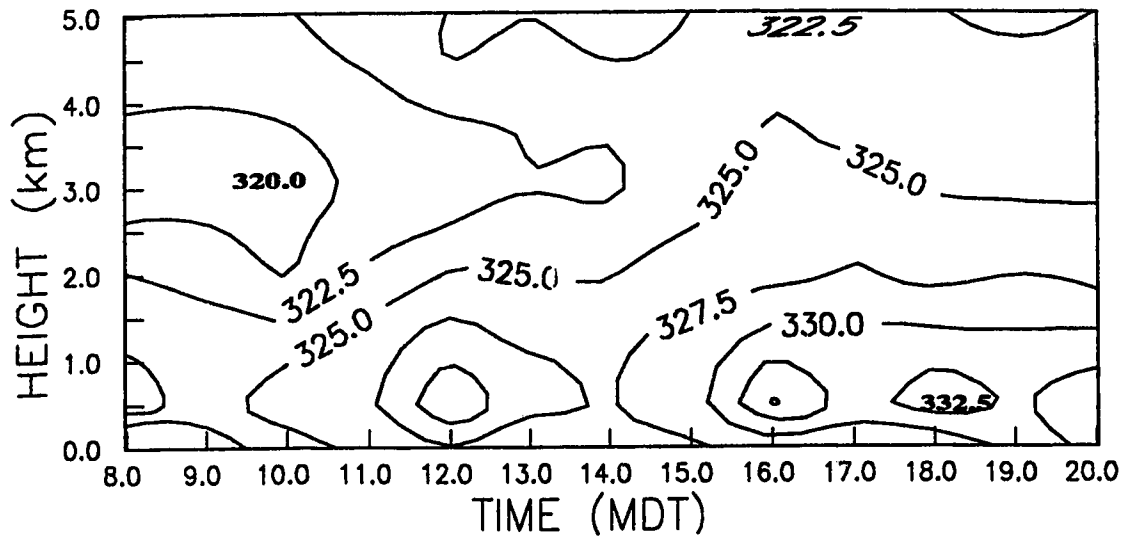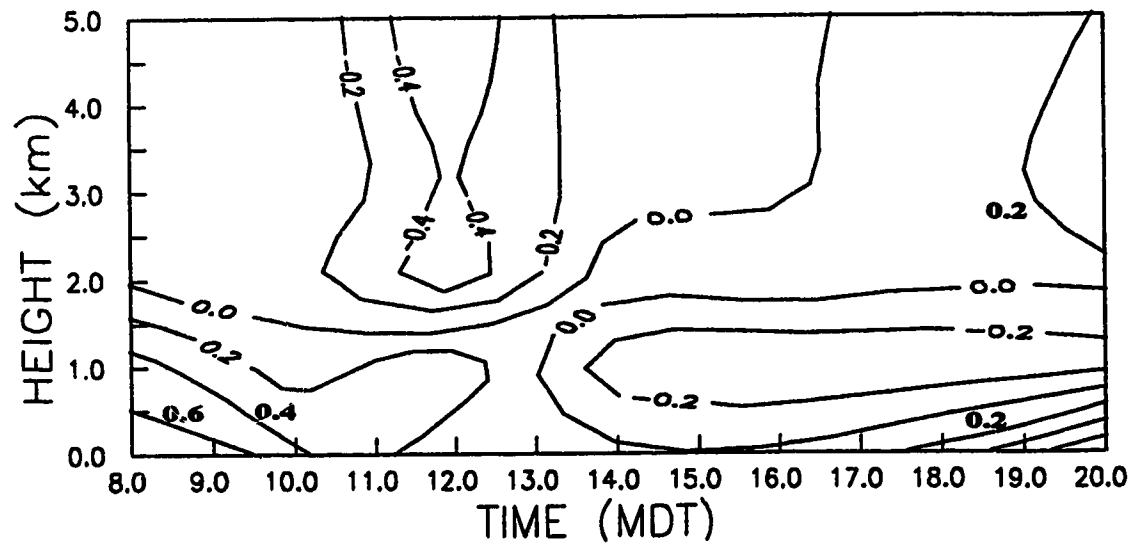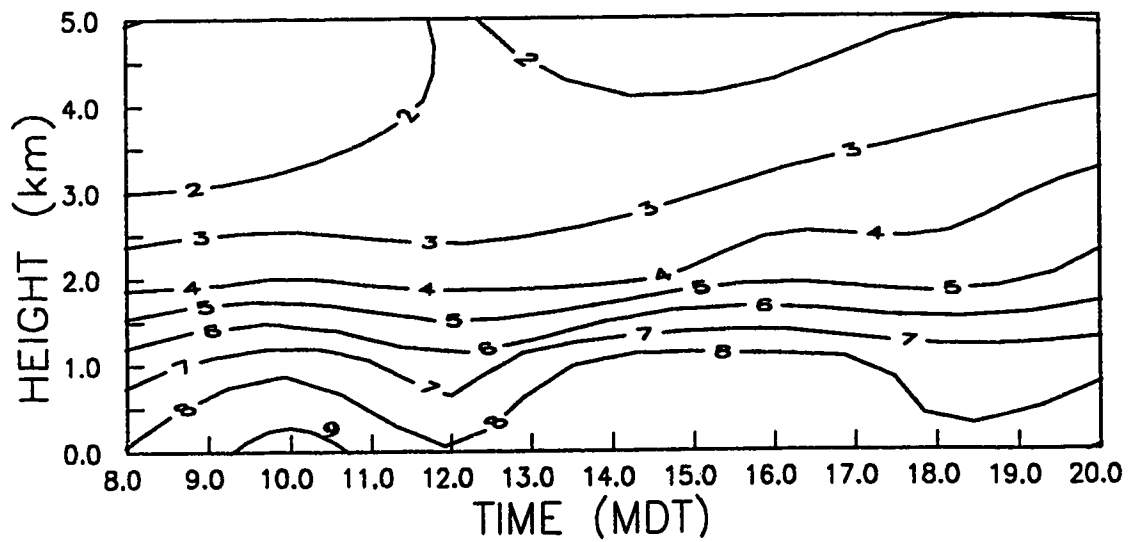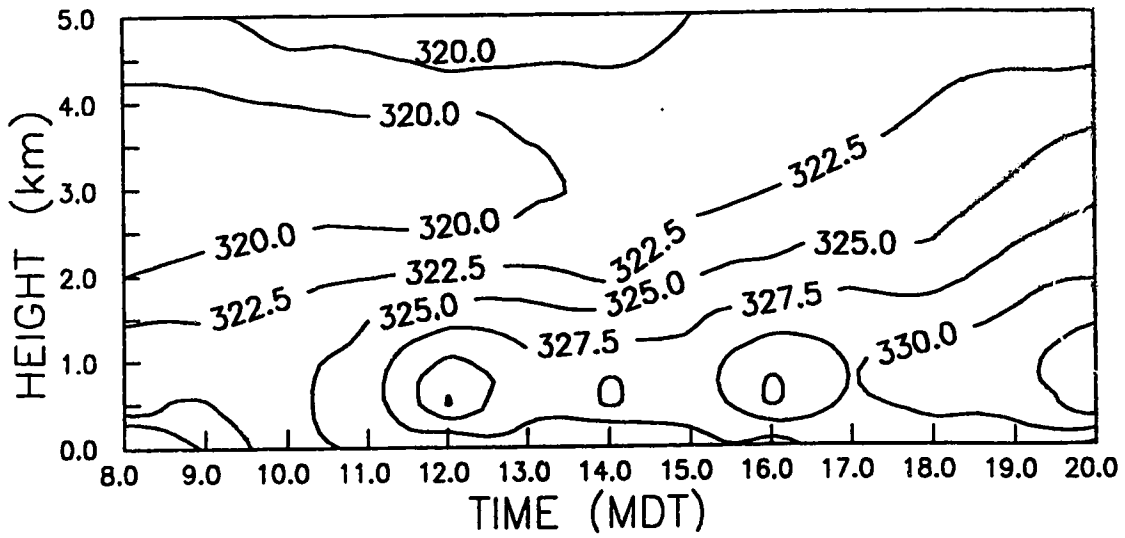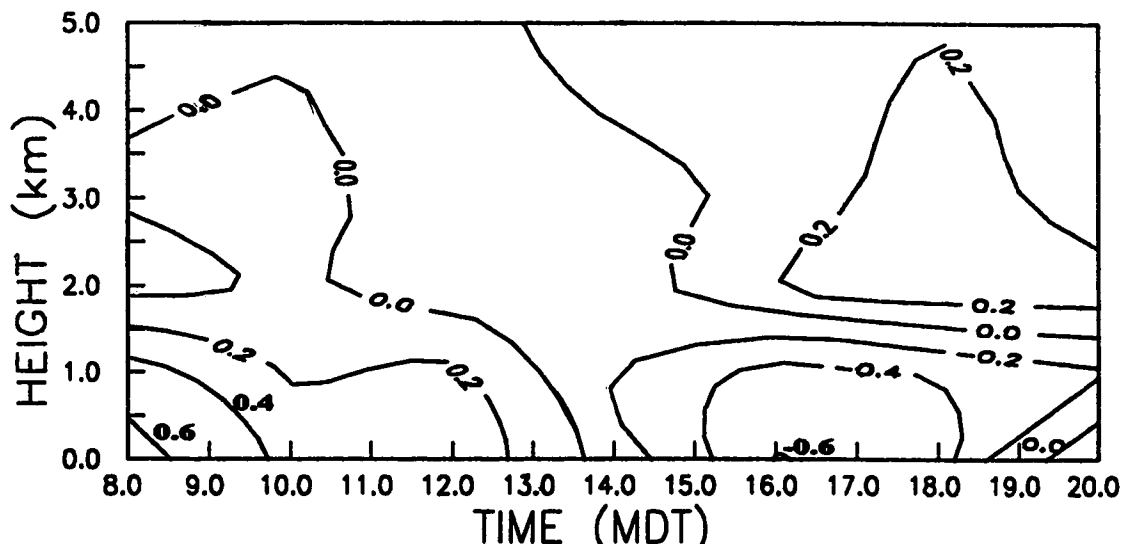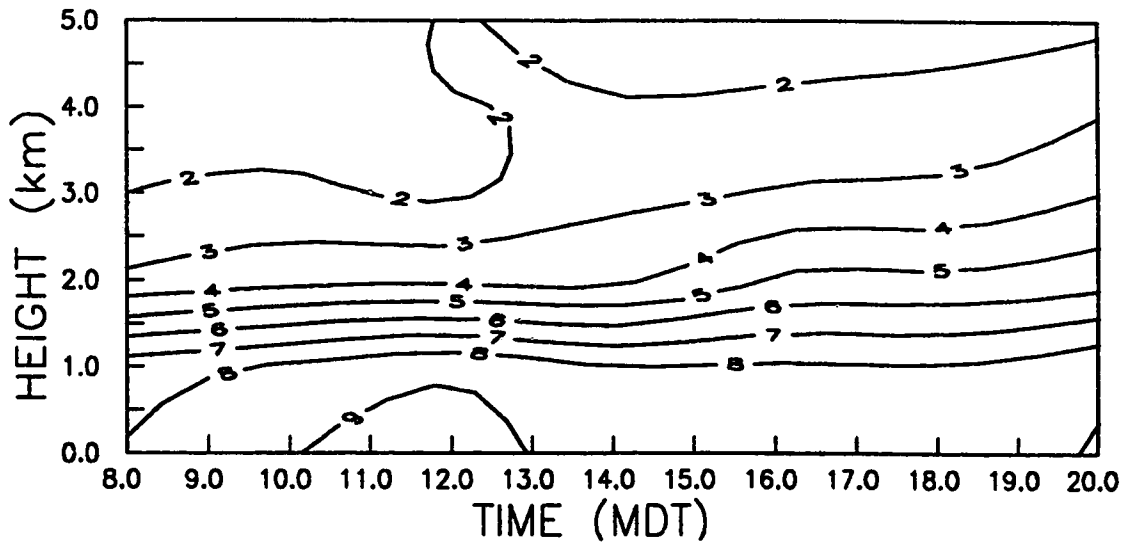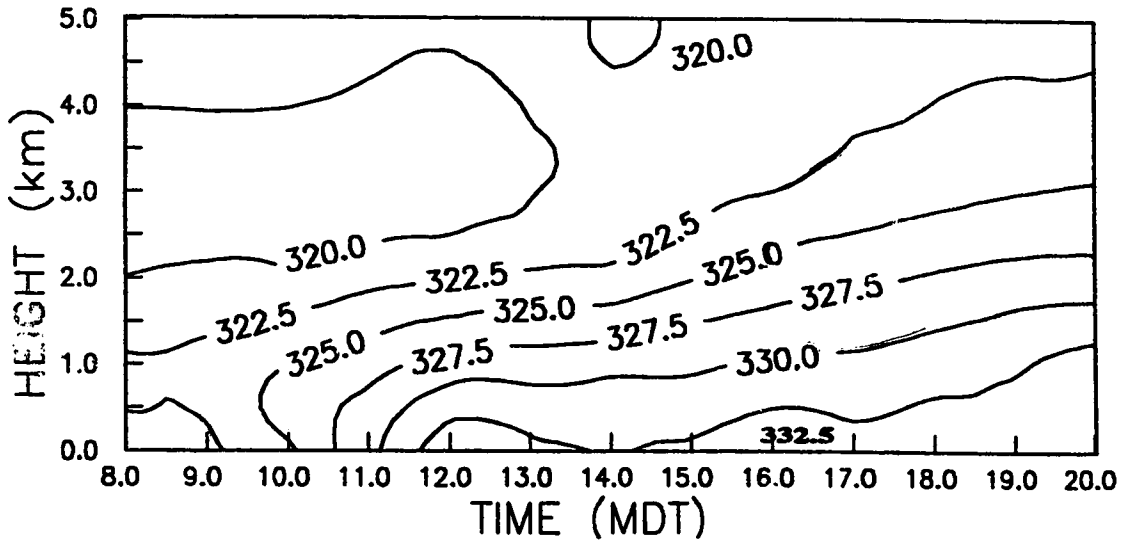
Figure 4.41. Time-height cross-section contours of equivalent potential temperature θe (degrees K), mixing ratio (g/kg), and moisture convergence (g/kg h) for the position of the LIMEX85 Storm K at 2200 UTC.
Note 12:00 MDT = 1800 UTC

moisture convergence at 12:00 MDT. The Storm B passed over this location at 12:00 MDT. Late afternoon mid-and upper-level regions show moisture divergence. Low-level and surface moisture convergence is evident for the entire period. Site Z has low- and mid-level moisture convergence until 13:00 MDT followed by divergence. There is a mid- and upper-level region of moisture convergence 0.3 (g (kg h)) at 18:00 MDT roughly coinciding with the time of Storm K development and passage over this location. Stations close to storm development have morning surface moisture convergence while stations removed from storms show maximal surface moisture convergence in the afternoon.

The analysis of the horizontal cross-sections allows the identification of existing boundary layer moisture pool, as well as the absence of a dry environment at the mid-levels. These findings are consistent with the typical convective storm model outlined in the literature review (page 5).

4.7   VERTICAL CROSS-SECTIONS ALONG A GRID LINE

The last set of moisture depictions are vertical cross-sections taken along an east-west line through the storm positions indicated by the radar data in the LIMEX85 region. These plots pertain to either Storm B (2000 UTC) near Rocky Mountain House or Storm K northwest of Red Deer (2200 UTC). Three times are depicted illustrating the pre-storm, storm and post-storm environments as summarized below in Table 4.2. Contours of mixing ratio, moisture convergence, equivalent potential temperature and the wind velocity components (u, v) are provided.

104

TABLE 4.2   Vertical cross-sections prepared for the LIMEX85 study region.

Storm Feature	Times Depicted (UTC)			Variables Depicted
	prior to	during	after	
STORM B	1400,	1800,	0200	r, MC, θe, u, v
STORM K	1400,	2200,	0200	r, MC, θe, u, v

Given a point of origin in the southwest corner of the LIMEX85 study area, Storm B is located at (85 km, 162.5 km) and Storm K is located at (170 km, 147.5 km).

Contours of mixing ratio (Figure 4.42) are very similar prior to both storms with the 6 g/kg contour extending from the surface up to the 800 mb level in the eastern half of the cross section (i.e., a tongue of moist air to the east).

For Storm B, the early morning pocket of low-level moisture to the east seems to be advected upward and intensifies as a mid-level moisture maximum to the west. During the storm mid-level values of 5 to 6 g/kg dominate. After the storms, even larger mid-level values occur suggesting the possibility of further convective outbreaks in these regions after the time periods covered here. Due to the lack of radar images for the time period around 0200 UTC, it is not clear if these values are associated with another early evening storm. After storm passage the low-level moisture content increases significantly. Some possible mechanisms to account for this include advection of moisture from the east near the surface, surface evaporation after rainfall, and the storage of moisture during the storm in cloud drops, rain drops as well as ice phase forms.

Contours of θe (Figure 4.43) prior to storm formation show maximum values at 850 mb near the storm formation position of Storm K, but not Storm B. These maximum regions fall to 900 mb during the storm passage and then return to a level of 850 mb after the storms. The early cross-sections show a warm, moist air mass from

105
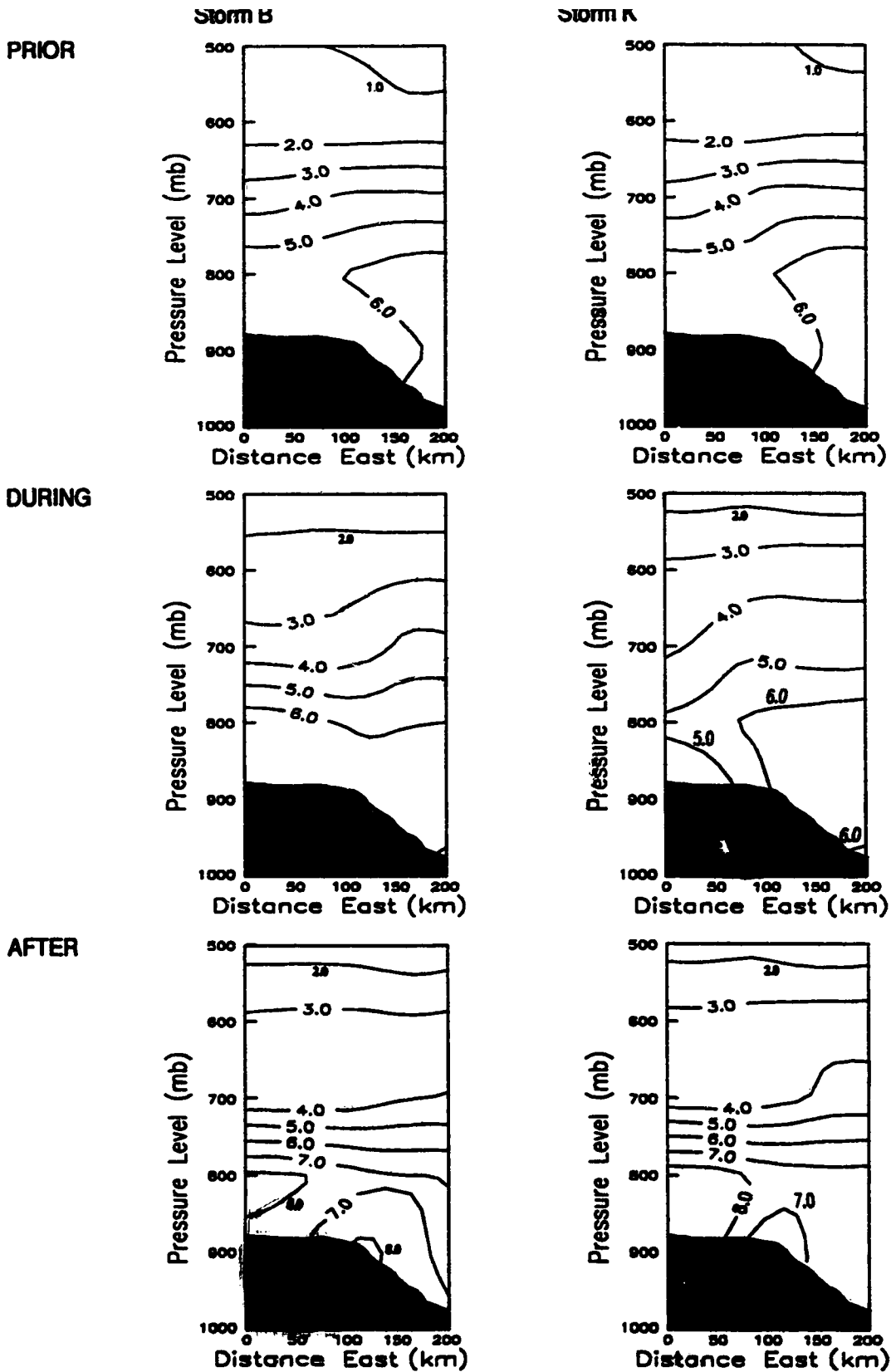
Figure 4.42. Contours of mixing ratio [g/kg] in an east-west vertical cross-section for two LIMEX85 storms, prior to, during, and after the storm passage.

Storm B   Storm K
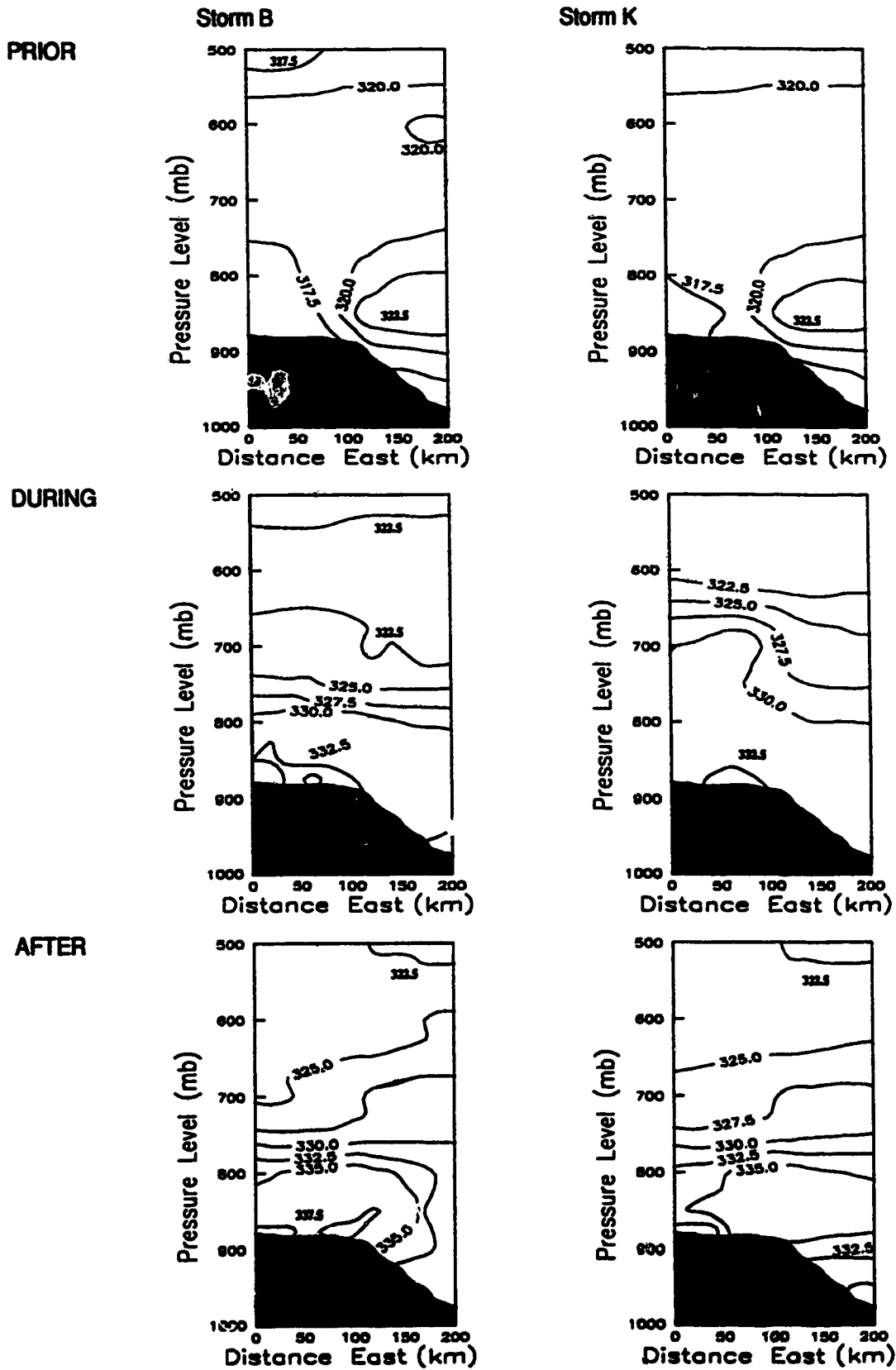
PRIOR

DURING

AFTER

Figure 4.43. Contours of equivalent potential temperature (degrees K) in an east-west vertical cross-section for two LIMEX85 storms, prior to, during, and after the storm passage.

the east pushing into the region. By storm time, the air masses have mixed and the earlier east-west gradient is replaced by a more homogeneous situation. Very tight vertical gradients occupy the 800 mb to 700 mb layer for Storm B during the after storm period. Storm K has tight vertical gradients between 600 and 700 mb during storm passage and tight vertical gradients between 700 and 900 mb after storm passage. This may also indicate the possibility of an early evening convective outbreak. Prior to both storms, the eastern lower-layers (1000 to 850 mb) are potentially stable while layers above 850 mb are potentially unstable ($\partial\theta e/\partial z < 0.0$). During the period of storm passage potential instability dominates the layers above 900 mb with values ranging from -3 °C/km near Storm K and -7 °C/km near Storm B. Both post-storm depictions indicate a return to low-level potential stability and potential instability above 850 mb.

Surface moisture convergence (Figure 4.44) occupies the east side of both cross-sections prior to storm development. By the time of storm passage, west side low and mid-level moisture convergence is evident. After storm passage, mid and low-level eastern moisture convergence remains, joined by upper-level regions of moisture divergence. Variable terrain makes the interpretation of surface moisture convergence difficult as a roughly flat surface is assumed.

The zonal wind components (U) (Figure 4.45) for both storms are very similar prior to storm development, with light westerly winds below 800 mb and moderate wind sheer above 800 mb. A review of the entire LIMEX85 data set showed that over 50% of the early surface wind field data were missing. Winds slightly above the surface which were not included in this analysis indicated a slight easterly component. Prior to the development of Storm K, the wind comes from the south east at about 5-10 ms⁻¹ with the easterly component at about 2 ms⁻¹. This may support the existence of a "plain breeze" (forced by differential heating in the plains and the Rocky foothills) hypothesized by Smith (1980). During storm passage, low wind speeds dominate the regions below 850 mb for Storm H and below 720 mb for Storm K. Early surface downslope flow is replaced by slight upslope flow during storm passage. Post storm surface flow returns to low downslope flow.
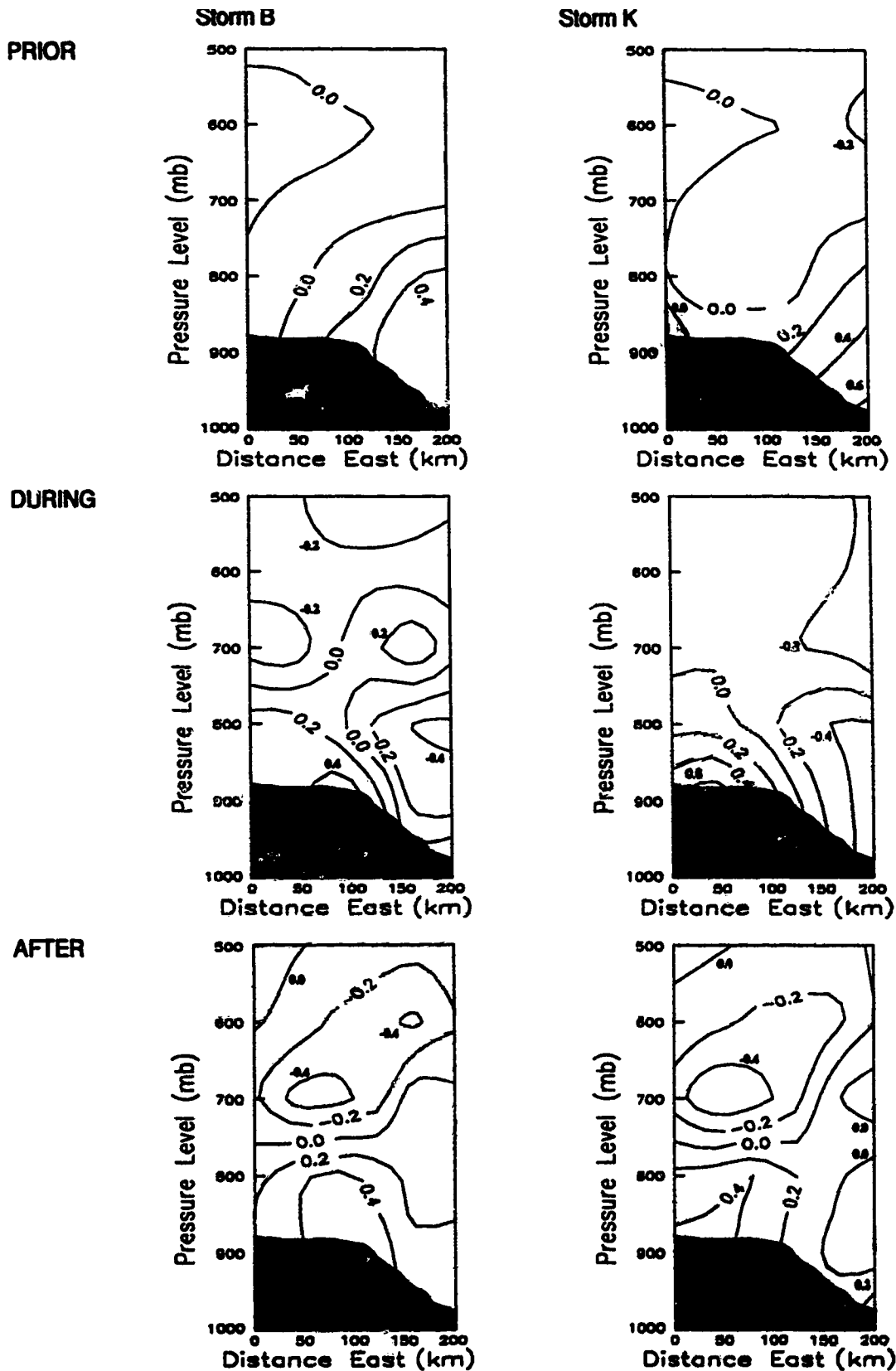
Figure 4.44. Contours of moisture convergence (g/kg h) in an east-west vertical cross-section for two LIMEX85 storms, prior to, during, and after the storm passage.
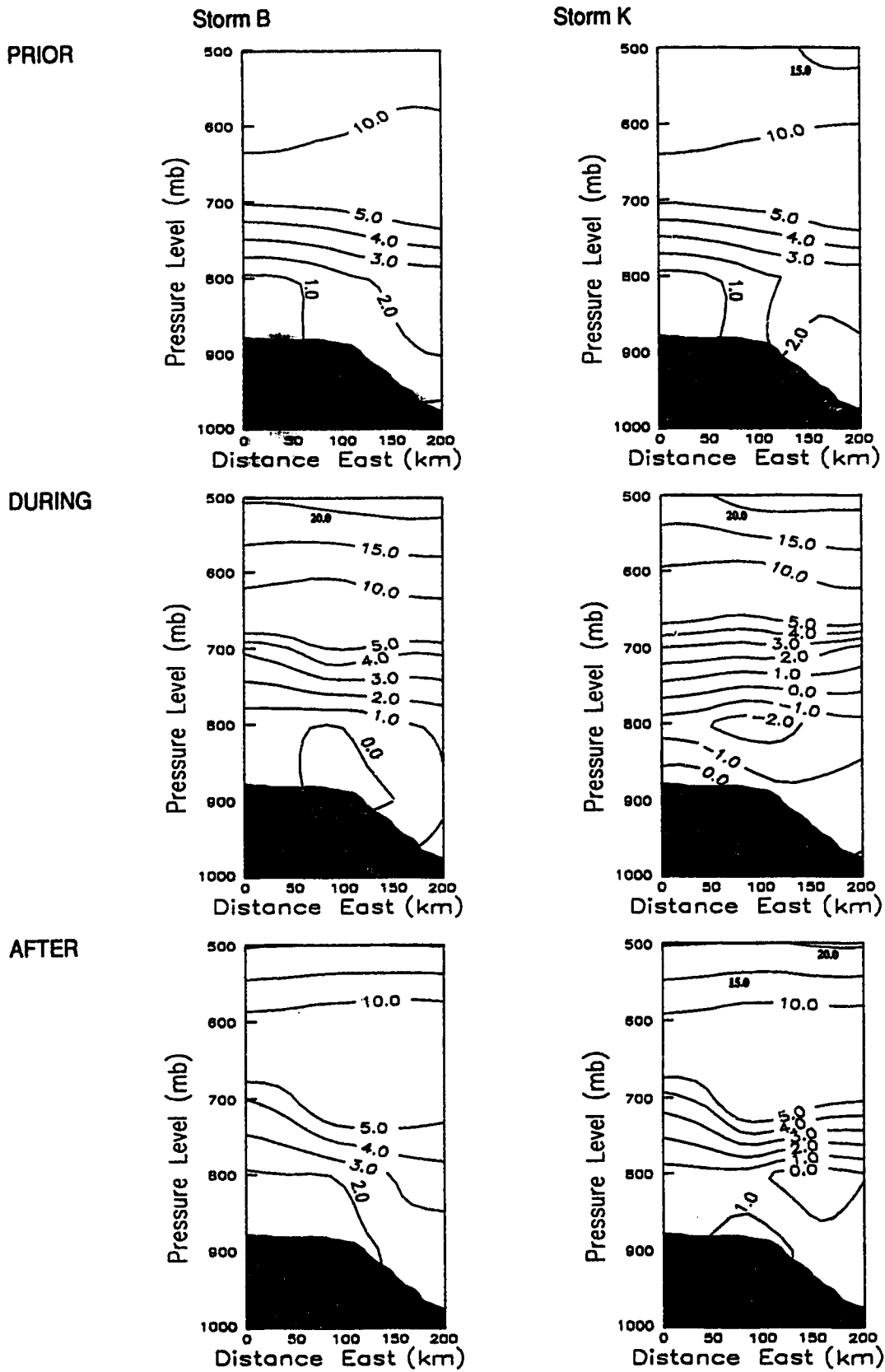
Figure 4.45. Contours of the zonal wind velocity component (m/s) in an east-west vertical cross-section for two LIMEX85 storms, prior to, during, and after the storm passage.

The meridional wind component (Figure 4.46) shows a southerly wind component dominating at all levels until storm passage when a flow from the north is evident in the eastern part of the cross-section for Storm K.

4.8   ERROR ANALYSIS

Every measurement has some uncertainty since it is not possible to measure any quantity exactly, due to the limits of precision, and calibration. These uncertainties cause further propagated error in analysis procedures. Errors take on two forms, systematic and random. Systematic errors include such things as observer biases, timing problems and poor calibration methodology. In general, systematic errors are difficult to quantify or eliminate and no statistical method exists to treat them. Normally, careful observation procedures and proper instrument maintenance/calibration can render systematic errors negligible when compared to random errors.

A quantitative estimate of random error is possible using statistically based methods such as those referenced in Squires (1968). These methods relate the error in a parameter to its variance. The standard error is assumed equal to the standard deviation or the square root of the variance.

Given that a parameter is a function of several variables we can combine the errors associated with each variable in a fashion based on the functional dependence to arrive at an error estimate for the parameter in question. The rules for the relation between standard errors are outlined in (Squires, 1968) Use of these methods requires the data in question to exhibit a normal or near normal distribution. Normally distributed data sets have specific higher moments (skewness and kurtosis) measures of 0.0 and 3.0. As perfectly normal distributions are rare, an arbitrary window of acceptable skewness and kurtosis values was set. For skewness, an acceptable range of -1.0 to +1.0 was selected. For kurtosis, an acceptable range of +2.0 to +4.0 was selected. Sample
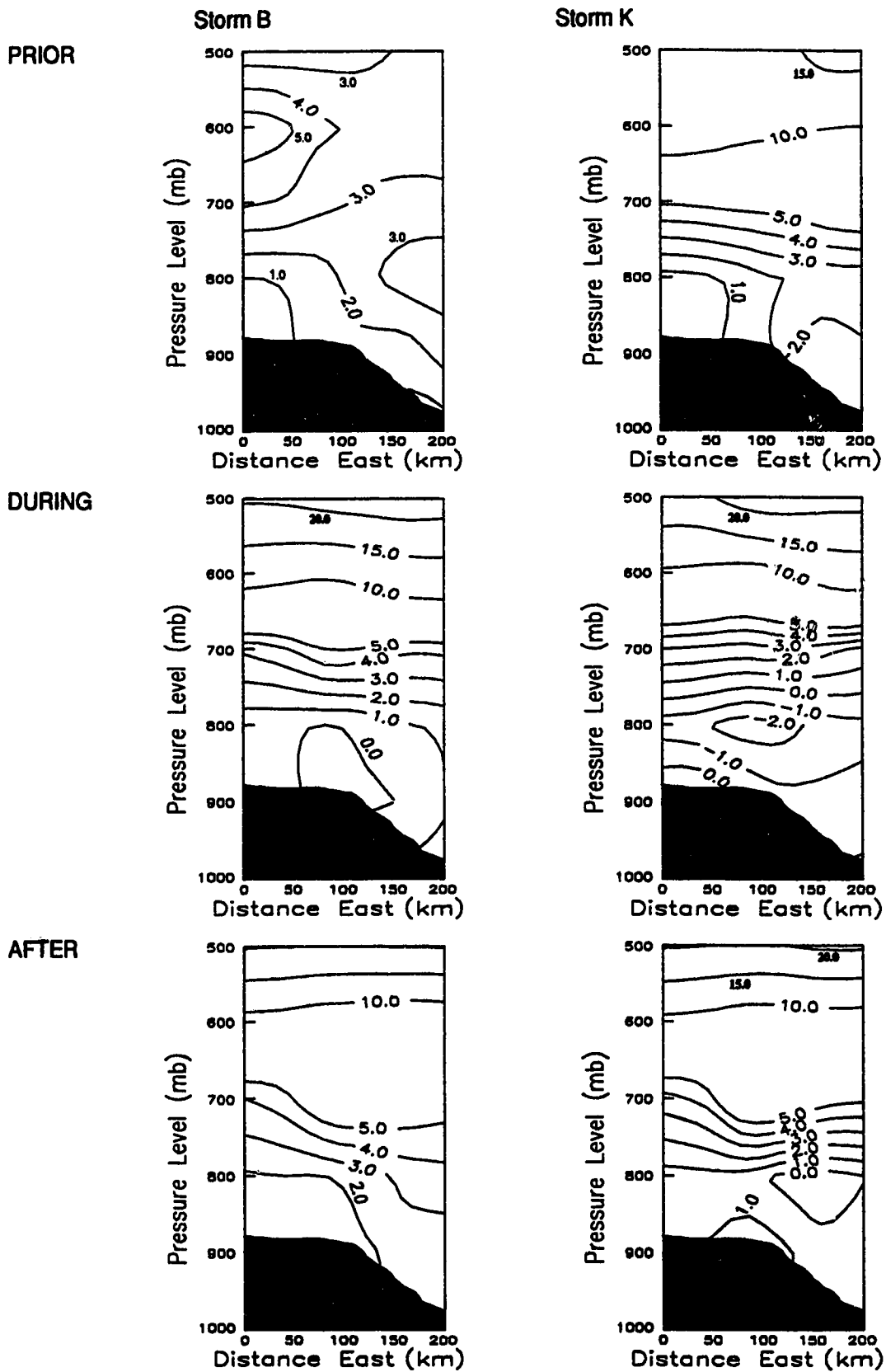
Figure 4.46. Contours of the meridional wind velocity component (m/s) in an east-west vertical cross-section for two LIMEX85 storms, prior to, during, and after the storm passage.

skewness and kurtosis values calculated for all variables used in the analysis are presented in Table 4.3.

TABLE 4.3   Sample skewness and kurtosis values for parameters used in the analysis.

Parameter	Skewness	Kurtosis
Mixing Ratio	-0.2	-0.6
Wind Speed	1.8	3.1
Wind Direction	-0.5	-1.0
Pressure	-1.1	-0.2
Temperature	-1.1	0.4
Dew Point Temperature	-1.4	1.3
U-wind Component	1.5	2.4
V-wind Component	0.5	0.6
Equivalent Potential Temperature	-0.1	0.0

None of the parameters meet the near-normal criteria. Another test of the normal distribution is the goodness-of-fit Kolmogorov-Smirnov test (Steele and Torrie, 1980). This test compares the theoretical cumulative distribution function with the sample cumulative distribution function. The statistic used to measure the difference is:

$$D = \max \; |CDF_{ob}(X)_i - CDF_{th}(X)_i| \qquad (4.2)$$

where: i ranges from 1 to N and N is the number of observations used to define the cumulative distribution function.

If the calculated D value is lower than the table D value for some p significance value (P usually = 0.05) and a known number of data points exist in the population, we can accept the distribution as normal. The value P is known as the probability of committing an error in the test, and is referred to as the level of significance of the test.

This test was applied to the same parameters as in Table 4.3 with the results presented in Table 4.4.

TABLE 4.4   Kolomogorov - Smirnov test statistic D values for parameters used in the analysis.

Parameter	Calculated D Value	Table D Value (P = 0.05)
Mixing Ratio	0.088	0.238
Wind Speed	0.280	0.271
Wind Direction	0.178	0.221
Pressure	0.503	0.225
Temperature	0.211	0.225
Dew Point Temperature	0.200	0.238
U-wind Component	0.160	0.247
V-wind Component	0.090	0.265
Equivalent Potential Temperature	0.249	0.238

Using this test, one can accept mixing ratio, wind direction, temperature, dew point temperature, and the wind velocity components as exhibiting normal distributions.

Each of our chosen moisture parameters are functions of several basic meteorological data:

$$r = f(t_d, p) \qquad (4.3)$$

$$\theta e = f(t, p, r) \qquad (4.4)$$

$$MC = f(r, u, v) \qquad (4.5)$$

$$IMC = f(p, r, u, v) \qquad (4.6)$$

In order to use the statistical method of calculating the error induced in the calculation of a moisture parameter, all of the basic meteorological precursors should exhibit

114

normal distributions. Since this is not the case, a different approach will be used to estimate the errors incurred by analysis.

Each basic meteorological variable used in this analysis is associated with a instrument uncertainty. Table 4.5 shows the largest expected measurement uncertainty associated with each parameter based on values cited by Strong (1986) and Sackiw (1986).

TABLE 4.5   Worst case measurement uncertainties for four parameters.

Parameter	Worst-case Measurement Uncertainty
Pressure	± 3 mb
Temperature	± 0.5°C
Wind Speed	± 0.5 m/s
Wind Direction	± 2°
Geographic Position	± 2 km

These worst-case uncertainties were propagated through the calculation process of the moisture measures and the gridding procedure. This was done for the full range of each basic meteorological parameter. An outline of this error estimation procedure is given below using mixing ratio as an example:

$$\text{Mixing ratio } r = 0.622 \, (e_w/(p - e_w)) \tag{4.7}$$

where e_w was calculated using (Lowe, 1976) polynomial formulation:

$$e_w = a_0 + t_d \, (a_1 + t_d \, (a_2 + t_d \, (a_3 + t_d \, (a_4 + t_d \, (a_5 + t_d \, (a_6)))))) \tag{4.8}$$

where: the values of $(a_0, a_1, a_2, a_3, a_4, a_5, a_6)$ can be found in Section 1.3.

115

Mixing ratio values were calculated for pressure values from 500 to 1050 mb in 25 mb increments and for dew point temperature values ranging from 250 to 310 K in steps of 3 K. These calculations were then repeated with every incidence of p replaced by p + Dp and p-Dp, and all incidences of t_d replaced by $(t_d + Dt_d)$ and $(t_d - Dt_d)$. The values of Dp and Dt_d were 3 mb and 0.5°C as referenced in Table 4.5. The differences between the paired results were collected and the largest and mean, and percentage differences retained at the end. The differences were sorted as the largest, mean, and percentage errors incurred by the analysis or calculation procedure. The resulting errors with the highest magnitude average, and percentage errors are tabulated in Table 4.6.

TABLE 4.6   Highest, average and percentage errors incurred by analysis or calculation procedures.

Calculation	Highest Error	Percentage of data Range	Average Error	Percentage of data Range
Mixing Ratio (g/kg)	1.53	10.8	0.25	1.8
Equivalent Potential Temperature (K)	5.0	7.4	1.24	1.8
Moisture Convergence (g/kg h)	0.14	6.3	0.07	4.7
Integrated Moisture Convergence (mb g/kg h)	52.6	20.4	25.1	10.0
1/d² Weighted Gridding Process Using 10 Nearest Neighbours*	3.1	N/A	2.57	N/A

* Percentage highest error and percentage average error.

Using the average error values as an error estimate, the minimum contour intervals for mixing ratio, moisture convergence, integrated moisture convergence and equivalent potential temperature are 0.5 g/kg, 0.15 g/kg h, 50 mb g/kg h, and 2.5 °C, respectively (Sharp, 1987).

CHAPTER 5.

CONCLUSIONS

5.0   SUMMARY

An analysis of the LIMEX85 data set was performed in order to characterize the temporal evolution of the moisture fields and to relate the moisture fields to observed thunderstorms. The moisture fields of mixing ratio, equivalent potential temperature, moisture convergence, and integrated moisture convergence were contoured on horizontal and vertical planes in order to depict their evolution in time and space. These contoured fields were then linked to the observed storms as indicated by radar images. The gridding procedure was tested and an error analysis for the computational methods was performed. The findings for each section of the analysis are summarized in the following section.

5.1   CONCLUSIONS

The surface stations near the positions of storm formation or over which storms passed show a well defined capping lid which lasts two to four hours longer than the normal morning inversion. These stations also exhibit cooling above the boundary layer. The LCL's at stations near storm formation or passage are significantly lower than those not associated with convective storm events. Convective storm development was observed on radar after the breakdown of the capping inversion.

Horizontal fields of surface mixing ratio show a moist tongue of surface moisture which expands over central Alberta from the east and southeast. This is spatially associated with the regions which show evidence of convective thunderstorm activity in central and south central Alberta. This pool of moisture satisfies the first condition of

117

thunderstorm formation, namely that there be a source of surface moisture. The highest mixing ratio values are spatially coincident with regions of storm development in both the Alberta and LIMEX85 study areas. Mid-level mixing ratios (800 - 650 mb) are consistently 3 to 4 g/kg providing sufficient moisture to counteract the inhibiting effect of cloud erosion by entrainment of ambient air into the cloud.

The source of surface moisture is accompanied by high surface θ_e values which reveal centres of potential instability in the same regions where storm development is evident based on radar imagery. The largest surface θ_e values occur south of the large storms observed. Within the LIMEX85 study area, the highest surface θ_e values occur in regions where convective storm development is evident. This instability along with relatively low LCL's tends to satisfy the second requirement of storm formation, a source of vertical lift to transport the boundary layer moisture upwards. The stratification of θ_e values indicates the existence of a state of conditional convective instability which favours storm development.

Moisture convergence tends to precede regions of storm development by two to four hours. This holds true for both the Alberta and the LIMEX85 analysis. Moisture convergence was observed during periods of storm formation below 750 mb. Upper levels were characterized by moisture divergence.

Upper-air horizontal fields of mixing ratio on isobaric surfaces show increases of atmospheric moisture prior to the times of storm development. However, the relationship between regions of maximum moisture and storm development or passage is less clear than at that the surface. This diminished spatial relationship is also evident in the upper air θ_e fields. Moisture convergence contours exhibit a stronger spatial relationship with the locations of storm growth or passage. Integrated moisture convergence contours showed very high values over the region which spawned Storm B, but had negative values at the formation time and position of Storms H and K.

Time-height cross-sections of θ_e at a particular location reveal larger negative $\partial\theta_e/\partial z$ gradients for stations representative of storm formation or passage. The mixing ratio is

118

generally higher at the surface during the late morning and early afternoon for these stations. In two-thirds of the storm cases an upper-level increase in mixing ratio is evident at mid-day. One-third of the storm cases show a marked increase in moisture convergence at mid and upper levels prior to storm formation. No upper-level increases in moisture are apparent for stations removed from storm development. Early morning surface moisture convergence is evident for stations near convective storms. Stations removed from the storms show maximal surface moisture convergence in the mid-afternoon.

Vertical cross-sections along an east-west parallel indicate high negative equivalent potential temperature gradients (< -3 °C/km) near the time of storm formation. Low-level moisture convergence before storm formation is followed by mid-level moisture convergence at the time of storm formation. Moisture flux and budget calculations indicate a net loss of moisture at all analysis times in the LIMEX85 study area. This supports the lack of any large storms observed forming in the region. The storms affect the ambient environment by significantly moistening the lower troposphere as they pass. Increases of mixing ratio up to 1.5 g/kg below 700 mb were observed in regions where storms passed.

The observed thunderstorm paths as determined by radar pass through regions with surface moisture sources, mid- and upper-level moisture convergence and high values of surface θ_e. Thus, the known requirements of thunderstorm formation and evolution as given by (Rogers, 1979) and (Cotton, 1990) are supported by the present analysis. The mesoscale analysis resolution is essential in order to delineate the moisture transport features associated with thunderstorm development and growth.

The average errors resulting from measurement uncertainty and the formulations of each moisture parameter represent a small percentage of the data ranges (2 to 10%).

6.   BIBLIOGRAPHY

Barry, R.G., and R.J. Chorley, 1974: Atmosphere, weather and climate. Methuen and
Company Ltd. Pub. Co., London, 379 pp.

Braham, R.R. Jr., 1952: The water and energy budgets of the thunderstorm and their
relation to thunderstorm development. Journal of Meteorology, 9, 227-242.

Brennand, M. and J.W. Mason, 1986: LIMEX85 automated surface data description.
Alberta Research Council Internal Report, 5pp.

Carlson, T. N., S. G. Benjamin, G. S. Forbes, and Y.F. Li, 1983: Elevated mixed layers
in the regional severe storm environment: conceptual model and case studies. Monthly
Weather Review, 111, 1453-1473

Carlson, T.N, 1982: The role of the lid in severe storm formation: Some synoptic
examples from Sesame. Proceedings of the 12th conference on Severe Local Storms
Conference, San Antonio Texas, Jan 11 - 15 1982, 221-224

Cotton, W.R., 1990: Storms. *ASTeR Press Pub. Co., Fort Collins, Colorado, 158 pp.

Foote, G.B. and J.C. Fankhauser, 1973: Airflow and moisture budget beneath a northeast
Colorado hailstorm, Journal of Applied Meteorology, 12, 1330-1353

Fuelberg, H.E. and M.F. Printy, 1983: Meso ß-Scale Thunderstorm/Environment
Interactions During AVE-SESAME V (20-21 May 1979). Journal of the American
Meteorology Society, Vol. 64, 1144-1155.

Fuelberg, H.E., Lin, Y. and H. Chang, 1986: A Moisture Analysis of the Meso ß-Scale
Thunderstorm Environment during AVE-SESAME V (20-21 May 1979). Monthly
Weather Review, 144, 534-545.

Haltiner, G.J., 1971: Numerical weather prediction. John Wiley and Sons Pub. Co., New York, 317pp.

Harbaug, J.W., Doveton, J.H. and J.C. Davis, 1977: Probability methods in oil exploration, John Wiley and Son Pub., New York, 254 pp.

Heimbach, J.A. and T.M. Engel, 1987: The Use of Limited Surface networks to Measure Mesoscale Phenomena. Monthly Weather Review, 115, 118-128.

Holton, J.R., 1979: An Introduction to Dynamic Meteorology. Academic Press Pub. Co., New York, 391 pp.

Honch, R., 1989: Mesoscale vertical velocity: A case study. Unpublished M.Sc. Thesis, University of Alberta, Edmonton, Alberta, 110 pp.

Honch, R.W. and G.S. Strong, 1990: Mesoscale vertical velocity and surface convergence fields in the lee of the Alberta Rockies: A Case Study. Proceedings of the 3rd Workshop of operational Meteorology, May 2 - 4, 1990, Montreal. 6 pp.

Hudson, H.R., 1971: On the relationship between horizontal moisture convergence and convective cloud formation. Journal of Applied Meteorology, 10, 755-762

Huschke, R.E., ed., 1970: Glossary of Meteorology, American Meteorological Society Pub., Boston, 638 pp.

Iribarne, J.V., and W.L. Godson, 1981: Atmospheric thermodynamics. Second Edition. D. Reidel Pub. Co., Boston, 259 pp.

Kuo, Y. and R.A. Anthes, 1984: Mesoscale Budgets of Heat and Moisture in a Convective System over the Central United States. Monthly Weather Review, 112, 1482-1496.

Lowe, P.R., 1976: An approximating polynomial for the computation of saturation vapor pressure, Journal of Applied Meteorology, 16, 100-103.

Maddox, R.A., 1983: Large-scale meteorological conditions associated with midlatitude, mesoscale convective complexes. Monthly weather review, 111, 1475-1493.

Mahrt L., 1977: Influence of low-level environment on severity of high plains moist convection. Monthly Weather Review, 105, 1315.

McCorcle, M.D., 1988: Simulation of Surface-moisture Effects on the Great Plains Low-Level Jet. Monthly Weather Review, 116, 1705-1720.

Modahl, A.C., 1979: Low-level wind and moisture variations preceding and following hailstorms in northeast Colorado. Monthly weather review, 107, 442-450.

Moore, J.T. 1982: The forcing and evolution of the three dimensional moisture convergence during the 10-11 April 1979 severe weather outbreak. Proceedings of the 12th Conference on Severe Local Storms, San Antonio Texas, Jan 11-15, 1982, 221-224.

Park, S. and D.N. Sikdar, 1977: Influence of low-level environment on severity of high plains moist convection. Monthly weather review, 105, 1315-1329.

Park, S. and D.N. Sikdar, 1982: Evolution of the dynamics and thermodynamics of a mesoscale convective system: A case study. Monthly Weather Review, 110, 1024-1040.

Rogers, R.R. and N.K. Sikellarion, 1986: Precipitation Production in Three Alberta Thunderstorms. Atmosphere-Ocean, 24, 145-168.

Rogers, R.R., 1979: A short course in cloud physics. Pergamon Press Pub. Co., New York, 235 pp.

Sackiw C.M., 1986: Examination of upper air data resolution using stability indices. Unpublished M.Sc. Thesis, University of Alberta, Edmonton, Alberta, 82 pp.

Sharp, W.E., 1987: Two basic rules for valid contouring. GeoByte Magazine, 2(4), 11-15.

Sikdar, D.N. and D. Fox., 1983: An evolving severe storm complex during sesame: Its large scale environment and momentum budget. Proceedings of the American Meteorological Society, 13th Conference, Tulsa Oklahoma, Oct. 17-20, 1983, 3121-315.

Smith, S.B. and M.K. Yau, 1987: The Mesoscale effect of Topography on the Genesis of Alberta Hailstorms. Beitr. Phys. Atmosph., 60,3, 371-392.

Smith, S.B., and Y.K. Yau, 1991: The roles of mountain-plain and synoptic circulations in the initiation of severe convective outbreaks in Alberta. Paper to be presented at the 5th conference on mesoscale processes, Jan. 5 - 10, 1992, Atlanta, George. 6 pp.

Squires, G.L., 1968: Practical physics. McGraw-Hill Pub. Co., London, 224 pp.

Steel, G.R., and J.H. Torrie, 1980: Principles and procedures of statistics: A biomedical approach. McGraw-Hill Book Pub. Co., New York, 633 pp.

Strong, G.S., 1974: The objective measurement of Alberta hailfall. M.Sc. Thesis, University of Alberta, Edmonton, Alberta, 182 pp.

Strong, G.S., 1986: Synoptic to mesoscale dynamics of severe thunderstorm environments: A diagnostic study with forecasting applications. Unpublished Ph.D. Thesis, University of Alberta, Edmonton, Alberta, 345 pp.

Strong, G.S., 1989: LIMEX85: 1. Processing of data sets from an Alberta mesoscale upper air experiment. Climatological Bulletin, 23(3), 98-118.

Surfer Version 4 Manual, 1989: Golden Software Inc. Pub. Co., Golden, Colorado, 310 pp.

Wenst, R.C., ed., 1968: Handbook of Chemistry and Physics, Chemical Rubber Company Pub., Cleveland, 2074 pp.

7. APPENDICES

APPENDIX I GRIDDING METHODOLOGY SENSITIVITY TESTS

In order to evaluate the effect of gridding interval choices , a series of sensitivity tests were performed. The gridding procedure is an interpolation/extrapolation of input data to a predefined grid of output data points. This procedure requires the user to make choices concerning the procedure. The main choice is to define the boundaries of the output grid and the number of x and y grid intervals. The following tests seek to reveal the effect of choosing different values of the gridding intervals. They are meant to simulate the case when the error in the input data is near zero. A second set of sensitivity tests follow which address as the effect of input errors on the gridding procedure. A specific function of the X and Y coordinates predetermined the contoured Z values.

The function $Z = \cos(X) \cos(Y)$ was selected with: (A.1)

$$\pi \leq X \leq 3\pi$$
$$\pi/2 \leq Y \leq 5\pi/2$$
X and Y increments of $\pi/10$.

The values of X, Y and Z were calculated to double precision (16 digits pass the decimal) to form an approximately error-fee input data set. The input data set has been offset by $\pi/8$ in order to keep the input data set from exactly overlapping the post-gridding output data set. This data set was gridded using the following cases in order to delineate the effect of choice of the grid interval:

- 200 increments of X and Y, $1/d^2$ interpolation, 10 nearest neighbours, $\Delta X = \Delta Y = \pi/10$ (Figure A.1)

- 100 increments of X and Y, $1/d^2$ interpolation, 10 nearest neighbours, $\Delta X = \Delta Y = \pi/10$ (Figure A.2)

125

- 50 increments of X and Y, $1/d^2$ interpolation, 10 nearest neighbours, $\Delta X = \Delta Y = \pi/10$ (Figure A.3)

- 25 increments of X and Y, $1/d^2$ interpolation, 10 nearest neighbours, $\Delta X = \Delta Y = \pi/10$ (Figure A.4)

- 10 increments of X and Y, $1/d^2$ interpolation, 10 nearest neighbours, $\Delta X = \Delta Y = \pi/10$ (Figure A.5)

Figure A.1 reveals the best representation of the function $Z = \cos(X) \cdot \cos(Y)$ with 200 intervals of x and y. Figure A.2 shows the function with 100 grids intervals. Although the overall representation is similar, the regions with very abrupt changes in contour path are less accurately portrayed. The same regions are poorly depicted in the 50 grid interval case as in Figure A.3. Further deterioration of regions with sharp contour redirection is further shown in Figure A.4 where the grid interval is 25. When using 10 grid intervals as shown in Figure A.5, the whole picture is deteriorated to the point where circular shapes are now shown in diamond-like features.

In order to resolve a field of data by using a contour map, the size of intervals used in the gridding procedure should be less than the average input data spacing. If the resulting field has regions of strong gradients (resulting in sharp contour directional changes) a larger number of gridding intervals should be used in order to more fully resolve the field. These conclusions assume the input data to be error free, which is usually not the case.
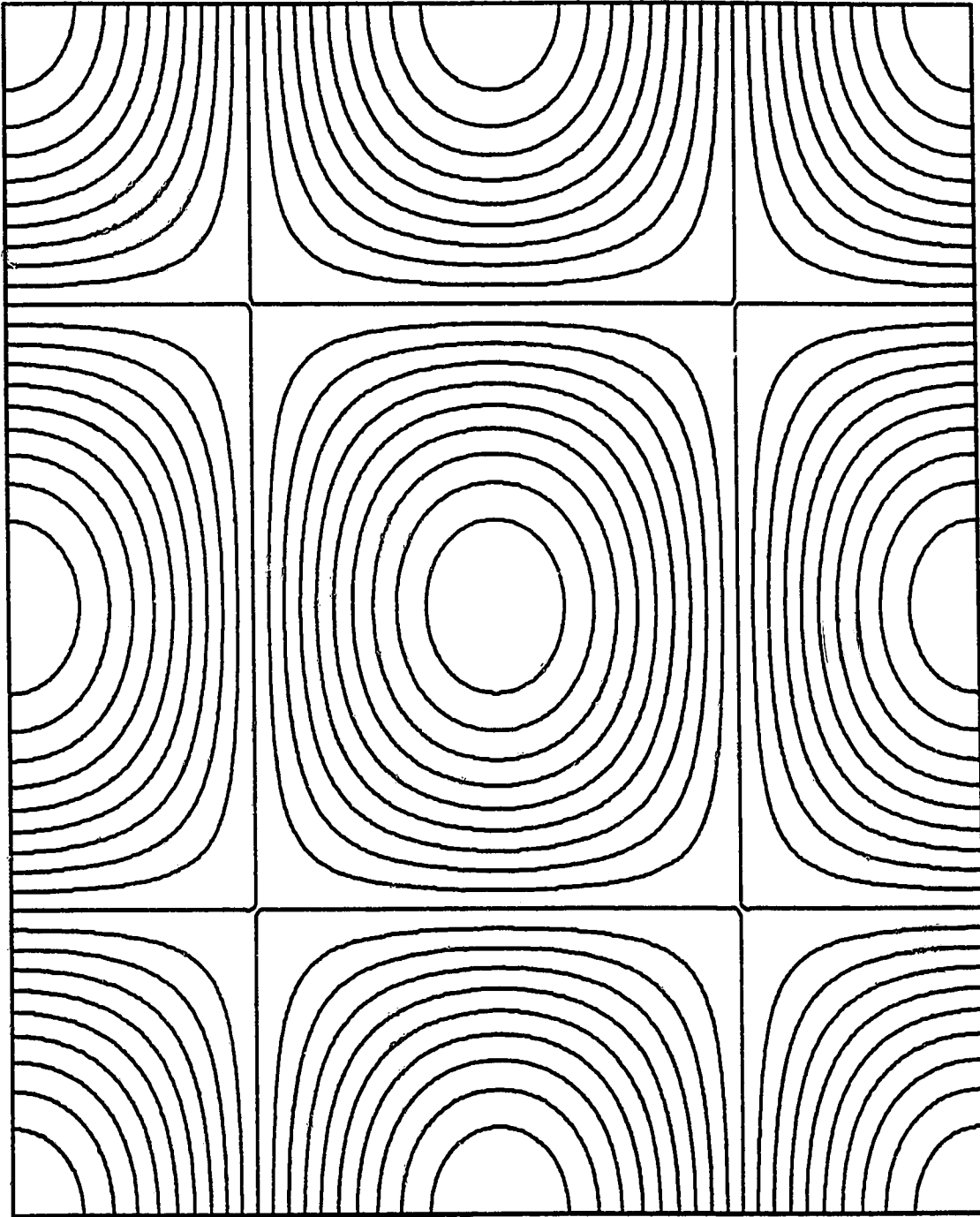
Figure A.1 Contours of Z = COS(x)*COS(y) using 200 grid lines in the X and Y planes.

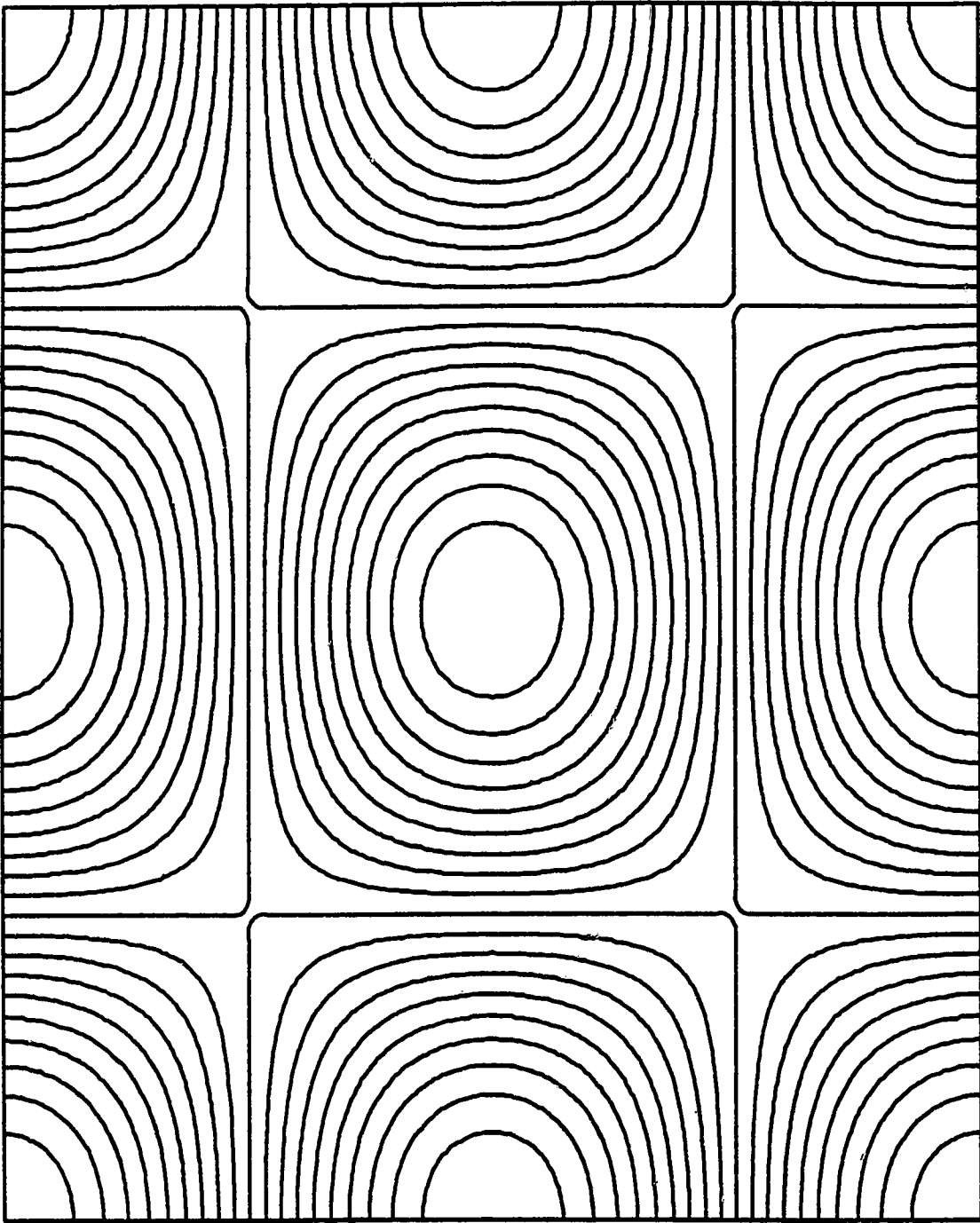Figure A.2 Contours of Z = COS(x)*COS(y) using 100 grid lines in the X and Y planes.

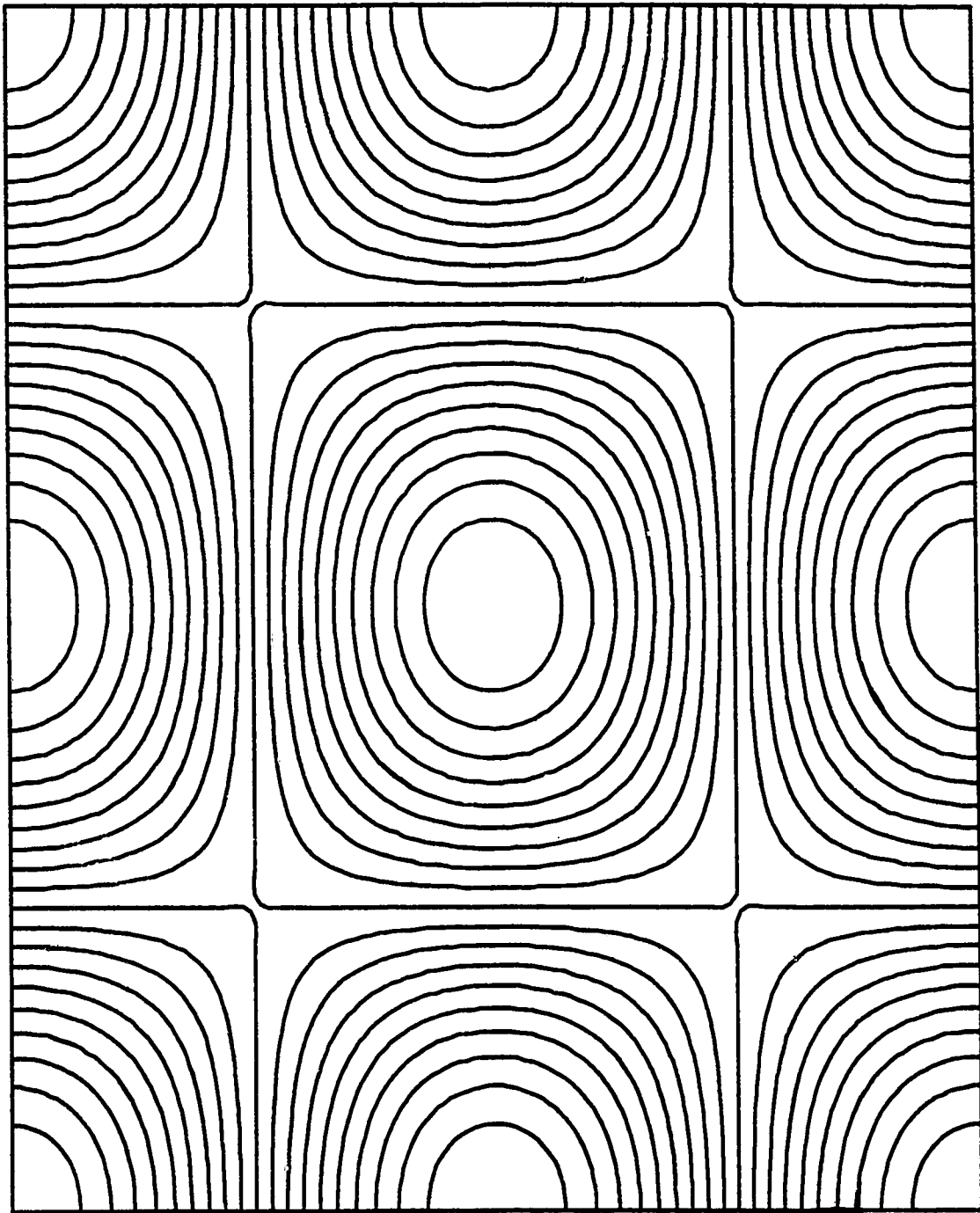Figure A.3 Contours of Z = COS(x)*COS(y) using 50 grid lines in the X and Y planes.

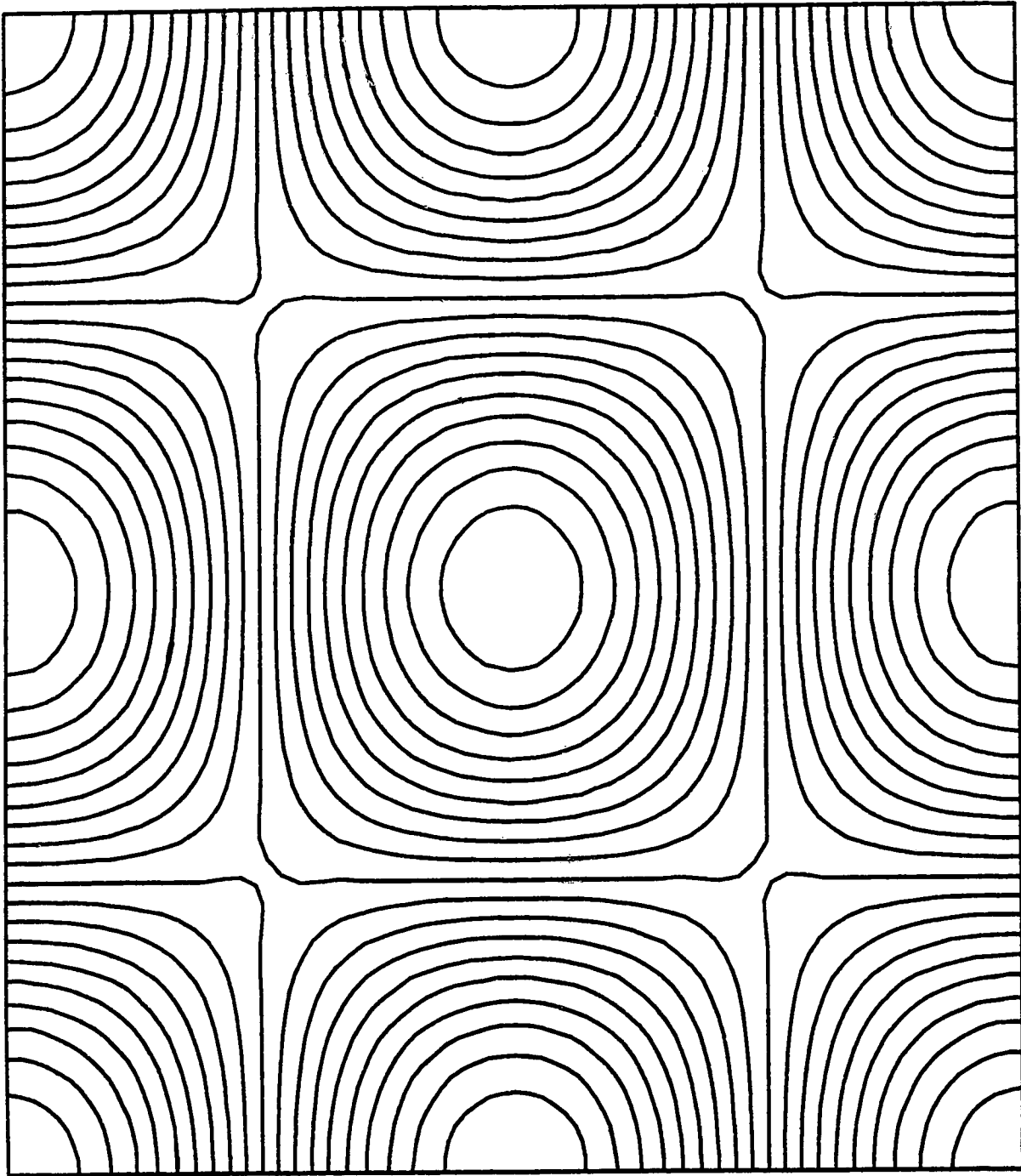Figure A.4 Contours of Z = COS(x)*COS(y) using 25 grid lines in the X and Y planes.

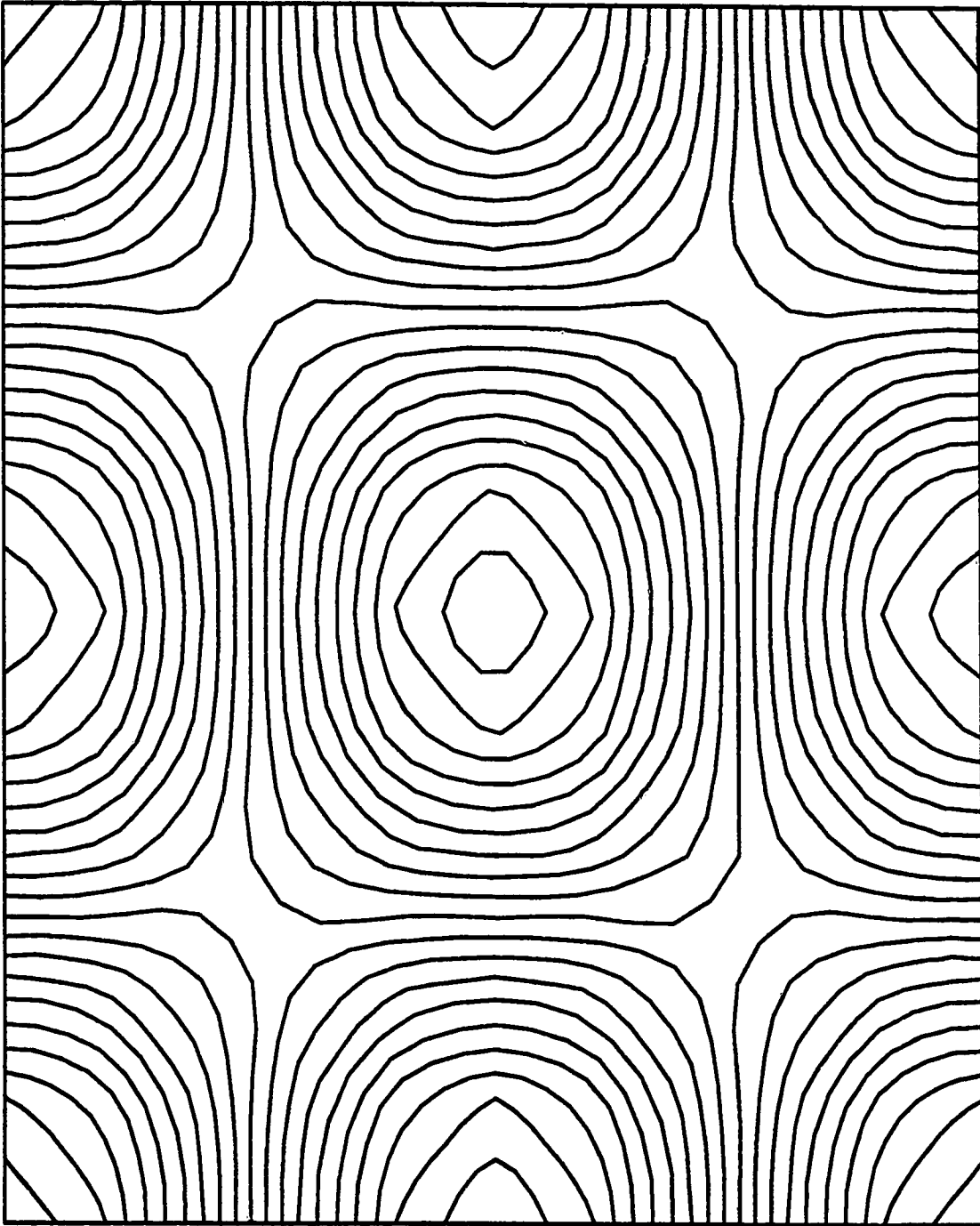Figure A.5 Contours of Z = COS(x)*COS(y) using 10 grid lines in the X and Y planes.

In order to evaluate the effect of random input error on the gridding and contouring procedure, the following tests are performed. Three of the horizontal contoured plots were chosen as base cases. These included the surface plot of mixing ratio values at 1400 UTC in the Alberta region, equivalent potential temperature and integrated moisture convergence at 1400 UTC on the LIMEX85 region. In order to introduce random errors into the base case input data sets, a random number file was produced containing a sequence of random numbers between -1.0 and 1.0. Using these random numbers, three separate magnitudes of error were introduced into the input data sets. The first corresponded to perturbing each base case input data point by a value equal to plus or minus the random number times the predicted mean error associated with the specific parameter (see Section 4.8 Error Analysis).

If $r_1...r_i...r_N$ represents the base case data field and $r_{p1}...r_{pi}...r_{pN}$ is the perturbed base case data field:

$$r_{pi} = ((\text{random number between -1.0 and 1.0}) \times (\text{Error Magnitude})) + r_i \qquad \text{(A.2)}$$

$$(\text{i running from 1 to N})$$

where: N is the number of irregularly spaced input data points

The second error magnitude used was the maximum error resulting from the error analysis (see Section 4.8 Error Analysis). The third and largest of the error magnitudes used was the standard deviation of the specific parameter resulting from the statistical analysis of the entire data base. The first error magnitude represents a distribution of error that is numerically consistent with the typical error associated with the particular variable. The first error magnitude on average spans 5.7% of the population range. The second error magnitude reflects the largest predicted error associated with the variable in question, spanning on average 16.3% of the population range. The third error magnitude represents a large distribution of error which is experimentally

unrealistic and spans 36.7% of the population range. The logistics of these sensitivity tests are summarized in Table A.1.

TABLE A.1   Random induced error magnitudes.

Parameter	Mean Error Magnitude 1	Maximum Error Magnitude 2	One Standard Deviation Error Magnitude 3
Mixing Ratio [g/kg]	0.25	1.53	2.57
Equivalent Potential Temperature [degrees K]	1.24	5.0	8.96
Moisture Convergence [g/kg h]	0.07	0.14	0.27

Figure A.5 depicts the effect of random errors on the 1400 UTC contours of mixing ratio on the Alberta study region. The mean error greatly increases the areal extent of the 9 and 6 g/kg contours. The overall shape of the pattern is retained. The maximum error has the effect of further deteriorating the overall pattern leaving only some resemblance to the original form. The effect of the standard deviation error yields a field which reflects the original pattern only to a small degree. This trend is repeated in Figures A.7 and A.8 where contours of equivalent potential temperature and moisture convergence are depicted, respectively. Mean and maximum errors yield contoured fields which resemble the original contours to a relatively high degree. However, the contours representing the effect of one standard deviation error bare little resemblance to the original figure. One can conclude that random errors reflecting small magnitudes, in the order of 15% of the data ranges or less, can cause the resulting contoured fields to change but still resemble the original pattern. The introduction of large random errors in the order of 35% of the data range can completely alter the form of the resulting figure as compared to the initial contour shapes.
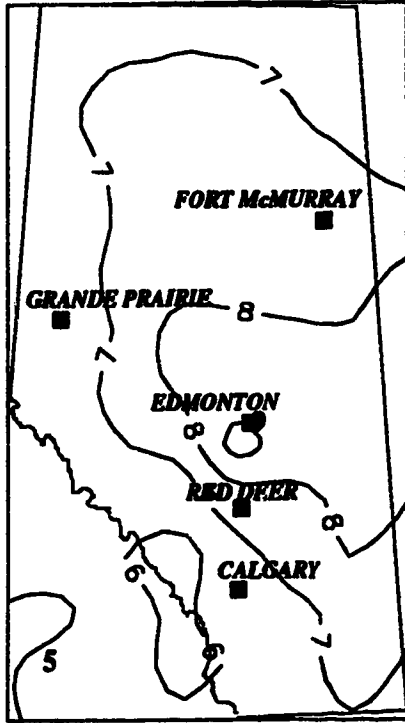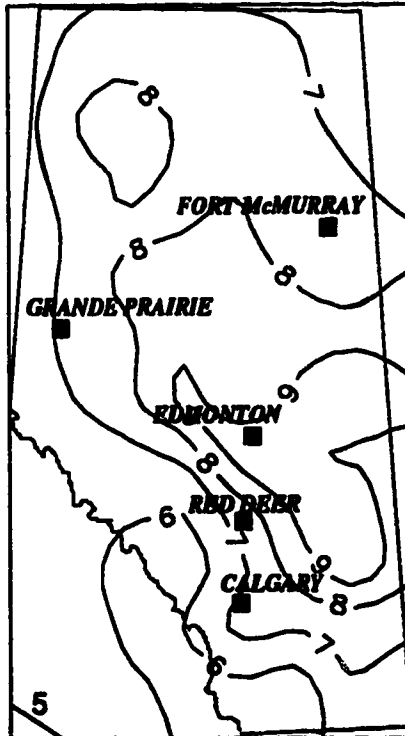
133

No random error

Mean random error (Magnitude 1)
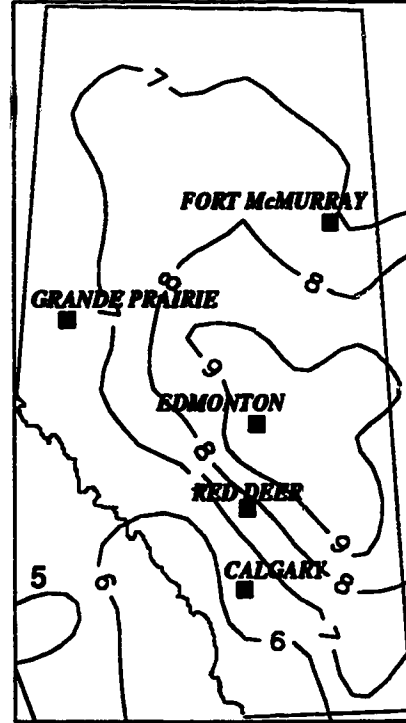
Maximum random error (Magnitude 2)

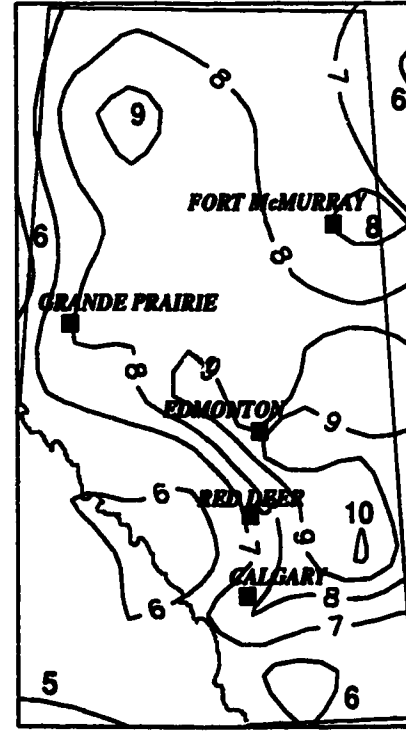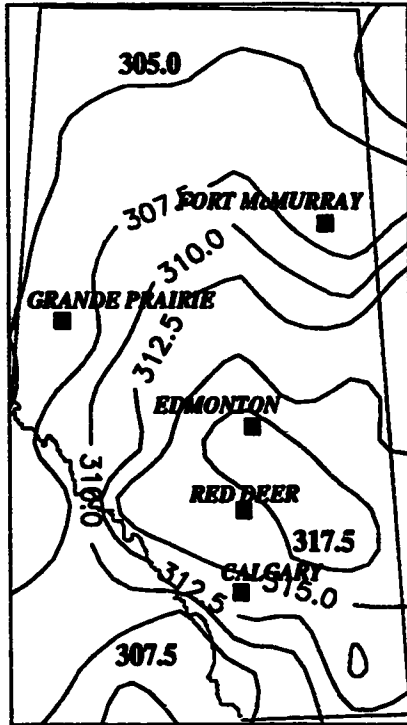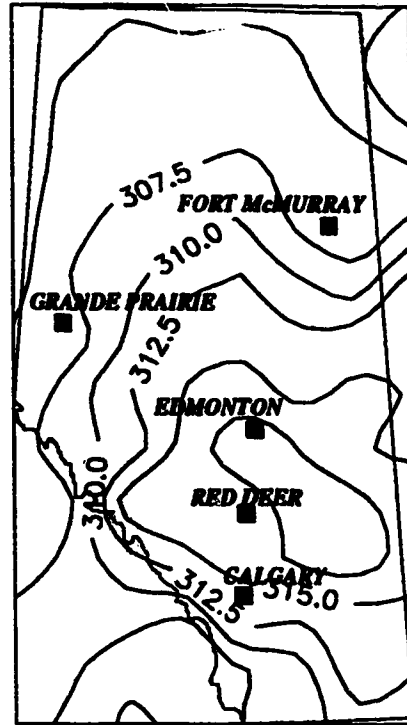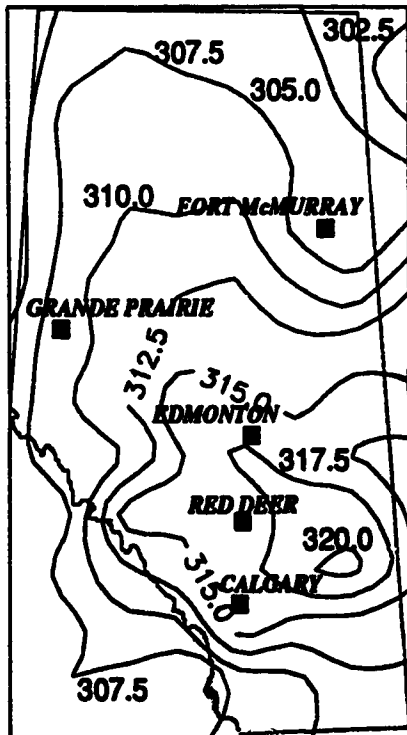One SD random error (Magnitude 3)

Figure A.6 Contours of mixing ratio r [g/kg] for various magnitudes of random error affecting the input data set. Initial data set from the surface in the Alberta Study Area at 1400 UTC July 11 1985.

No random error

Mean random error (Magnitude 1)

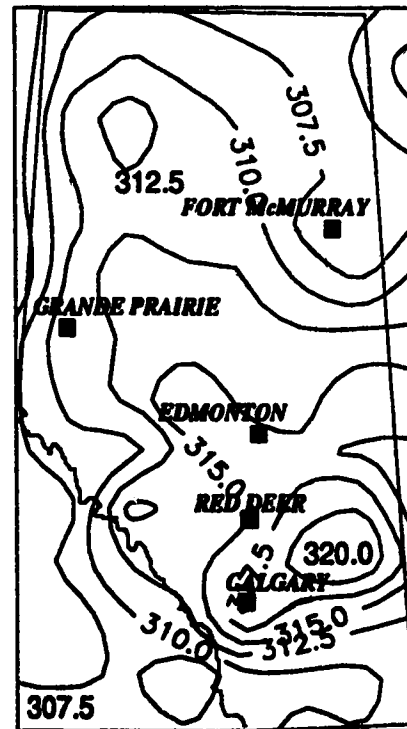Maximum random error (Magnitude 2)

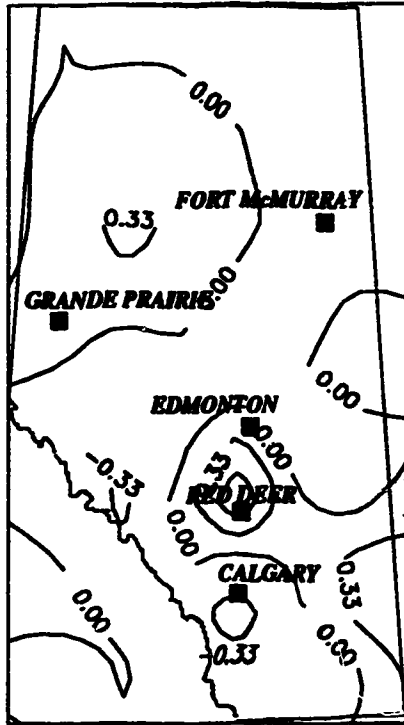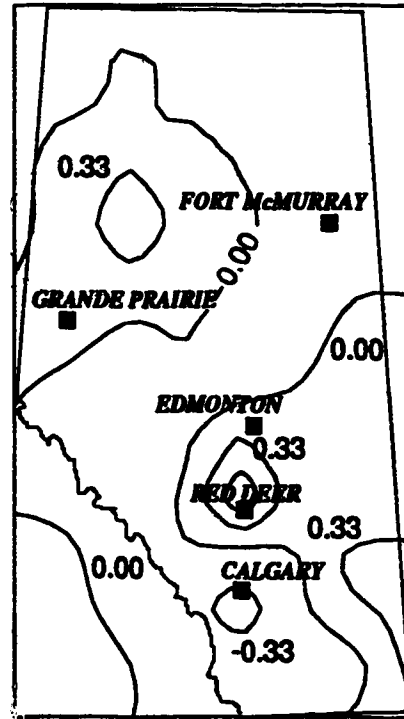One SD random error (Magnitude 3)

Figure A.7 Contours of equivalent potential temperature θe [degrees K] for various magnitudes of random error affecting the input data set. Initial data set from the surface in the Alberta Study Area at 1400 UTC July 11 1985.
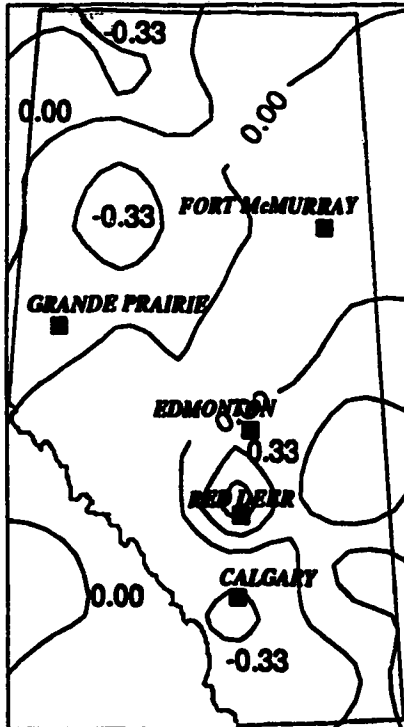
135

No random error

Mean random error (Magnitude 1)

Maximum random error (Magnitude 2)
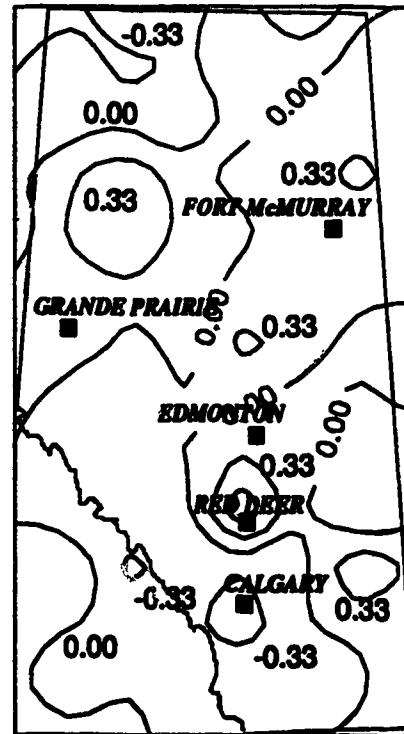
One SD random error (Magnitude 3)

Figure A.8 Contours of moisture convergence MC [g/kg h] for various magnitudes of random error affecting the input data set. Initial data set from the surface in the Alberta Study Area at 1400 UTC July 11 1985.